HIGH-THROUGHPUT SINGLE-CELL FUNCTIONAL AND MOLECULAR PROFILING OF IMMUNE CELLS IN CANCER IMMUNOTHERAPY

A Dissertation

Presented to

The Faculty of the Department of Chemical and Biomolecular Engineering

University of Houston

In Partial Fulfillment

of the Requirements for the Degree

Doctor of Philosophy

In Chemical Engineering

by

Ivan Liadi

August 2015

HIGH-THROUGHPUT SINGLE-CELL FUNCTIONAL AND MOLECULAR PROFILING OF IMMUNE CELLS IN CANCER IMMUNOTHERAPY

Ivan Liadi

Approved:

Chair of the Committee
Navin Varadarajan, Assistant Professor
Chemical and Biomolecular Engineering

Committee Members:

Richard C. Willson, Professor
Chemical and Biomolecular Engineering

Vincent M. Donnelly, Professor
Chemical and Biomolecular Engineering

Badrinath Roysam, Professor/Department Chair
Electrical and Computing Engineering

Shaun Xiaoliu Zhang, Professor
Biology and Biochemistry

Suresh K. Khator, Associate Dean
Cullen College of Engineering

Michael Harold, Professor/Department Chair
Chemical and Biomolecular Engineering

ACKNOWLEDGMENTS

- Dr. Navin Varadarajan for advising on doctoral studies and professional developments
- Dr. Vincent M. Donnelly, Dr. Richard C. Willson, Dr. Badrinath Roysam, and Dr. Shaun Zhang for serving as committee members for my doctoral defense
- Dr. Laurence J.N. Cooper, Dr. Harjeet Singh, and Dr. Helen Huls for collaborating on CAR^+ T cells and for providing cells, reagents, and running experiments
- Dr. Badrinath Roysam, Nicolas Rey-Villamizar, Amine Merouane, and Yanbin Lu for the collaboration and consultation on image processing and data analytics
- Dr. Richard C. Willson and the lab constituents for use and consultation of the lab equipments especially the ELISA plate readers
- Dr. Patrick Cirino for use of the flow cytometry
- Dr. Gabrielle Romain, Dr. Ankit Mahendra, Dr. Melisa Martinez, Dr. Victor G. Sendra, Dr. Vandana Kaul, Dr. Irfan Bandey, Anthony Lie, Balakrishnan Ramesh, JayR T Adolacion, Xingyue An and Shaza Abnouf for the invaluable help on experiments and supports
- Last but not least, to my dear family, friends, and relatives that have been tremendous source of spiritual and moral supports on my pursue of this degree

HIGH-THROUGHPUT SINGLE-CELL FUNCTIONAL AND MOLECULAR PROFILING OF IMMUNE CELLS IN CANCER IMMUNOTHERAPY

An Abstract

of a

Dissertation

Presented to

Faculty of the Department of Chemical and Biomolecular Engineering

University of Houston

In Partial Fulfillment

of the Requirement for the Degree

Doctor of Philosophy

in Chemical Engineering

by

Ivan Liadi

August 2015

ABSTRACT

Immunotherapy has revolutionized the treatment of cancer and newer approaches including the adoptive transfer of genetically modified T cells reprogrammed to target tumor antigens have shown remarkable responses. Despite their promise, the efficacy of adoptive immunotherapy remains unpredictable due to the heterogeneous nature of the infusion products, patients' characteristics, treatment regimens, and tumor burdens. Specifically with regards to the T-cell infusion product, there is a need to develop methodologies that allow for definition of potencies to understand the phenotypic, molecular, and functional contribution of infusion products at single-cell level.

In the first part of this dissertation, we implemented Timelapse Imaging Microscopy in Nanowell Grids (TIMING) to demonstrate that while $CD4^+CAR^+$ (CAR4) cells killed at slower rate, most likely due to lower granzyme B content, they benefited from apoptosis resistance compared to $CD8^+CAR^+$ (CAR8) cells. These findings suggest that overall potency of multi-killing should be evaluated together in their context to resist apoptosis.

In the second part of this dissertation, we developed single-cell multiplexed platforms comprising beads biosensors for detecting protein secretion, TIMING to monitor motility and cell-cell interactions, and microfluidic qPCR for transcriptional profiling. Analysis of thousands of single-cell interactions for over 5 hours revealed that the integrated behavior of polyfunctional T cells that kill and secrete IFN-γ was similar to those without IFN-γ secretion, suggesting cytolysis to be the dominant determinant of the interaction behavior and that killing enables faster synapse termination. In addition, tracking the speed of these cells by TIMING indicated that serial killer T cells may be

identified based on their high out-of-contact basal motility. Transcriptional profiling of these single-cells confirmed that the motile cells expressed increased amounts of perforin and displayed an activated phenotype.

In summary, these results highlight the heterogeneity of immune cells and thus, the need for definition of potency prior to infusion. We propose that single-cell platforms as demonstrated here are suitable to uncover the diversity and to help identify optimal functional and molecular biomarkers for applications in the clinic.

TABLE OF CONTENTS

LIST OF FIGURES

LIST OF TABLES

ABBREVIATIONS AND DEFINITIONS

aAPC: Artificial antigen presenting cells

ACT: Adoptive Cell Therapy

AFU: Arbitrary fluorescence units

AICD: Activation Induced Cell Death

AR: Aspect ratio of polarization represented as the ratio of the major and minor axes of the cell, fitted to an ellipse

CAR: Chimeric Antigen Receptor

CAR4 cell: $CD4^{+}CAR^{+}$ T-cell

CAR8 cell: $CD8^{+}CAR^{+}$ T-cell

CEF peptide: HLA-class I-restricted viral peptides typically used as positive control in eliciting IFNγ response for human PBMC

Conjugation: Stable contact between effector cell and target cell lasting > a single interval

CRA: 51Chromium Release Assay (population level assay) to measure cytotoxicity

d_{Well}: Net displacement of the T-cell centroid, within the nanowell, averaged over an interval

E: Effector cell

GzB: Granzyme B

Killing efficiency: Description of the kinetics of killing mediated by individual T cells (Please see tDeath below)

Killing frequency: Number of T cells capable of participating in killing

LoD: Limit of detection at different analyte concentration as assessed by beads assay or ELISpot

MFI: Mean Fluorescence Intensity

Multi-killer: CAR^+ T cells that kill at least two tumor cells at an E:T ratio of 1:2-5

Multi-killing: Ability of a single T-cell to kill two or more target cells

$\mathbf{N_{total}}$: Total number of events

PBMC: Peripheral blood mononuclear cells

Single killer: effector cells that kill tumor cell at an E:T ratio of 1:1

T: Target cell

$\mathbf{t_{AICD}}$: Time to effector cell death

$\mathbf{t_{Contact}}$: Cumulative duration of conjugation between t_{Seek} and t_{Death}

$\mathbf{t_{Death}}$: Time elapsed between first conjugation (t_{Seek}) and tumor cell apoptosis (Annexin V staining)

TIMING: Timelapse Imaging Microscopy In Nanowell Grids

$\mathbf{t_{Seek}}$: Time taken by effector cell to conjugate with tumor cell

1. Introduction

The heterogeneous nature of the immune cells and understanding of their respective potencies and interactional behaviors remain one of the most complex problems in biological systems. In the context of cancer immunotherapy, for example, infusion of bulk population of immune cells in adoptive cell therapy to fight cancer has often been met with varying results ranging from no response to complete remission. These results are understandable given the heterogeneity of the genetic makeup of the patients, of the infusion products, and the complexity of the tumor microenvironment just to name a few.

While bulk assays have been exceptional in providing insights into how populations of cells behave as a whole, the measurements obtained are average responses of the whole systems. This approach of averaging responses have implicit limitations i.e., the masking of specific cells with respect to its phenotypes (subsets, gene, protein expression, etc.), functionalities (cytolytic efficacy, cytokine secretion, motility, etc.), and interactional behaviors (cooperative, inhibitory, etc.). There is therefore a need to tackle this problem starting with an approach that we can control with relative ease i.e., understanding the makeup of this heterogeneous body of infusion products and furthermore, to identify and quantify the contribution and interactional behaviors of these products at single-cell level. Significantly, it is necessary to identify which single-cell with its functionality/ biomarkers or combinations (polyfunctionality) that is truly necessary and critical in mediating anti-tumor response, as not all immune cells in the infusion products contribute to tumor eliminations in cancer immunotherapy (1).

Cancer is a family of diseases involving abnormal cell growth stemming from genetic changes, which can be attributed to both external and internal factors. Some of the

treatment regiments available to cancer immunotherapy include chemotherapy, checkpoint blockades, vaccines, oncolytic virotherapy, kinase inhibitors, and adoptive cell therapy. The decision on the choices of treatments depends on several factors such as the types and severity of the leukemia, patients' age, white blood cell (WBC) count, cancer genetics, and previous exposure to cancer or treatment (2). Chemotherapy entails the use drugs to cure, control, or ease cancer symptoms. Several types of chemotherapy drugs are available commercially, each with their own mechanism of actions. Chlorambucil and cyclophosphamide are alkylating agent that are typically taken orally, and they work by attaching alkyl groups to DNA, thus damaging the DNA and cells in the process (3). Fludarabine is a purine analog that inhibits DNA synthesis and is taken intravenously (4). In the clinic, chemotherapy drugs have often been combined with FDA-approved monoclonal antibodies to combat cancers. In leukemia, the combinatorial use of fludarabine and cyclophosphamide with rituximab for example, has been shown to increase the survival rates of patients in the clinic (5). While the use of chemotherapy in combating cancer is promising, it is however not without any disadvantages. Chemotherapy drugs have been known to induce adverse side effects such as persistent fatigue, nausea, and hair loss (6). Although these drugs may work well against abnormal cancer cells, the effects of the drugs were also carried over to normal healthy cells. As expected, alkylating agents such as cyclophosphamide, also disrupt the DNA of normal healthy cells. Similarly, with rituximab mAb therapy, healthy B cells possessing CD19 on the surface were also killed in the process.

Vaccination has shown considerable promise in the regulation of immune response in fighting cancer and other diseases. As an example, Sipuleucel-T, a first dendritic cell

(DC) based vaccines approved by the FDA, has been shown to mediate anti-tumor response and prolong survival rate in several patients with prostate cancer(7). In other efficacy studies, vaccines have elicited antigen-specific polyfunctional responses of T cells in diseases model of HIV (8), vaccinia virus (9), and yellow fever (10, 11). While tools such as DNA microarrays allow for high-throughput profiling of vaccine-induced immune cells, they are limited with respect to averaging of the responses of immune cells at population level, thus downplaying the significance of the variation of polyfunctional immune cells. Importantly, analysis of rare subsets of these antigen-specific immune cells has also proven to be challenging.

FDA-approved checkpoint inhibitors such as anti-PD1 and anti-CTLA4 are two common inhibitors that have been studied extensively (12-14). CTLA-4 has been shown to be upregulated on T-cell surface, leading to the decline in T cells activation in response to tumor antigen. Similarly, PD-1 ligand has been found to be upregulated on the surface of certain tumors, contributing to inhibit T cells functions and to promote tumor escape mechanism. As in the case of vaccination and chemotherapy, the efficacy of these checkpoint inhibitors has shown varying efficacy from patients to patients, due to the heterogeneity of the tumor cells and the infusion products of each patient.

Another emerging treatment in cancer immunotherapy is oncolytic virotherapy, which uses carefully selected, replication-competent viruses to destroy cancerous tissues while causing no harms to normal tissue (15, 16). Oncolytic viruses kill cancerous cells in different ways ranging from direct cytotoxicity of the virus to a complex immune effector-mediated mechanism. One critical milestone of oncolytic virotherapy is demonstrated in a phase III melanoma clinical trial using talimogene laherparepvek (T-VEC) based on

engineered herpes simplex virus 1 (HSV-1). T-VEC possesses a dual-mechanism of action, destroying cancerous tissues through direct cytotoxicity and also by promoting cancer cell recognition and destruction by immune cells. The proposed mechanism of action can be broadly categorized into three parts i.e., (1) viruses enter normal tissues, unable to replicate, thus leaving cell unharmed, (2) viruses enter cancerous cells, replicate and secrete GM-CSF until the cell lyses with subsequent release of viruses and GM-CSF into circulation, and (3) GM-CSF attracts dendritic cells, which then present antigen to T cells. Despite this promising result, oncolytic virotherapy remains highly challenging due to several reasons i.e., difficulty to optimize systemic viral delivery, intratumoral spread, and cross-priming of immune system. As expected, suppression of immunity may increase intratumoral spread but at the same time diminishes cross-priming of immune cells and *vice versa.* In addition, clinical testing has suggested that this approach to move new product into phase I requires enormous work, expenses, toxicology testing, and regulatory approval.

Tyrosine-kinase inhibitors (TKI) represent another class of drugs that are commonly used in combating cancer by blocking the signal transduction cascades. Selective targeting of genetically altered tyrosine kinases have shown significant results in the clinical setting, suggesting that altered tyrosine kinases are main drivers of different cancers (17). One commercially available TKI that has been used to fight chronic myelogenous leukemia (CML) is the Bcr-Abl TKI. The Bcr-Abl tyrosine kinase (imatinib) results from abnormal fusion of break point cluster (Bcr) gene at chromosome 22 and Abelson (Abl) gene at chromosome 9, and it has been implicated in pathogenesis of more than 90% of CML cases. Other examples of TKIs drugs include gefitinib (18) and erlotinib (19) which act on epidermal growth factor receptor (EGFR). Overall, TKI drugs are

promising approach to fight cancer due to their relatively lower toxicity and higher specificity compared to non-specific chemotherapy drugs. Challenges associated with TKIs lie in the identification of suitable tyrosine kinases to inhibit, and the need for relevant *in vivo* models to assess function of both mutated and non-mutated tyrosine kinases.

Immunotherapy such as adoptive cell therapy (ACT) involves the use of the patients' own immune cells to mount a response against the tumor. ACT is a targeted therapy which has shown great promise in recent years (20, 21). In this therapy, immune cells such as T cells are isolated from patients, expanded *in vitro,* and then re-infused back into patients. While ACT with T cells and genetically engineered immune cells represent a major advance in steps toward tumor eradications, they were not without their challenges. As evidence, clinical results have shown that there are currently no therapy applicable or "magic bullets" that can be used to treat all types of patients with similar conditions. This observation is understandable given the lack of surface tumor antigen, heterogeneity of the tumor cells, infusion products and their respective potencies. The current technology of ACT is still generic with respect to the same receptors of immune cells being used for infusion but as more advanced genome engineering technologies such as TALEN and CRISPR-Cas9 become available and as neoantigens or biomarkers were discovered, approaches toward a more personalized gene-modified ACT can be achieved (22).

Nowadays, immunotherapy represents one promising approach for several cancer cases owing to its varying treatment options and promising results in the clinic. Checkpoint blockades and CAR^{+} based ACT, for example have shown durable responses in patients, even for those previously refractory to other chemotherapies. While this progress is remarkable, several questions and challenges still remain. For one thing, combinatorial

treatment has been expected to work on several settings. Combination of anti-PD1 and anti-CTLA-4 blockade with vaccine for example, has been shown to restore tumor rejection function of T cells in *in vivo* mice model. Despite this, there is still substantial debate over the optimal combination modules.

In the ACT front, it has been shown that ACT works in several patients on the clinical setting, however, these results only applies to a proportion of patients most likely due to factors such as heterogeneity of immune cells/infusion products, tumor burden, and genetic makeup of the patients. With respect to this heterogeneity of the inoculum, there is therefore a need to identify biomarkers/functionalities and define potency that can predict success, and this can be achieved by using the many single-cell profiling technologies that were available today. This step is necessary since analysis at the population level give only the average responses, and it has been shown that there is a subset of cells that contribute to the majority of anti-tumor response, thus making the selection and identification of these small subsets of cells critical not only for the sake of understanding mechanistic insights of these cells but also for design and manufacture of future infusion products. Some of the most well described functionalities of immune cells are direct cytotoxicity (23, 24), secretion of pro-inflammatory cytokines(25, 26), and motility (27). Success in quantifying this heterogeneity at single-cell at high throughput across multiple biological dimensions starting from intracellular and extracellular signaling to genomes and transcriptomes to cellular interactions could have huge implications on the discovery and improvement of immunotherapy (28).

In the past few decades, several single-cell technologies had been developed to study the functionality of immune cells. While *in vivo* systems that replicate the nature of

the tumor microenvironment were desirable, they were typically not cost-effective and require complex tools to perform. In addition, analyses of these data were often difficult and exacerbated by background noise. On the other hand, *in vitro* microsystems and microfluidic systems were suitable for high throughput interrogation of single cells as they were more cost effective, simpler to run, and relatively easy to customize, though they were typically lacking when it comes to spatial and temporal resolution for studying complicated systems. With that being said, microsystems have developed to become more powerful as they had been adapted to handle multiplexing for interrogation of multiple functionalities in high throughput manner, all on conditions that mimic closely those *in vivo*. In this review, we examined recent single-cell microfluidic systems and looked at how a dynamic and modular system can help us expand and decouple the complex depths and breadths of heterogeneous systems.

1.1. Single-cell system for protein secretion and proteomic studies

Microfluidics system are versatile enough to be extended to study the multiplexing capacity of immune cells and can be incorporated with other functional assays while minimizing undesired perturbation and damage to cells. In the context of proteomic studies for single-cells, two of the most common microfluidic approaches used are microengraving and antibody barcode arrays.

1.1.1. Microengraving

Initially described by the Love group, microengraving was in the beginning used predominantly for rapid screening of antigen specific antibodies from individual hybridoma cells (29). This technology is based on the soft lithography technique and polydimethylsiloxane (PDMS) arrays in which submicron wells at pico-liter volume were used to isolate and protein secretion from single cells.

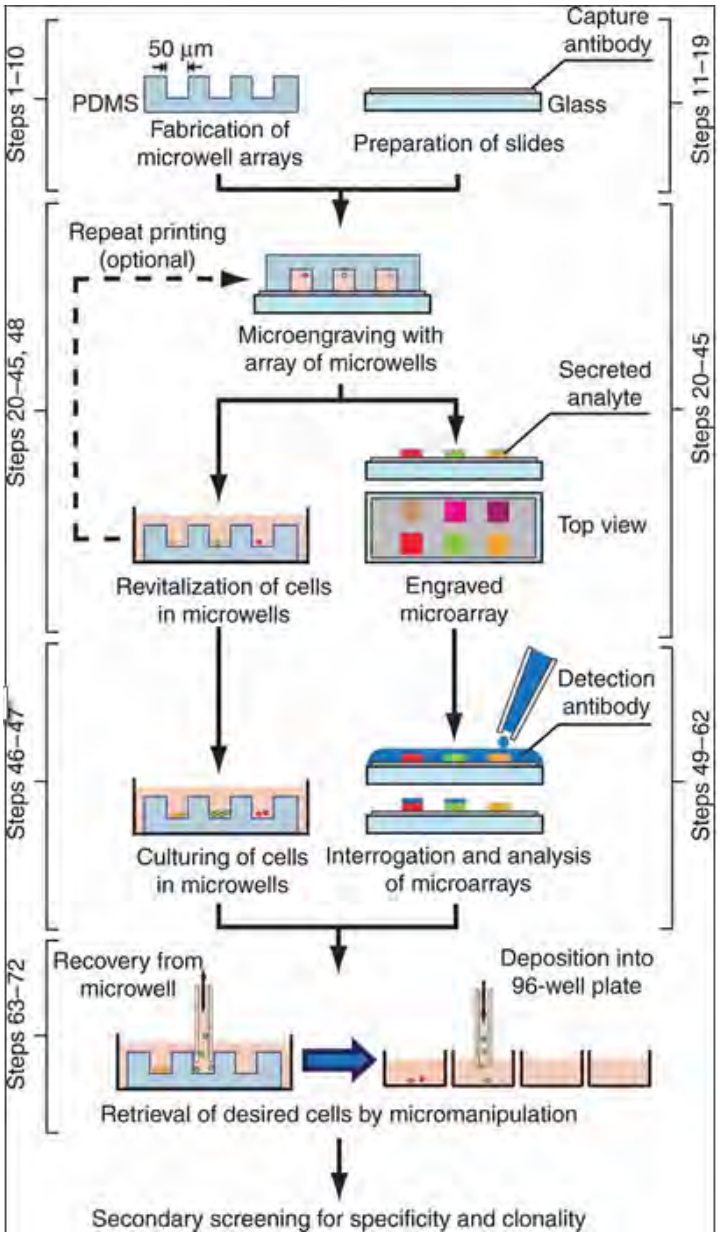

Figure 1: Schematic of microengraving for detection of end-point cytokine secretion from single cells

Today, microengraving techniques have been expanded and coupled with other functional techniques such as cytolytic frequency measurement through end-point imaging on nanowell arrays, making it a powerful system for studying multi-functional attributes of single cells.

In microengraving, nanowell arrays containing ~100,000 wells containing single cells were hybridized/printed with functionalized glass substrate coated with capture antibodies against cytokines of interest (30, 31) (**Figure 1,** reproduced and captioned from {Ogunniyi, 2009 #289}, copyright owned by Nature Publishing Groups**)**.

During hybridization, cytokines secreted from single-cells were captured on the functionalized glass substrate and detected with secondary label antibodies. The strength of these techniques lies in the fact that specific cells with desired phenotypes can be retrieved for further profiling using micromanipulator. In addition, Han *et al.* has also shown that sequential microengraving can be performed for prolonged amount of time (>12 hr) at an interval of 2 hr for each hybridization to look at kinetics of cytokine secretion (32). This process however is time consuming and labor intensive as it requires many washing steps and careful printing/separation steps in which cells may potentially be lost. In addition, microengraving is usually performed after cytolytic assay and requires long-term hybridization, thus the complete kinetics of cytokine secretion may not be captured entirely as the kinetic windows for each hybridization are typically long (>1hr). In addition, due to the encapsulated nature of the process, a lack of nutrient and gas exchange for prolong amount of time may potentially affect the biology of the cells. In addition, accumulation of protein over time in constraint wells might potentially affect the behavior of cells thus it may not be compatible for long-term studies.

1.1.2. Antibody barcode arrays

Developed by the Heath group, single-cell barcode arrays (SCBC) comprises hundreds to tens of thousands of microchambers (<1 nL volume) in which protein concentration is measured by utilizing spatially resolved miniature antibody arrays with

immunosandwich assays (33-35). Using multi-color scheme and specific design of SCBC to enable cell lysis, this approach can be used to assay around 20 secreted, membrane, or cytoplasmic proteins and it can be integrated with multi-color flow cytometry to combine functional proteomics with phenotypic analyses.

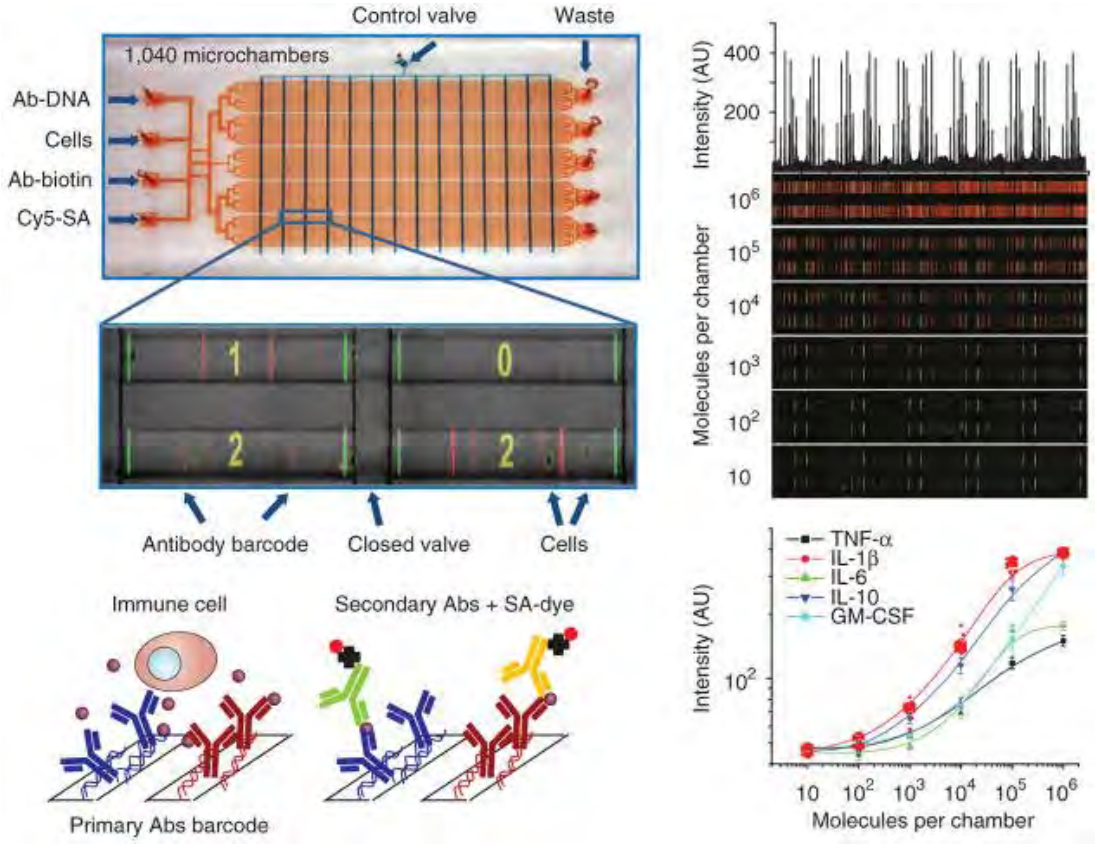

Figure 2: SCBC for single-cell protein secretome analysis

In one of the study with modified SCBC, Wang *et al.* associated PI3K signaling activity with cell-cell separation in a tumorigenesis study of glioblastoma multiforme cancer cells (36). Looking at interactions of pairs of brain cancer cells, they found that at short time interval (30 min), the cells do not exhibit any influencing behavior on one another. At long time interval (6 hr), however, they found that cells inhibits one another based on protein expressions at short distance (<90 μm). On the contrary, at long distance (>90 μm), the pair of cells mostly exhibit activating responses on one another.

On a separate study with SCBC, Ma *et al.* studied the functional diversity of melanoma-associated antigen MART-1 specific $CD8^+$ T cells from 3 representative clinical trial patients (**Figure 2,** reproduced and captioned from (33), copyright owned by Nature Publishing Groups). Specifically, they performed a kinetic study that last for a 90 day trials by combining a 19-plex SCBC functional proteomic assays with 10-color flow cytometry to look at the evolution of T cells phenotypes. The conclusions from this study were two fold (1) by combining the single-cell data from each patient, T cells could be loosely classified based on their biological behavior such as anti-tumor or pro-inflammatory (2) there exists a subset of highly polyfunctional T cells in which roughly 10% of these T cells secrete five or more different proteins and they do this at an approximate 100 –fold higher copy numbers compared to the less polyfunctional T cells. Importantly, this polyfunctionality kinetics correlates with clinical observations.

On a separate and recently published study, Lu *et al.* from the Fan group demonstrated a highly multiplexed platform to detect secretion of 42 immune proteins, the highest multiplexing recorded to date at single-cell level (37). This technology works by super-imposing an antibody barcode array with a PDMS-based microchamber array containing single cells, thus creating an encapsulation. The barcodes capture secreted cytokines during hybridization and are subsequently removed and completed with detection antibodies. In this study, Yao used this platform to profile lipopolysaccharide (LPS) stimulated macrophages. Their key findings were as follows (1) this technology revealed the existence of macrophage dynamic macrostructure within the population which is conserved in response to different toll like receptors (TLR) stimulation (2) this technology revealed profound functional subpopulations with differential response and

activation level in this phenotypically homogeneous population (3) this technology promoted identification of macrophage inhibitory factors (MIF) that potentiate activation of LPS-regulated cytokines.

Overall, antibody barcode arrays are robust platform for highly multiplexed quantification of proteomes for single-cell studies. They are scalable, high-throughput, and require small sample size suggesting potential integration capability with other upstream approach such as flow cytometry. Despite these advantages, antibody barcode arrays may also suffer from encapsulation process as in the case of microengraving. Both of these techniques are also heavy on the data front. In microengraving for example, quantitative modeling and analysis are required to obtain frequency and secretion or distribution of secreting single cells on the nanowell arrays. Similarly, in antibody barcode arrays, unsupervised data-driven modeling and clustering was critical to understand and uncover the unique information disclosed through single-cell measurements.

1.1.3. Mass cytometry (CyTOF)

Flow cytometry is a powerful single cell technology that allows for rapid screening of up to 15 fluorescent parameters. One of the limitations of the flow cytometry is the reliance on fluorescent tags conjugated to antibodies, which may result in auto-fluorescence and spectral overlap. These issues were exacerbated as more fluorochromes were used (38). To circumvent these issues, a new technology has to be considered. Mass cytometry is a powerful technique that relies on highly purified stable rare metal isotopes as the labels to the antibodies and it has several advantages over flow cytometry such as: (1) no auto-fluorescence as the isotopes were not present in biological samples, (2) no

compensation as there is no spectral overlap, (3) higher multiplexing capability (>40+ parameters possible), (4) improved conjugate signal intensity.

In a study by Bendall *et al.* from the Nolan group, they used mass cytometry to simultaneously measure 34 parameters of single-cell (31 antibody bindings, DNA content, viability, and cell size) in a healthy human bone marrow model (39). Eighteen markers of functional signaling states perturbed by stimuli or inhibitors was used to monitor signaling behavior of cell subsets of a defined hematopoietic hierarchy, and the resulting data set was categorized and clustered as defined by surface expression, resulting in superimposable map of single-cell signaling response with drug inhibition. Significantly, the analyses revealed precise signaling motifs within defined cell subsets and continuous phosphorylation behaviors crossing population boundaries that can be tracked closely with cellular phenotypes. Overall, mass cytometry allows for highly multiplexed coupling of phenotypic characterization/biomarkers of single-cell with functional responses. Despite these advantages however, mass cytometry suffers from lower throughput (10x lower than flow cytometry), no cell sorting capability, low frequency of cells analyzed (only ~30 %), and small selection of compatible antibodies for tagging.

In a separate study by Bodenmiller *et al.* also from the Nolan group, they introduced mass-tag cellular barcoding (MCB), which increases traditional mass cytometry throughput by using *n* metal ion tags, thus bringing up the multiplexing capacity up to 2^n samples (40). In this particular study, Bodenmiller used seven tags to multiplex an entire 96-well plate and applied MCB to characterize human peripheral blood mononuclear cell (PBMC) from eight donors, and the corresponding effects of 27 inhibitors on the PBMC

(**Figure 3**, reproduced and captioned from (40), copyright owned by Nature Publishing Groups).

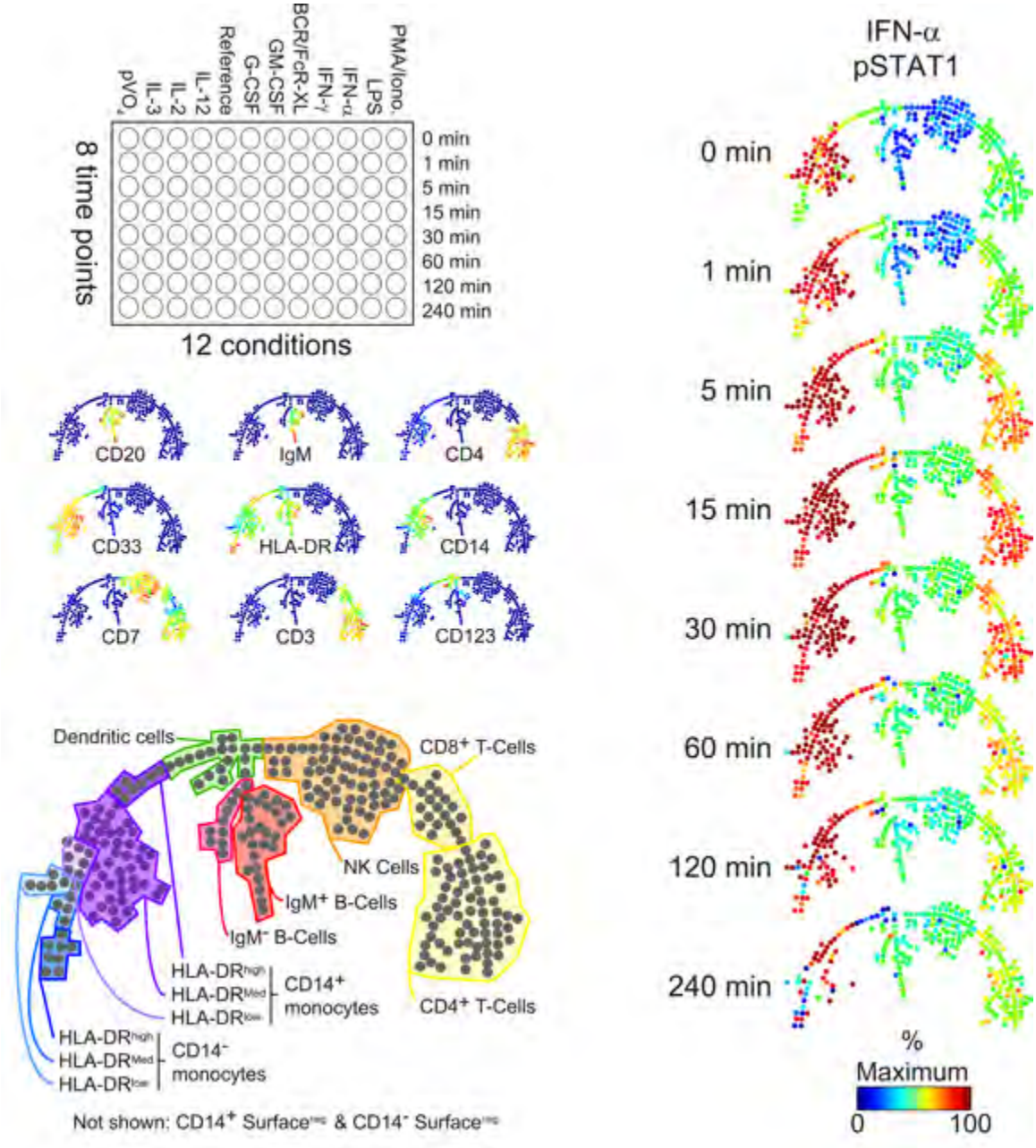

Figure 3: PBMC signaling time-course experiment with mass cytometry

In summary, they measured 14 phosphorylation sites in 14 PBMC types at 96 conditions resulting in an astonishing 18,816 phosphorylation levels from each sample.

Overall, screening with MCB could be useful for high throughput screening in the context of diseases mechanistic studies, drug discovery and design, and pre-clinical testing.

1.1.4. Droplet microfluidics

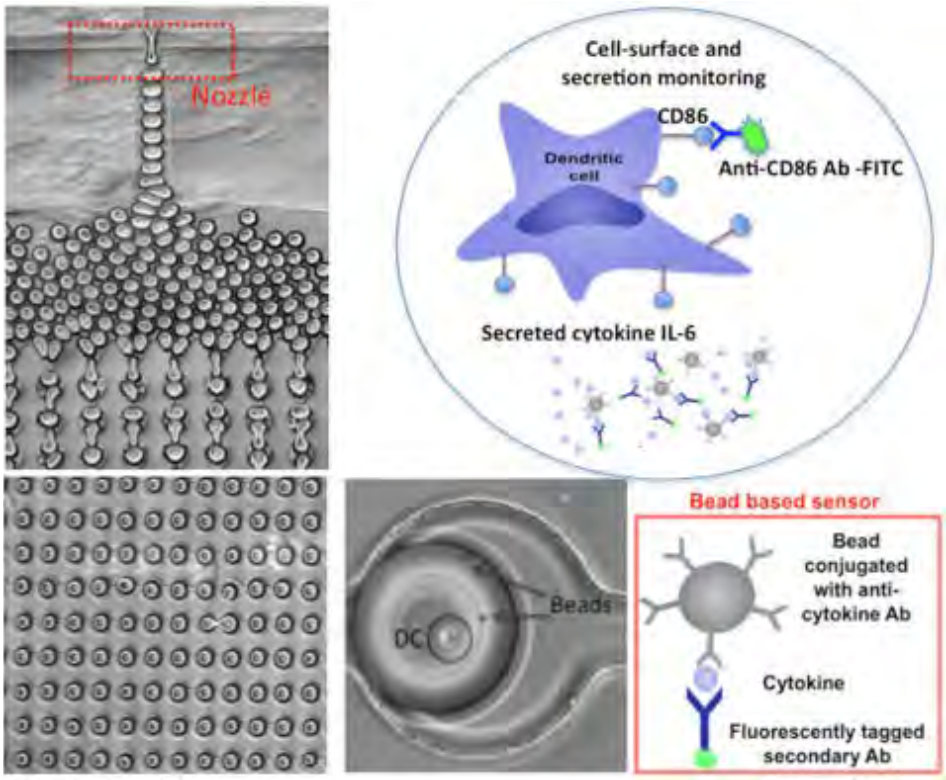

Figure 4: Droplet generation in the PDMS device and illustration of microfluidic reaction droplet for monitoring cell surface and secretion simultaneously

Another technology to study single-cell is the droplet microfluidics. Konry *et al.* designed nano-liter microfluidics based reactors coupled with microsphere-based sensors to stimulate and monitor surface and secreted markers of single cells and single-cell interactions **(Figure 4,** reproduced and captioned from (41), copyright owned by Nature Publishing Groups).

The technology relies on microfluidics with 3 main inlets which can be modified depending on the desirable studies. In one of the studies, Konry *et al.* designed a 3 inlet microfluidics containing oil inlet, dendritic cells (DC) inlet and bioassay reagents inlet

(beads and antibodies). The oil inlet facilitated the formation of micro-reactor droplets encapsulating single DC with anti-CD86-FITC antibody to profile surface marker of the DC and beads (anti-IL-6-FITC coated) to capture secreted IL-6 from the DC simultaneously. Similarly, on another study, they encapsulated regulatory T cells (T_{regs}) and utilized beads to detect and screen for single cell that secrete IL-10. In another study, they modified the inlets of the microfluidics to include single naïve T-cell in order to monitor immunological synapse (IS) formation and more specifically, the cytoskeleton remodeling and microtubule polymerization in DCs.

The versatility of microfluidics has allowed its technology to be readily combined with other technology such as flow cytometry. Chokkalingam *et al.* used droplet microfluidics and functionalized beads to probe for multi-cytokine secretion (IFNγ, TNFα, and IL-2) from PMA/ionomycin stimulated single Jurkat T-cell suspended in the droplet (42). The population of single-cell was then run through flow sorting in order to screen and bin the single-cell based on the types of cytokines they secreted or did not secrete.

Overall, the droplet microfluidics technology is a powerful single-cell encapsulation technique to physically and chemically isolate cells while minimizing risk of cross-contamination and promoting fast, efficient mixing of reagents. Despite these advantages however, droplet microfluidics are not without their disadvantages as the accumulation of secreted factors from cells were isolated and not allowed to diffuse outside leading to aggregation of factors such as secreted proteins that could potentially alter the behavior of the encapsulated immune cells. In *in vivo* system where immune cells and environmental conditions were open systems, droplet microfluidics might not be compatible especially for long term studies.

1.1.5. Aptamer sensors

Antibody detection technology typically involved multiple washes and reagents and on some cases, may not be compatible with real-time detection of proteins secretion. One of the strategies to counter this is by using aptamer beacons, which are single stranded DNA or RNA probes that bind proteins of interest and subsequently emit signals upon interaction with target proteins (**Figure 5,** reproduced and captioned from (43), copyright owned by Springer).

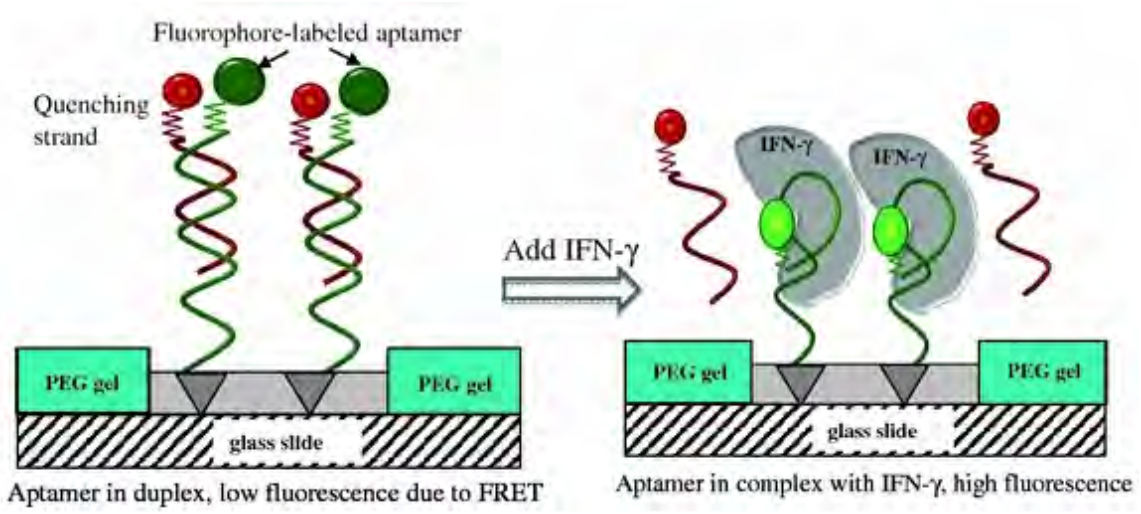

Figure 5: Schematic description of cytokine-sensing microwells.

Briefly, Tuleuova *et al.* demonstrated the use of aptamer beacons for detection of IFNγ in real time in microwell arrays (43, 44). Initially, the aptamer becons were quenched with quencher-carrying complementary strands resulting in formation of DNA duplex with low fluorescence. As the duplex was exposed to IFNγ, the quencher was displaced and the aptamer-IFNγ complex resulted in high fluorescence signals.

1.1.6. Localized surface plasmon resonance (LSPR)

Another microfluidics based technology to study proteins secretion from single cells in real time is the label-free localized surface plasmon resonance (LSPR) imaging

proposed by Raphael *et al.* (45, 46). LSPR technology works by taking advantage of the increase of intensity when proteins bind at the surface of a patterned metallic nanostructure thus creating perturbations in the local index of refraction. Upon exposure of these surfaces to charge-coupled device (CCD) camera, the signals are then amplified and manifested as bright nanostructures. The advantages of the LSPR technology are four-fold i.e., (1) real-time measurement limited only by camera exposure time (2) ease of integration with traditional bright field and fluorescence imaging (3) built-in spatial and temporal quantitative determination of protein secretion (4) negative controls can be quantified based on arrays sufficiently far away from the cells. In their paper, Raphael *et al.* utilized the LSPR to temporally and spatially map secretion of anti-c-myc antibodies from single 9E10 hybridoma cell, and found two modes of secretion. The first type of secretion was a continuous secretion and the second one was a concentrated burst which coincided with morphological contractions of the cells. Overall, this technique is highly robust and can be adapted as a quantitative tool for study of paracrine protein signaling.

1.2. Single-cell system for gene expression study

1.2.1. Gene expression cytometry (CytoSeq)

Aside from the quantification of proteins secretion or expression, the process of understanding heterogeneity of single-cells also benefits from quantification of gene expression. While flow cytometry can provide single cell measurement of protein expression, there are limited tools available for studying RNA/DNA expressions from single-cell. Fan *et al.* from the Fodor group recently developed a gene expression cytometry that combine next generation sequencing with stochastic barcoding of single-cell (47). This technology, called CytoSeq, utilized microfluidics platform with combinatorial beads

library to uniquely label transcripts and reconstruct digital gene expression profiles of thousands of single cells (**Figure 6,** reproduced and captioned from (47), copyright owned by AAAS).

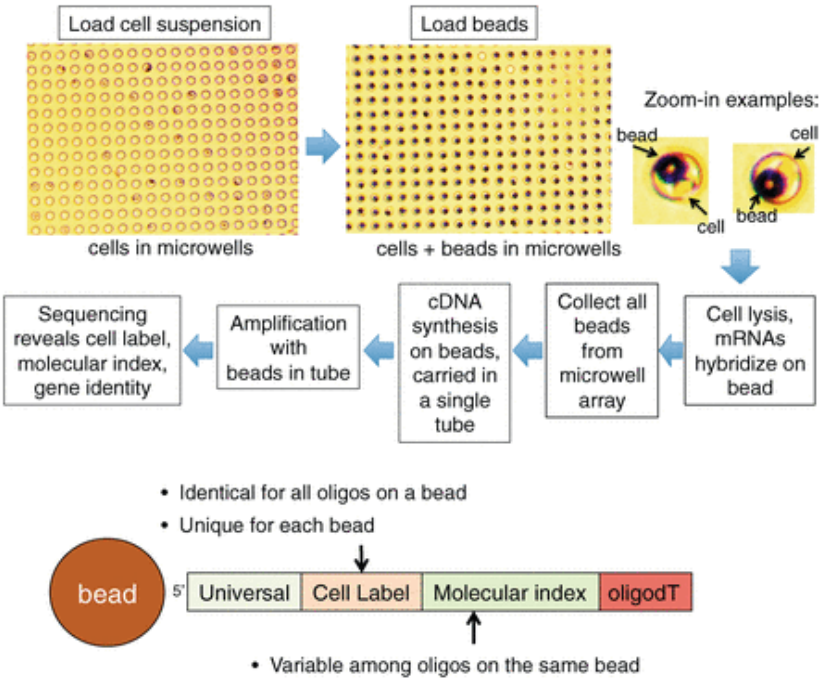

Figure 6: Experimental procedure for CytoSeq and structure of oligonucleotides attached to beads.

Briefly, the experimental procedures involved isolating single cells on microwells with beads, which upon cells lysis allow for hybridization of mRNA on beads. Next, beads were collected from the arrays and cDNA synthesis and further amplification were performed on beads in a single tube. The sequencing results further revealed the cells label, molecular index, and gene identity. Applying this technology, Fan *et al.* dissected the human hematopoietic system and further characterized responses to *in vitro* stimulation. For example, they first simultaneously identified major cell types in human PBMC samples based on looking at 632 single PBMC and 98 genes and dissected these PBMCs into monocytes, NK cells, T cells subsets and B cells by principal component analysis (PCA).

They further delved into the quantification of gene expression variation in unstimulated $CD3^+$ T cells vs stimulated $CD3^+$ T cells (with antibody against CD3 and CD28) and found upregulation of several genes in stimulated samples. Overall, these approaches allow for robust and rapid quantification of gene expression, without the need for expensive robotics for single-cell manipulation.

1.2.2. Fluidigm single-cell profiling

Single cell gene expression platforms had also shown great promise in helping understand the roles of individual immune cell in the context of protective immunity after vaccination. Flatz *et al.* in their study profiled different subsets of $CD8^+$ T cells and revealed their varying and differentially expressed gene profiles upon inductions with three HIV vaccines (48). While their population study with these vaccines revealed similar antigen-specific stimulation with respect to magnitude, phenotype and functionality of $CD8^+$ T cells, remarkably, single cell gene expression analysis enabled the discrimination of central memory (CM) and effector memory (EM) T cells. Specifically, expressions of *Eomes, Cxcr3, and Ccr7 or Klrk1, Klrg, and Ccr5* enabled differentiation of CM and EM subsets respectively. Taken together, single cell gene expression platform can facilitate the design and evaluation of vaccines, help decouple the mechanism of protective immunity, and potentially contribute to understanding and quantifying efficacy of therapies in cancer immunotherapy.

1.2.3. Single-cell RNA-seq

Cell-cell communication represents a significant event in which cells regulate their cellular heterogeneity upon encounter with different antigens and signaling cues. Shalek *et al.* performed single cell RNA-Seq of 1,700 primary mouse bone marrow-derived dendritic

cells (DCs) on microfluidic platform and found significant differences between identically stimulated DCs with respect to both the level of transcription of the cells and the fractions of DCs expressing the given mRNA (49). They uncovered a small number of "precocious" cells that express Ifnb1 and "core" anti-viral genes very early after lipopolysaccharide (LPS) stimulation, in which through the secretion of IFN-β, help promote anti-viral genes in other cells, leading to population level response (paracrine signaling). These "precocious" cells were only distinguishable through the expression of "core" anti-viral genes, but were critical for timely and efficient responses at the population level. Overall, this study highlighted the power of single cell in studying heterogeneous sample sizes which include rare novel subsets of immune cells and their contribution to overall population-level responses.

1.3. Single-cell system for cytotoxicity and migration assays

1.3.1. End-point imaging on nanowell arrays

Aside from microengraving application, nanowell arrays have also been used to study single-cell mediated cytotoxicity. Varadarajan *et al.* used nanowell arrays to study and evaluate the ability of thousands of single $CD8^+$ T cells to lyse HIV-infected cells and secrete IFNγ (50). The authors found that these two functionalities were discordant for the majority of single T cells as the T cells encounter cognate antigens. The evaluation of single-cell cytolytic efficacy in this case was performed by taking live-imaging of the nanowell arrays at t = 0 hr and 4 hr, and accounting for cell deaths through labeling by SYTOX green nucleic acid stains. Despite its powerful ability to quantify single-cell effector-mediated lysis, this methodology has its limitation, as it does not provide

information on the kinetics of killing i.e., time to kill, motility of effector cells, conjugate formation, eccentricity to name a few.

1.3.2. On-chip time-lapse imaging

On another single-cell study, Khorsidi from the Onfelt group studied the migration behavior of natural killer (NK) cells by utilizing time-lapse microscopy (51). Specifically, they calculated the mean-squared displacement of NK cells and determined the curvature and trajectory of individual NK cells. They further categorized the migration behaviors into three parts i.e., (1) transient migration arrest periods (TMAPs), (2) directed migration, (3) random movement, and found that TMAPs correlate with conjugation and target lysis. On a similar study, Forslund *et al.* from the Onfelt group designed and utilized microchip with deep wells (50 µm x 50µm x 300 µm) to perform live cell imaging and demonstrate the cytotoxic potential of NK cells and interactions with target cells (**Figure 7,** reproduced and captioned from (52), copyright owned by Frontiers).

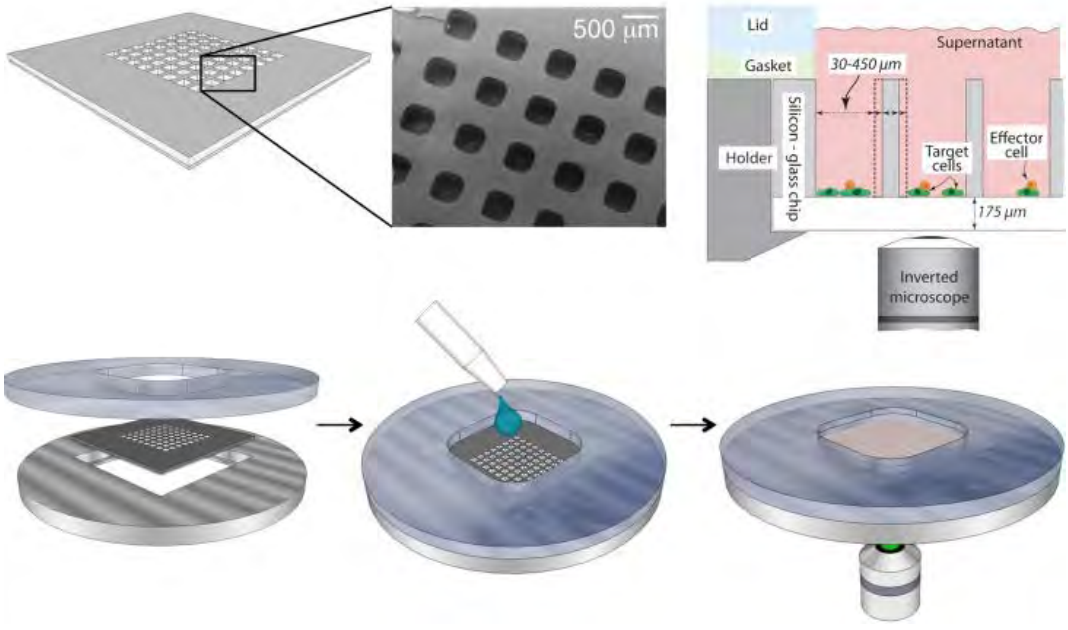

Figure 7: Schematic overview of the microchip platform from Forslund's experiment

The advantages of this deep wells are that they ensured entrapment of cells in the wells while providing sufficient nutrients for prolonged experiments (>4 days). On another study by Vanherberghen *et al.*, also from the Onfelt group, they further categorized NK cells into five subgroups based on dynamic cytotoxicity using time-lapse microscopy on a micro-chip system (53). The majority of NK cells were found to not be involved in any cytotoxic events, whereas some of the minority was found to be involved in the death of the majority of the target cells. Importantly, a small subset of NKC called "serial killers" was shown to deliver their lytic hits of multiple targets faster and in a consecutive manner. These results further highlight the heterogeneity of immune cells and showcases that averaging functional responses over the whole spectrum may not capture the whole picture. Ideally, understanding the contribution of individual cells may potentially help design future regimen for immune cells infusion in adoptive immunotherapy.

Sackmann *et al.* on another studies proposed a handheld diagnostic microfluidic-based platform to look at neutrophil chemotaxis for distinguishing asthmatic from non-asthmatic patients (54). Briefly, whole blood from patients was suspended on the "base" of microfluidic chips, and neutrophils were captured by P-selectin substrate and other components were removed with laminar flow wash steps. The "base" was hybridized with the "lid" containing hydrogel chemoattractant mixture (H-CA) which initiated the neutrophil chemotaxis. Images were then taken, and the chemotaxis data were tracked and analyzed with software to generate outputs that describe the neutrophil absolute speed, chemotactic index, and chemotactic velocity. Sackmann *et al.* analyzed 34 patients with this platform and found that the neutrophil chemotaxis velocity was determined to be significantly slower for asthmatic vs. non-asthmatic patients with sensitivity and specificity

of 96 % and 73 % respectively. Overall, this assay demonstrated how microfluidics can potentially serve as suitable platform to look at migration of immune cells, and in this case, a significant time-saving assay compared to traditional diagnostics assay.

1.3.3. Dielectrophoresis-based array (DEPArray)

Abonnenc *et al.* described a software-based lab-on-a chip platform of dielectrophoresis-based array (DEPArray) combined with time-lapse epifluorescence microscopy to manipulate cells interactions by entrapment through DEP cages and monitor lysis –on-chip of single target cells by cytotoxic T lymphocyte (CTL) and NK cells (55). Briefly, DEP system utilized interdigitated electrode arrays to generate DEP forces that decay exponentially from the surface, thus allowing for force manipulation of cells in a non-uniform electric field.

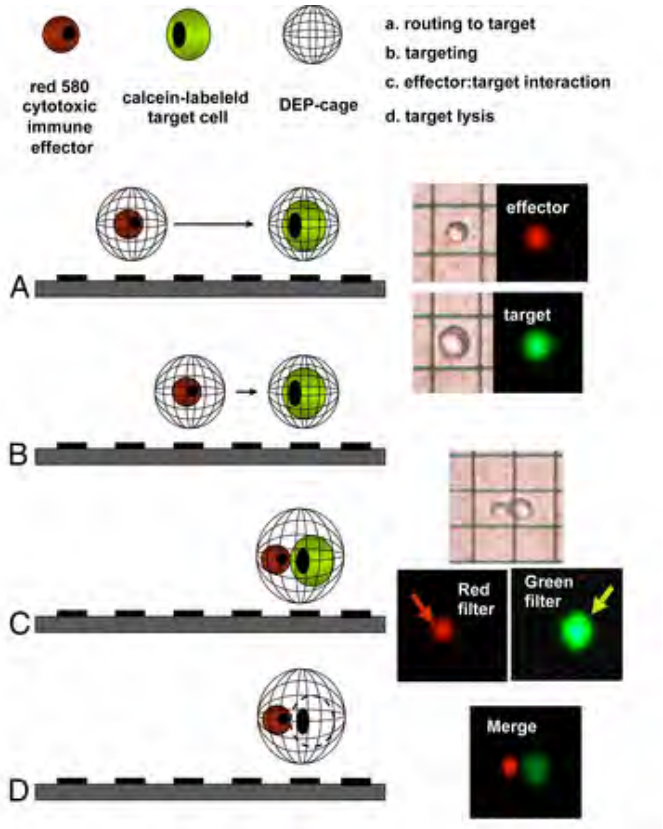

Figure 8: Step-wise targeting of a single target by effector on DEPArray.

In this study, they assess cytotoxicity by real-time quantitation of release of calcein dye from target cells and also further showed that this technique can be used to discriminate non-lytic effectors and refractory target to immune lysis in a heterogeneous population (**Figure 8,** reproduced and captioned from (55), with permission from the Royal Society of Chemistry). While DEP arrays are extremely useful for spatial micromanipulation of cells with high trapping efficiencies, it may be challenging when it comes to simultaneously maintenance of cell patterning and microenvironment.

1.4. Single-cell system for proliferation, activation, and differentiation assays

Long term monitoring of immune cells represents a critical and challenging part of understanding the dynamic heterogeneous population, where immune cells have often been lost in the process, either through the perturbation of the microenvironment or the tendency of cells to move in or out of confinement given enough stimuli. In a study by Zaretsky *et al.*, they designed deep microwells based on combination of PDMS arrays and standard culture plate to monitor single-cell proliferation, activation, and differentiation up to 72 hrs (**Figure 9,** reproduced and captioned from (56), copyright owned by).

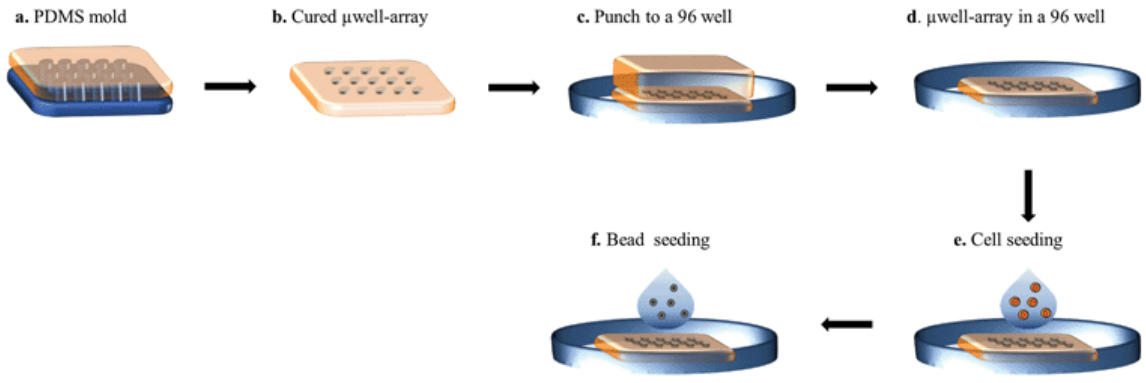

Figure 9: Microwell array fabrication and cell loading in Zaretsky's setup

Specifically, $CD4^+$ T cells were loaded onto microwells along with activation microbeads (anti-CD3/anti-CD28) and quantitative data on proliferation and deaths were

calculated. CD69 expression, which is upregulated upon activation of the $CD4^+$ T cells by microbeads, is detected by PE-conjugated anti-CD69. Furthermore, they showed that this platform can be used to study differentiations of immune cells. In this case, naïve $CD4^+$ T cells with Foxp3-GFP fusion that are isolated from mice expressed Foxp3 upon addition of proper stimulation molecules i.e., transforming growth factor beta (TGFβ) and interleukin 2 (IL-2).

On a separate study, Dura *et al.* designed a microfluidic platform with trap-like geometry in order to force single-cell pairing, thus allowing studies of cell-cell interactions (57). Combining the microfluidics with microscopy and on-chip fixing, they specifically studied lymphocyte activation and showed dynamic and static measurements to inform on cell intrinsic and extrinsic factors on cellular responses. Activation of OT-1 specific $CD8^+$ T cells were shown through calcium (Ca^{2+}) flux and three different modes of stimulations i.e., antigen specific stimulation by peptide loaded B cells, antibody based stimulation by anti-CD3/anti-CD28 beads, and chemical stimulation with ionomycin. In addition, the group also showed sequential activation modes in which trapped single cells were exposed to sequential stimulation condition of antigen peptides with varying TCR affinity followed by ionomycin stimulation. Based on the tracking of the cell response histories, they binned the T cells as double responders, single responder (respond only to ionomycin), and no responder.

With the advances in technology, many new and superior techniques become available to us for thorough interrogation of immune cells. As we move from population level analysis into more specialized and personalized ones, there is an urgent need for more single-cell technology that can profile phenotypic, functional, and molecular biomarkers

in high throughput manners. The single-cell technology nowadays, however have targeted and limited utility when it comes to combinatorial profiling. For example, some single-cell technologies as described above can only detect protein secretion or quantify cytolytic efficacy. There is therefore a need to design a platform that can perform multiplexed interrogation of single-cell, in order to obtain a more complete picture of immune cells' capability and polyfunctionality. On this dissertation, we discussed our TIMING technology to look at single-cell cytolysis, motility, and interactions, and combined it with beads assays and microfluidics qPCR to further look at protein secretion and molecular signature of single-cell. This combinatorial approach can potentially bring forth a deeper understanding of immune cells, and may help design new approaches for future clinical trials.

CHAPTER 2

Individual motile $CD4^+$ T cells can participate in efficient multi-killing through conjugation to multiple tumor cells

Note : This is a reformated version of a manuscript accepted at Cancer Immunology Research

Liadi, I., H. Singh, G. Romain, N. Rey-Villamizar, A. Merouane, J. R. Adolacion, P. Kebriaei, H. Huls, P. Qiu, B. Roysam, L. J. Cooper, and N. Varadarajan (2015). Individual Motile CD4+ T Cells Can Participate in Efficient Multikilling through Conjugation to Multiple Tumor Cells. *Cancer Immunol Res* 3: 473-482.

2.1. INTRODUCTION

Chimeric antigen receptors (CARs, check abbreviation and definition sections) are hybrid molecules that typically combine the specificity and affinity of single-chain antibodies with selected intracellular signaling domains of the T-cell receptor (TCR) complex (58-60). When expressed on genetically modified T cells, CARs redirect specificity independent of human leukocyte antigen (HLA) to recognize tumor-associated antigens (TAAs). Second and third generation CARs include the endodomains for co-stimulatory molecules and can thus directly endow the different signals needed for T-cell activation upon binding TAA (61). Initial data from clinical trials at multiple centers reporting the adoptive transfer of T cells genetically modified to express a CD19-specific CAR for the treatment of B-cell malignancies are encouraging, with patients benefiting from complete remissions (62-64). These clinical results have accelerated the clinical translation of T cells bearing CARs targeting TAAs other than CD19 for the treatment of

hematologic malignancies as well as solid tumors (65-67). As a group, these clinical trials differ in the design and specificity of the CARs, the *ex vivo* approach used to manufacture the T cells, the *in vivo* regimen used to pre-treat the recipient, the tumor burden and type, and the T-cell dosing scheme. Thus, drawing conclusions regarding the relative anti-tumor effects between the populations of bioengineered CAR^+ T cells is not readily feasible[1]. One of the hallmarks of a therapeutically successful infusion is the presence of CAR^+ T cells that can persist to execute multiple tumor cells within the tumor microenvironment (68).

In spite of the recent success of adoptive immunotherapy, the mechanistic basis for the potency of a given T-cell product has not been well defined. The majority of adoptive studies have focused on infusing $CD8^+$ T-cell populations because of their ability to directly recognize and lyse tumor cells, thus mediating antitumor immunity (69). In the absence of $CD4^+$ T-cell help however, some infused $CD8^+$ T cells can become functionally unresponsive and undergo apoptosis (70). Indeed, adoptive cell therapy (ACT) protocols that incorporate $CD4^+$ T cells may mediate superior responses, and preclinical and clinical data have established the importance of $CD4^+$ T-cell help during immunotherapy (71, 72). More recently however, adoptive transfer of $CD4^+$ T-cell populations has shown that these cells can mediate regression of established melanoma, and that these cells can differentiate into cytolytic effectors (73-75). Despite these advances direct comparisons of the potency and kinetics of interactions between donor-derived populations of $CD4^+$ T cells and tumor cells at single-cell resolution, and the comparison to $CD8^+$ T cells is lacking.

Although two-photon microscopy studies are well suited for understanding the mechanistic basis of T-cell tumor cell interactions *in vivo*, direct observation of killing and motility is restricted to tens of events that may lead to sampling bias. Additionally, these

studies are limited in throughput and cannot be used to routinely determine the interactions between cellular infusions and tumor cells. *In vitro* dynamic imaging (53, 76-80) systems are well-suited for studying the longitudinal interactions between cells at single-cell resolution, in a defined environment. Here, we have employed Timelapse Imaging Microscopy In Nanowell Grids (TIMING) to analyze the longitudinal interactions between individual CD19-specific T cells (effectors, E) expressing a second generation CAR with one or more $CD19^+$ tumor cells (target(s), T). To the best of our knowledge, we demonstrate for the first time that $CD4^+CAR^+$ T cells (CAR4 cells) can directly engage in multi-killing via simultaneous conjugation to multiple tumor cells. The major differences between CAR4 and $CD8^+$ CAR^+ T cells (CAR8 cells), at the single-cell, in mediating tumor-cell lysis *in vitro*, was the kinetics of killing, and this was attributed to the differences in their intracellular Granzyme B (GzB) content. Surprisingly, in both sets of T cells, a minor sub-population of individual T cells identified by their high motility, demonstrated efficient killing of single tumor cells. By comparing both the multi-killer and single killer CAR^+ T cells it appears that the propensity and kinetics of T-cell apoptosis was modulated by the number of functional conjugations. Our results demonstrate that the ability of CAR^+ T cells to participate in multi-killing should be evaluated in the context of their ability to resist AICD.

2.2. METHODS

2.2.1. Human subjects statement. All work outlined in this report was performed according to protocols approved by the Institutional Review Boards at the University of Houston and the University of Texas M.D. Anderson Cancer Center.

2.2.2. Cell lines and antibodies. All antibodies were purchased from Biolegend (San Diego, CA). Human pre-B cell line NALM-6 (ATCC), Daudi-β2m (ATCC), T-cell lymphoma EL-4 (ATCC) and modified $CD19^{+}$EL-4 cells were cultured as described previously (81, 82). The cell lines were routinely tested to ensure that they were free of mycoplasma contamination and flow-cytometry was utilized to confirm the expression of CD19.

2.2.3. Genetic modification and propagation of cells: PBMC from healthy volunteers were electroporated using Nucleofector II (Amaxa/Lonza) with DNA plasmids encoding for second generation CAR (designated CD19RCD28) and SB11 transposase and co-cultured with γ-irradiated K562 aAPC (clone 4) for 28 days along with cytokines (IL-2 and IL-21) in a 7-day stimulation cycle as described previously (81). For single cell analysis, frozen CAR^{+} T cells were revived and re-stimulated with irradiated K562 aAPC before using them in experiments.

2.2.4. Flow cytometry: Cells were stained for cell surface markers (CAR, CD4, CD8, CD3), fixed and permeabilized (Cytofix/Cytoperm, BD Biosciences) for 20 min at 4^{0}C. Cells were subsequently stained for intracellular granzyme B in perm/wash buffer at 4^{0}C for 30 min, acquired on a FACS Calibur, and analyzed using FCS Express/FlowJo as previously described (81). Statistical analyses for determining GzB expression were performed within R.

2.2.5. End-point cytotoxicity assay. Nanowell array fabrication and the corresponding cytotoxicity assay to interrogate effector-target interaction at single-cell level were performed as described previously (78). Briefly, CAR^{+} T cells labeled for 5 minutes with 1 μM of red fluorescent dye, PKH26 (Sigma) and target cells labeled for 5 minutes with 1

μM of green fluorescent dye PKH67 were co-loaded onto nanowell arrays at a concentration of 10^6 cells/mL. Images were acquired on a Carl Zeiss Axio Observer fitted with a Hamamatsu EM-CCD camera using a 10x 0.3 NA objective. Automated image acquisition of the entire chip was performed at 0 and 6 hour and apoptosis was identified by staining with AnnexinV conjugated to Alexa-647 (Life Technologies, Carlsbad, CA).

2.2.6. TIMING assays. Nanowell grids were fixed in position on a 60 mm petridish. The cells were labeled and loaded exactly as described for the end-point assay and imaged on a Zeiss Axio Observer using a 20x 0.45 NA objective. Images were acquired for 12-16 hours at intervals of 7-10 minutes.

2.2.7. Statistical analysis. P-values were calculated using GraphPad Prism software and asterisks were assigned as follows: * $P<0.05$, ** $P< 0.01$, *** $P< 0.001$, and **** $P< 0.0001$

2.2.8. Flow cytometry based cytotoxicity assay: CAR4 cells ($1x10^6$ cells) were incubated with $CD19^+$ target cells ($0.2x10^6$ cells; Daudiβ_2m, NALM-6, CD19EL-4) at E:T ratio of 5:1 in the presence or absence of 5mM EGTA in 24-well plates in 5% CO_2 at 37°C for 6 hours. Following incubation cells were stained for CD3 (T cells) and CD19 (tumor targets), acquired on a FACS Calibur (BD Biosciences) and analyzed using FCS Express version 3.00.007 (Thornhill, Canada).

2.2.9. Image processing and cell segmentation: In order to permit accurate computation of cell displacements despite camera and stage movements, the individual nanowells were detected automatically with >99% accuracy by correlating pre-constructed shape templates at the expected range of orientations and magnification values. The correlation

value is a maximum at the well centers, and these points are detected using a local maxima clustering algorithm. The cells in each image channel are analyzed automatically using a 3-step method (83). First, each pixel is stratified as bright foreground, intermediate foreground, and dark background based on modeling image intensities as a mixture of three Gaussian distributions. The foreground pixels are subjected to multi-level thresholding (we used 10 equally-spaced levels between the maximum and minimum foreground intensity values). The cell centers are detected using a local maxima clustering on the average of Euclidean distance maps computed at each threshold. Using these cell centers, the image foreground is partitioned into individual cell regions using the normalized cuts algorithm, allowing cell sizes and shapes to be quantified. Spectral overlap between the dyes used under the imaging conditions were eliminated during image processing through our automatic "unmixing" process, and this is performed independently for each set of experiments. In addition, the segmentation scripts calculate an integrated fluorescence intensity by averaging on all the pixels associated with a given cell and thus eliminated any ambiguity in effector/target classification due to the diffusion of dyes across the cell membrane during contact.

2.2.10. Cell tracking: The detected cells, denoted $C_{i=1..N}^{t=1...T}$, where N is the number of cells in the well and T is the number of frames, are tracked from frame to frame using a graph-theoretic edge selection algorithm on a directed graph where cells correspond to vertices and edges represent temporal association hypotheses (84). The association cost for each edge $f_{i,j}^{t}$ between object i at time t and object j at time $t+1$ is calculated based on cell location and size. The temporal correspondences are identified using an integer programming algorithm that maximizes the total association cost subject to constraints to

ensure that each cell in a given frame is associated with a maximum of one cell in the subsequent frame, and vice versa.

2.3 RESULTS

2.3.1 Production and phenotype of CAR$^+$ T cells: Genetically modified and propagated T cells were generated from the peripheral blood mononuclear cells (PBMC) of healthy volunteer donors derived using the *Sleeping Beauty* (SB) system (85) to enforce expression of a second generation CD19-specific CAR (designated CD19RCD28) that activates T cells via a chimeric CD3 and CD28 endodomain (**Figure 10**).

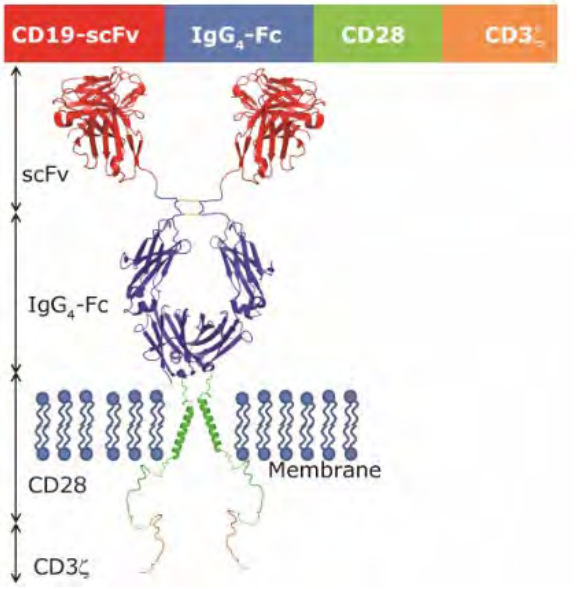

Figure 10: Schematic of second-generation CD19-specific CAR (CD19RCD28) that signals through chimeric CD28/CD3-ζ

Subsequent to expansion, CAR$^+$ T cells from two separate donors contained predominantly CD8$^+$ T cells (**Figure 11**).

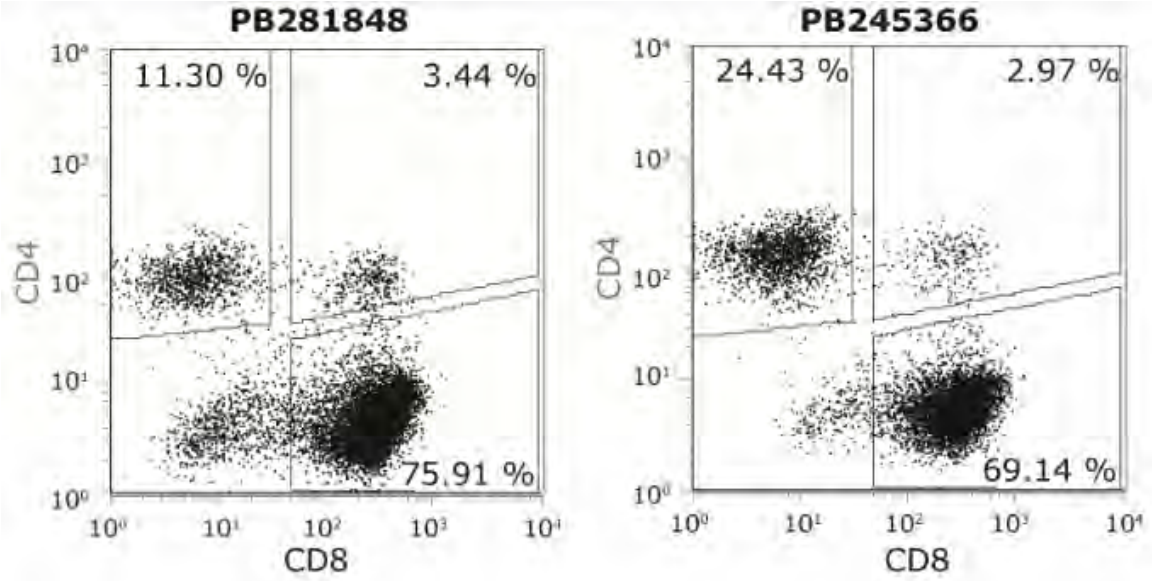

Figure 11: Phenotypic characterization of the CAR$^+$ T cells from two separate donors.

The approach to producing the CAR$^+$ T cells mirrors our manufacture in compliance with current good manufacturing practice for human application (**Figures 12 and 13)**. Briefly, peripheral blood mononuclear cells (PBMC) were electroporated with plasmids encoding for the Sleeping Beauty (SB) transposase and the transposon containing the CAR. The electroporated cells were subsequently expanded by co-culture with K562-derived artificial antigen presenting cells (aAPC) modified to express CD19, CD64, CD86 and CD137L, in the presence of exogenous IL-21 and IL-2. CD19RCD28 T cells showed >10^4 fold expansion in culture over a period of 4 weeks. Inferred cell counts were calculated assuming all viable cells were carried forward through each stimulation cycle. The error bars represent standard deviation from three independent measurements.

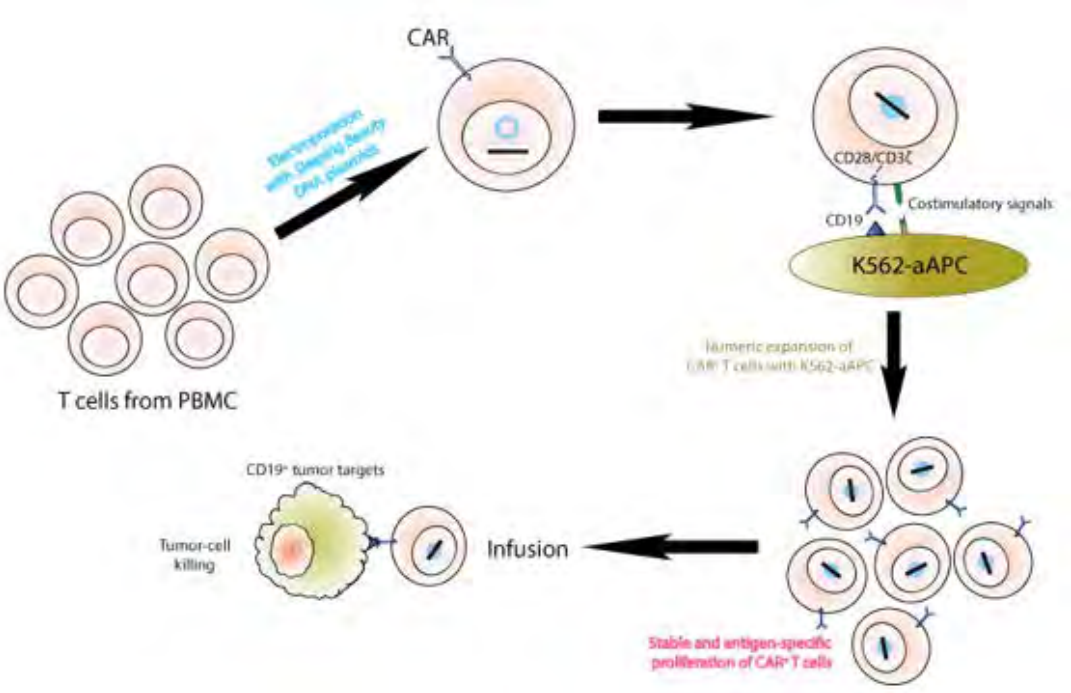

Figure 12: Genetic modification and expansion of CAR$^+$ T cells.

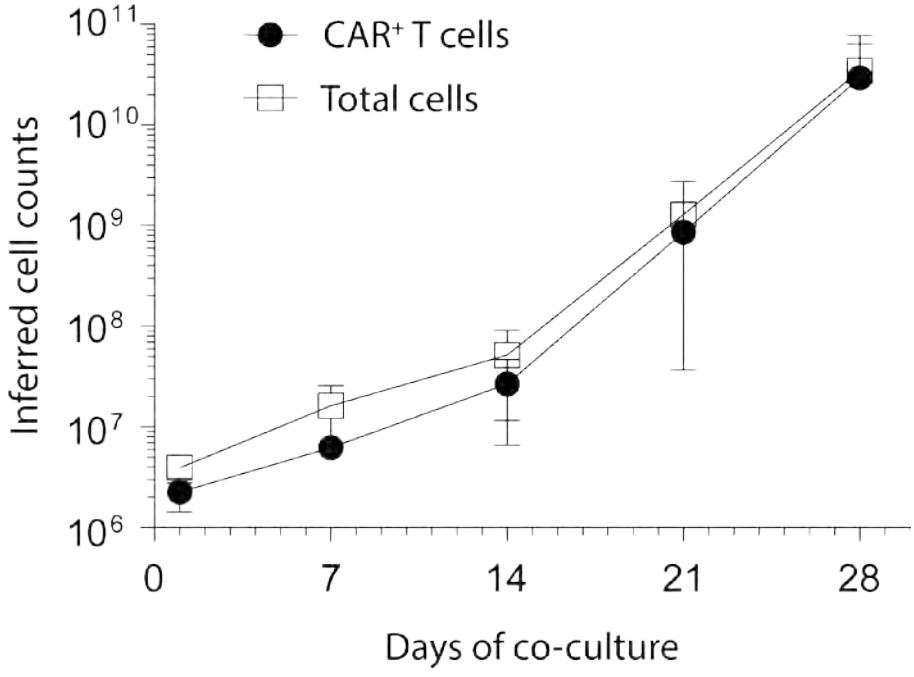

Figure 13: Representative data from a single donor showing expansion of CAR$^+$ T cells on aAPC in the presence of soluble IL-21 and IL-2.

2.3.2 The cytotoxic potential, specificity and multi-killing ability of individual CAR⁺ T cells: Donor-derived CAR⁺ T-cell populations were evaluated for their ability to lyse CD19⁺EL4 target cells, by co-culture within nanowell grids (**Figures 14 and 15**). Labeled effectors and target cells are loaded onto a nanowell array (~85,000 individual wells, 125pL each well) to enable monitoring of T-cell function at the single-cell level. Subsequent to loading and washing steps, the entire chip is immersed in cell-culture media containing AnnexinV. A pre-image is acquired on the microscope to determine the occupancy of every single nanowell and to exclude cells dead at the start of the assay.

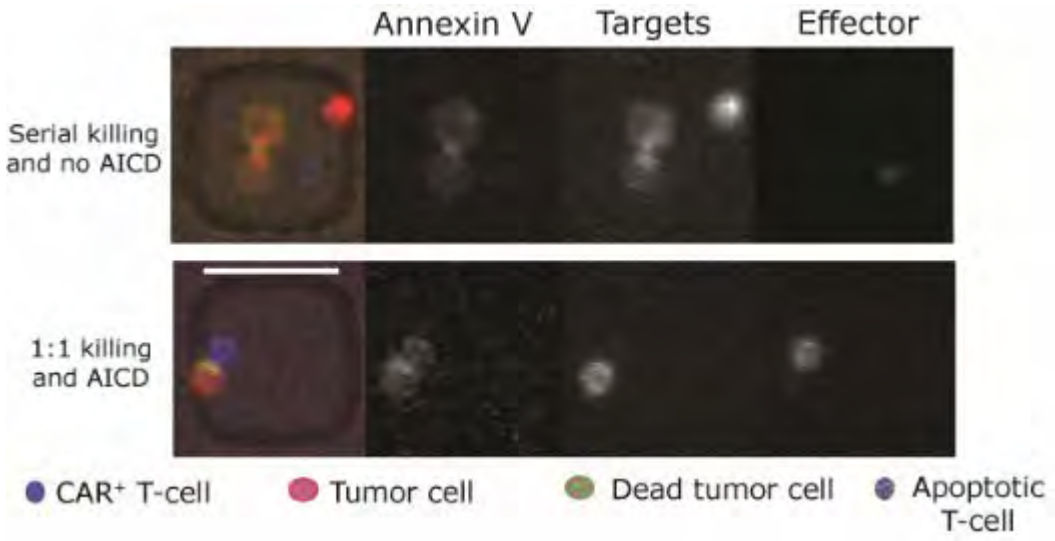

Figure 14: Representative composite micrographs illustrating the ability of single CAR⁺ T cells to kill, and to undergo apoptosis, when incubated with tumor cells. Scale bar 50 µm.

The array is then transferred to the incubator for 6 hours to enable cell-cell interactions and a second post-image is acquired. In house image segmentation programs are used to automatically process the images and database matching is employed to determine killing. In parallel, a separate nanowell array is loaded with targets only to determine the death rate in the absence of effectors, over the same period of time. The

killing assay results are corrected for the background killing rate determined by the target only arrays.

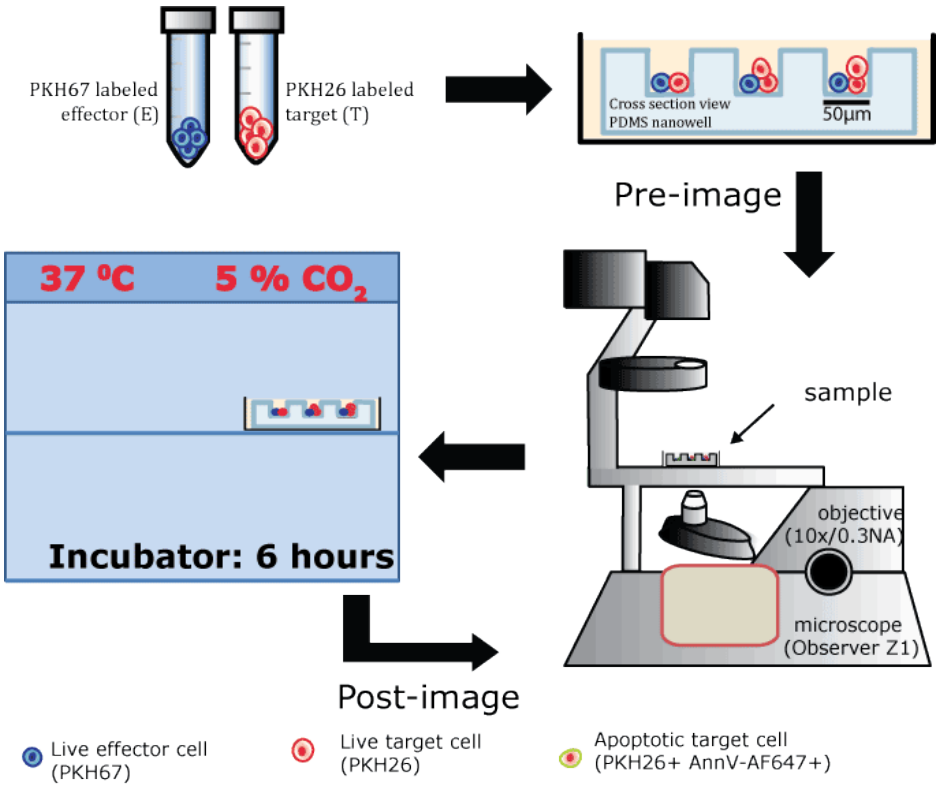

Figure 15: High-throughput cytotoxicity assay for monitoring T-cell target cell interactions in nanowell grids.

At an E:T of 1:1, averaged across both donors, 29% of single CAR^+ T cells induced apoptosis of (number of events, N_{total} = 4,048) $CD19^+$EL4 cells within six hours, whereas they induced apoptosis of just 1% (N_{total} = 3,682) of $CD19^-$EL4 cells in the same time frame. The >29-fold increase of lysis of $CD19^+$ versus $CD19^-$ targets confirms TAA-specific lysis (**Table 1,** p-value <0.0001, Fisher's 2x2 test). In parallel, a conventional 4-hour ^{51}Chromium release assay (CRA) was performed at the same E:T ratio (1:1) and reported a similar overall magnitude of target cells killing (mean 14-fold increase of lysis of $CD19^+$ versus $CD19^-$EL4 cells), albeit without single-cell resolution (**Table 1**).

Table 1: Comparison of the cytolytic responses measured by the single-cell assay and population-level 51Cr release assay, at an E:T ratio of 1:1. The numbers in parentheses report the total number of events

Effector : Target (E:T) ratio 1:1

Sample	Single-cell cytotoxicity assay			^{51}Cr release assay		
	$CD19^{pos}$	$CD19^{neg}$	NALM-6	$CD19^{pos}$	$CD19^{neg}$	NALM-6
PB281848	0.22 (2525)	0.02 (2692)	0.30 (3102)	0.17	0.00	0.16
PB245366	0.35 (1523)	0.01 (990)	0.37 (401)	0.39	0.05	0.40

The ability to redirect specificity to lyse human $CD19^+$ tumor cells was confirmed using the pre-B cell line NALM-6 (**Figure 16**).

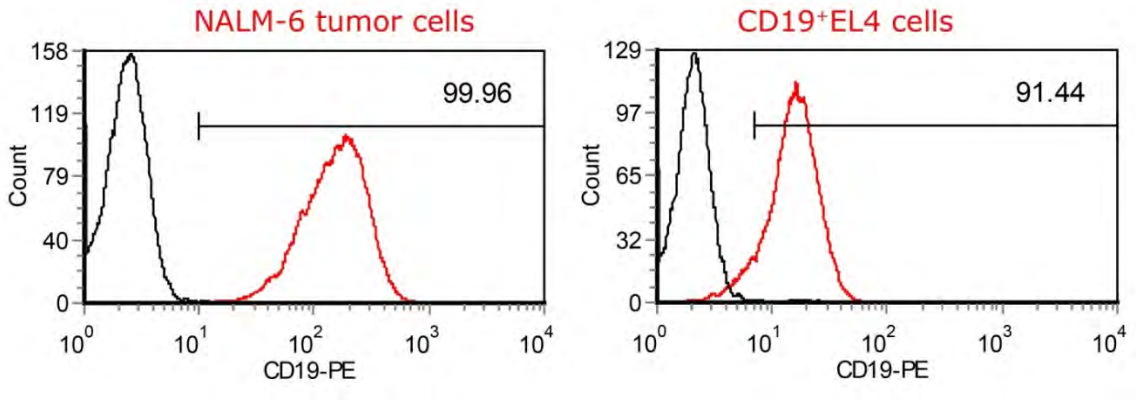

Figure 16: CD19 expression on NALM-6 tumor cells or $CD19^+$EL4 target cells as determined by immunofluoresecent staining. The parental EL4 cell line was used as a negative control (black lines).

When averaged across both donors, within six hours of observation, individual CAR^+ T cells induced apoptosis in 34% (N_{total} = 3,503) of NALM-6 target cells at an E:T ratio of 1:1. Across all of the samples tested, single cell assay demonstrated a linear correlation to the CRA (**Table 1**, r^2 = 0.84, p-value = 0.01). The ability of individual T cells to eliminate more than one target cell was quantified by analyzing nanowells containing multiple targets (**Table 2**). The tumor-cells are colored red, the CAR^+ T cells

are labeled blue with an artificial white exterior. Killing is determined by the colocalization of Annexin V staining (green) on red target cells. Scale bar 50 µm.

Table 2: Composite micrographs illustrating representative examples of the interactions between single CAR$^+$ T cells (E) and one or more NALM-6 tumor (T) cells.

Number of Targets	Possible outcomes			
	0 killed	1 killed	2 killed	3 killed
1	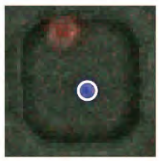	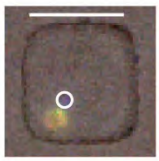		
2	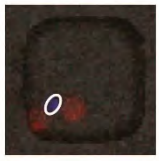		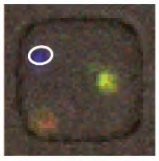	
3		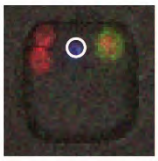		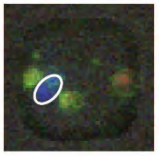

Averaged across both donors, at an E:T ratio of 1:2, within six hours, 21% (N_{total} = 2,294) of single CAR$^+$ T cells killed exactly one CD19$^+$EL4 target-cell whereas 23% killed both targets (**Figure 17**). During this same timeframe, at an E:T ratio of 1:3, 22% (N_{total} = 1,108) of single CAR$^+$ T cells killed exactly one target, 22 % killed exactly two targets, and 9% killed all three targets (**Figure 17**).

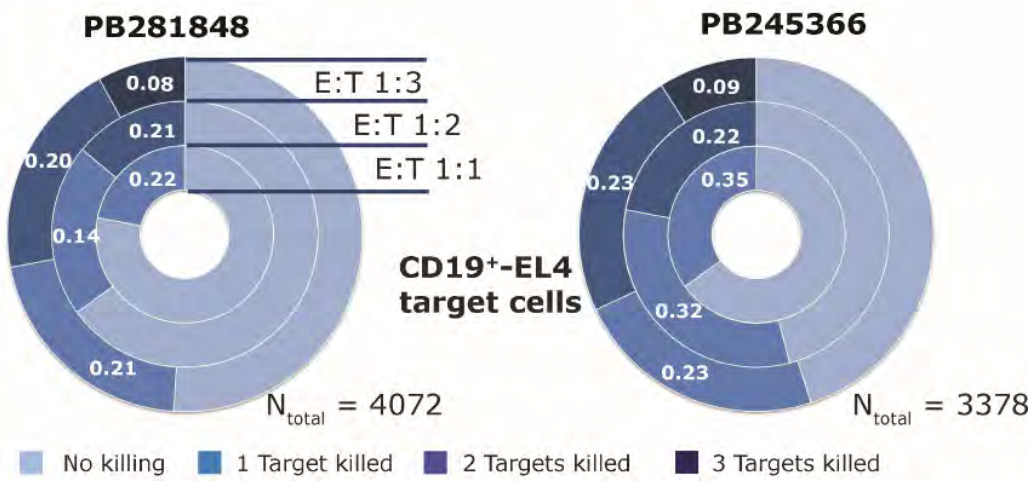

Figure 17: Donut plots summarizing the frequency of killing outcomes of the interaction between CAR$^+$ T cells, derived from these two donors, and CD19$^+$EL4 target cells.

Thus, within a defined observation window, the likelihood that an individual CAR$^+$ T cell killed more than one tumor cell improved as the number of targets within the nanowell increased but this might simply reflect higher frequency of interactions at higher cell densities (**Figure 18**).

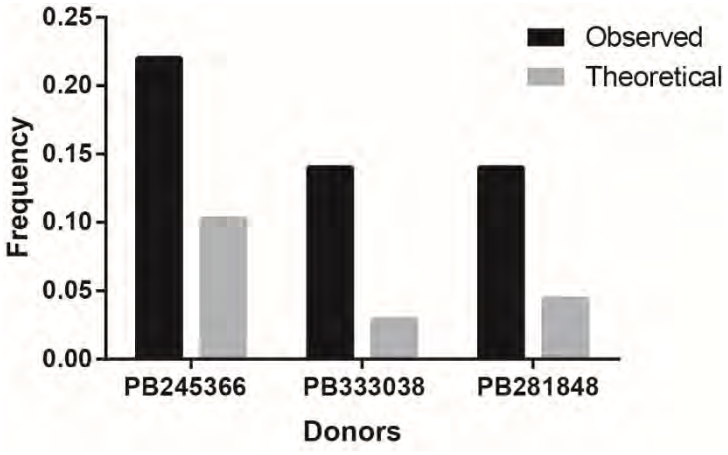

Figure 18: Comparisons of the observed killing frequencies at an E:T ratio of 1:2, and theoretical frequency, defined as the square of the frequency of killing

These findings were also observed when substituting NALM-6 as target cells, albeit with diminished frequency of multi-killing after 6 hours of co-culture (**Figure 19**).

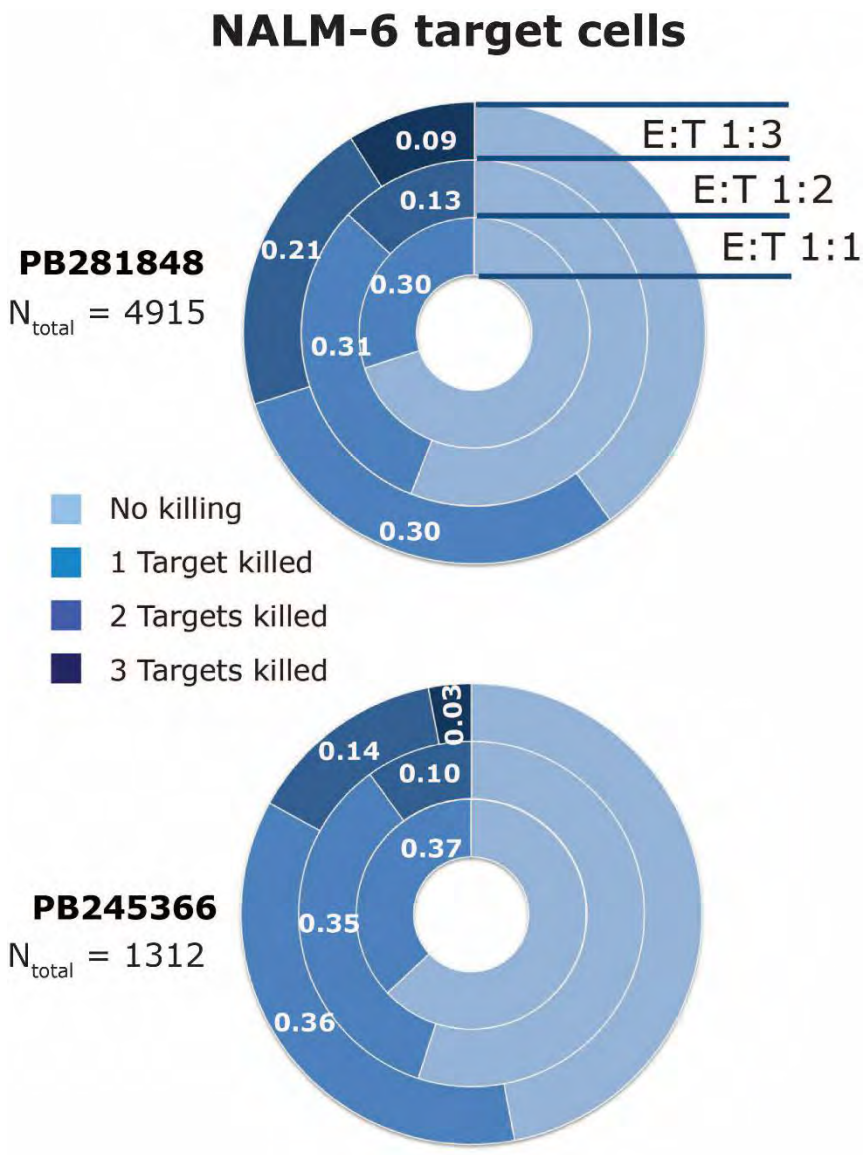

Figure 19: Donut plots summarizing the outcomes of the interaction between individual CAR8 cells and 1-3 CD19$^+$–NALM-6 tumor cells.

In aggregate, these data demonstrate that the responses measured by the single-cell assay are consistent with the results of CRA, and that multi-killer CAR$^+$ T cells (ability to lyse at least two targets) comprised 20% (N_{total} = 3,402) of the CAR$^+$ T-cell population.

2.3.3. Motile CD8⁺ cytotoxic T cells are efficient killers with decreased potential for activation induced cell death (AICD)

In order to gain an improved mechanistic understanding on the interaction between individual CAR⁺ T cells and NALM-6 tumor cells, we developed and implemented TIMING (**Figure 20**).

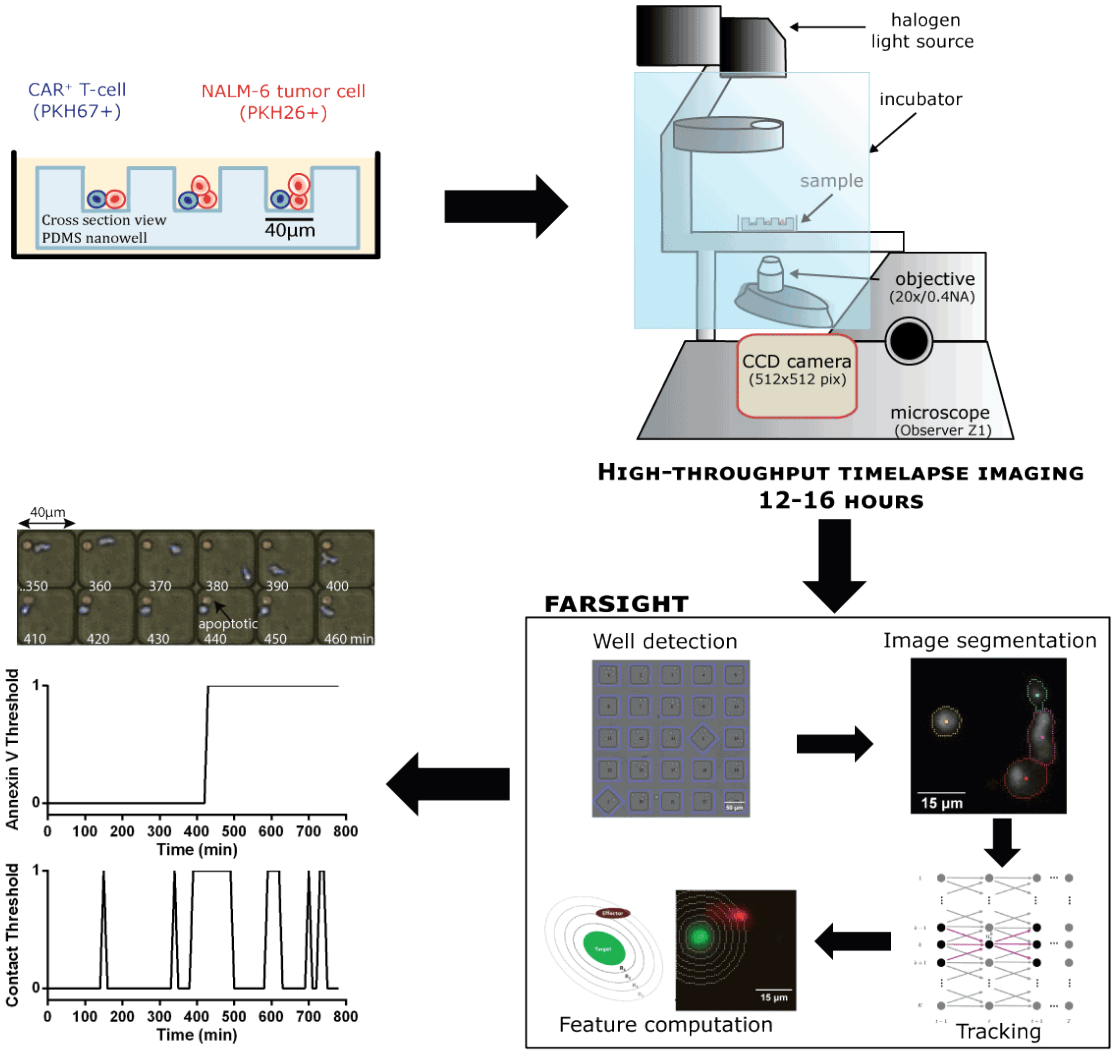

Figure 20: Timelapse Imaging Microscopy In Nanowell Grids (TIMING).

PDMS nanowell arrays (64 pL each nanowell) are fabricated to bond a 60mm petridish. Labeled effectors and targets are loaded onto the nanowell array and the entire chip is immersed in cell-culture media containing fluorescent Annexin V. At least 6,000 nanowells are imaged every 7-10 minutes on the microscope for a total of 12-16 hours. Subsequently, an integrated pipeline within FARSIGHT is implemented to automatically enable well detection, image preprocessing and cell segmentation, tracking and feature computation. The images are fragmented such that each nanowell represents a single time series file. When analyzing time series data, only nanowells that yielded the exact same number of effectors and targets in >95% of time points were carried forward for analysis. Finally, the data is presented as time-series plots for each well along with the associated cell feature graphs.

Six parameters describing T-cell intrinsic behavior motility (d_{Well}) and aspect ratio of polarization (AR), conjugation (contact lasting >7 minutes, t_{Seek} and $t_{Contact}$), and death (t_{Death} and t_{AICD}) were computed to define each interacting pair of effector and tumor cell (**Figure 21-23**).

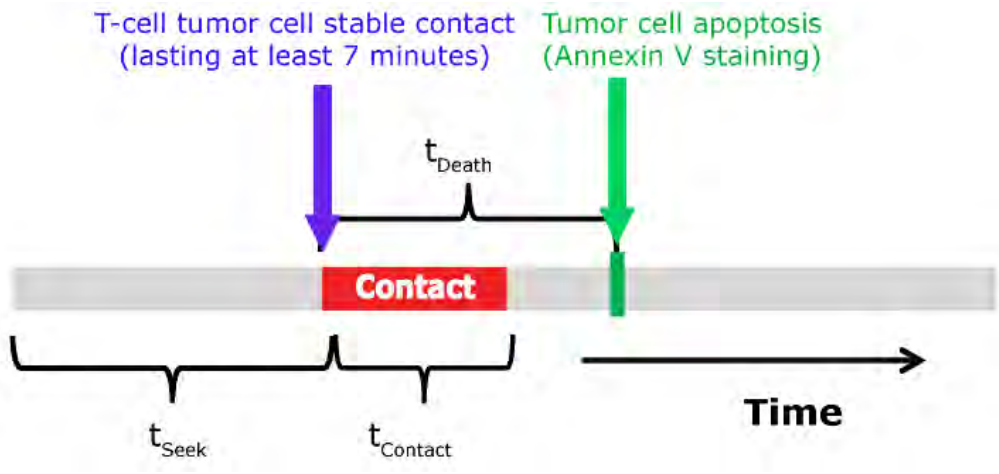

Figure 21: Schematic depicting t_{seek}, $t_{contact}$, and t_{death}. Red bar indicates periods of conjugation.

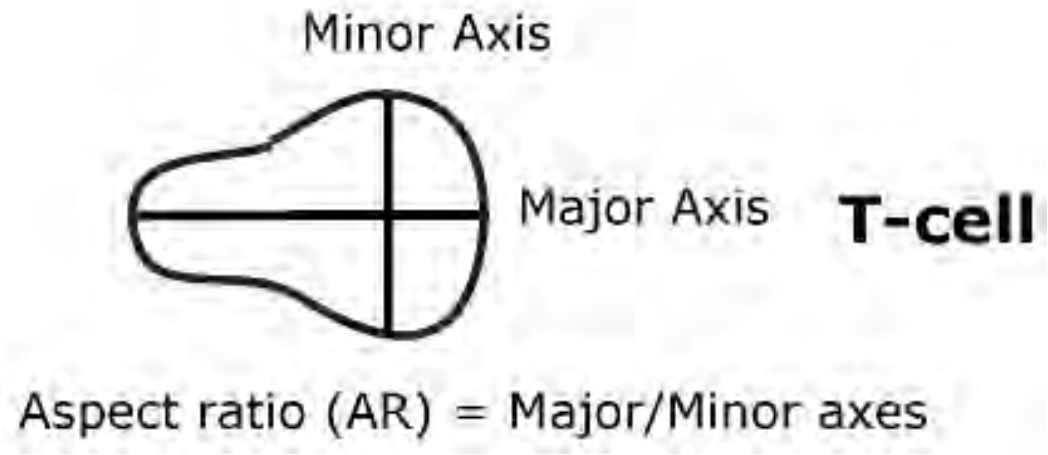

Figure 22: Aspect ratio of polarization describes the ratio of major and minor axis fitted to an ellipse.

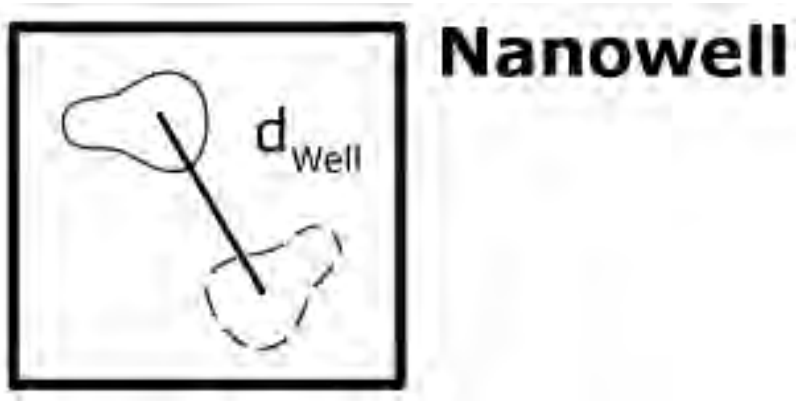

Figure 23: d_{Well} represents the average displacement of the centroid of the effector cell between successive seven minute time points.

At an E:T of 1:1, 77 % (N_{total} = 268) of single $CD8^+CAR^+$ T cells (CAR8 cells) that made at least one conjugate were able to kill the engaged leukemia cell. In order to identify subgroups of T cells that exhibited different behavioral interactions with the tumor cells leading to subsequent killing, the time series data for each of three features, total duration of conjugation, d_{well} and AR, underwent hierarchical clustering (**Figure 24**) (86).

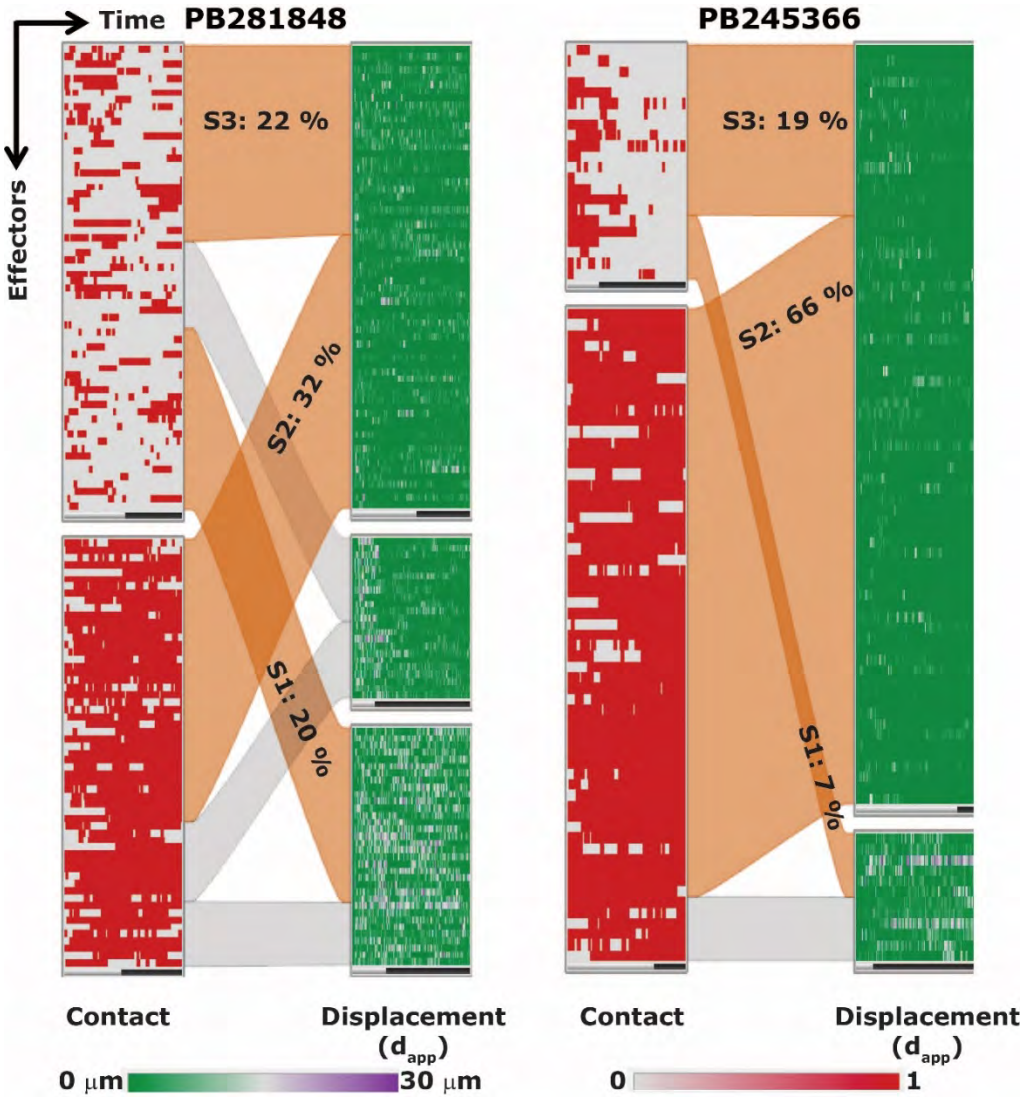

Figure 24: Identification of subgroups of killer CAR8 cells based on their motility and contact behavior with tumor cells at E:T of 1:1.

The time series of the contact pattern of CAR8 cells in their interaction with NALM-6 cells was clustered using K-means clustering (Euclidean distance, complete linkage) to identify low and high contact duration subsets. The displacement (d_{well}) of the CAR8 cells was independently clustered to yield two or three subsets using K-means (Euclidean distance, complete linkage). Since these are features of the same cells, Caleydo was used to visualize the linkage between the clusters (gray cables) at single-cell resolution. The frequency of each of the three subsets, S1-S3, is highlighted in orange.

Three T-cell subgroups were described that collectively accounted for 70% of the single-killer CAR8 cells: S1 (14% [7-20%], range), low conjugation and high motility; S2 (49% [32-66%]), high conjugation and low motility; and S3 (21% [19-22 %]), low conjugation and low motility (**Figure 24**). The high-motility subgroup, S1, comprised predominantly of elongated T cells that had an initial "lag-phase" (t_{Seek} 184±38 minutes, Mean±SEM), but formed stable conjugates ($t_{Contact}$ 98±13 minutes) prior to target apoptosis (t_{Death} 204±35 minutes) (**Figures 25 and 26**). On the figures, Each circle represents a single cell. P-values were computed using parametric one-way ANOVA. (* P<0.05, ** P< 0.01, *** P< 0.001, and **** P< 0.0001)

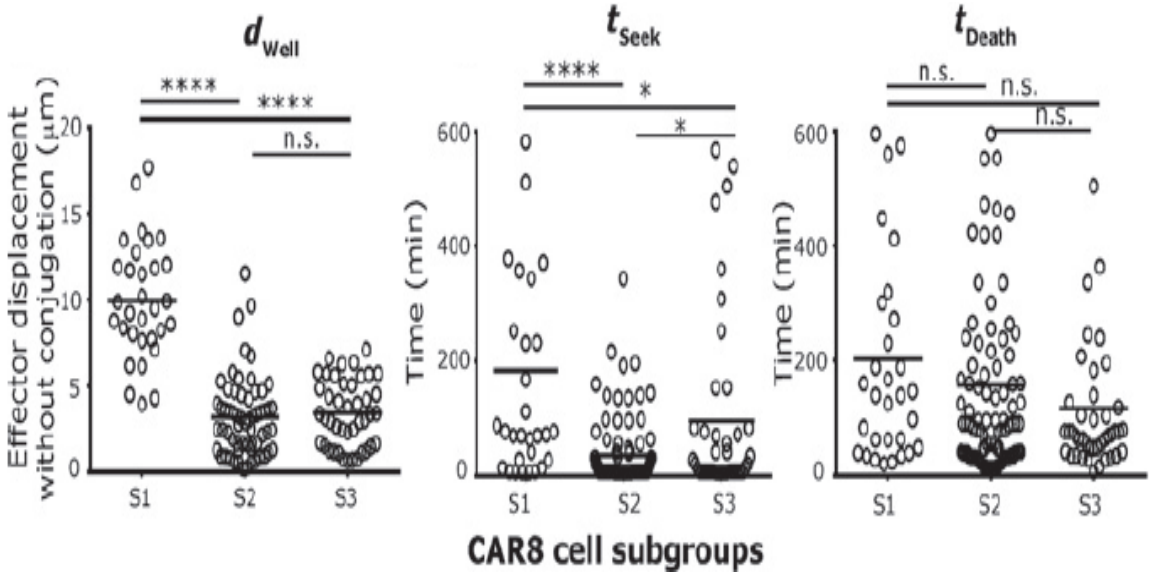

Figure 25: Mean motility, time to first conjugation, and killing efficiency of single CAR8 cells three different subgroups.

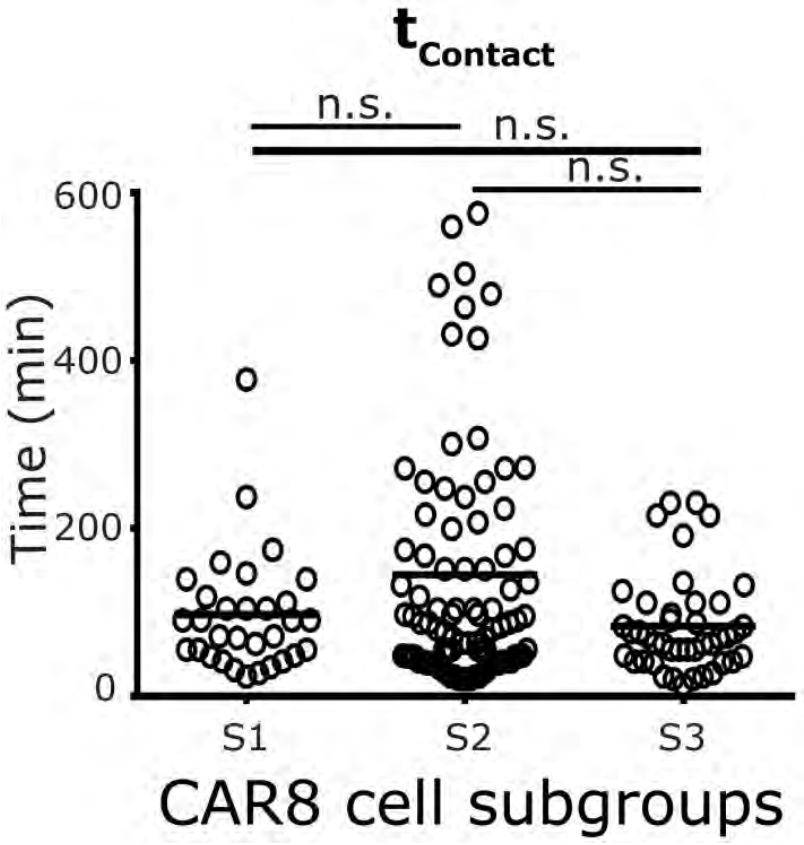

Figure 26: At an E:T of 1:1, the total duration of conjugation prior to NALM-6 tumor cell killing is no different for the CAR8 cells in the different subgroups.

Predominantly, these T cells exhibited a decrease in motility and increased circularization (**Figure 27**) during tumor-cell conjugation, detached after tumor-cell death, resumed normal migratory function and had only a low frequency of effector cells undergoing AICD (**Figure 28**). On Figure 18 and 19, each circle represents a single-cell and the horizontal black line designates the mean of the population. P-values were determined using a pairwise two-tailed t-test on both figures (S1 were excluded from analysis in Figure 19 due to low number of apoptotic effectors).

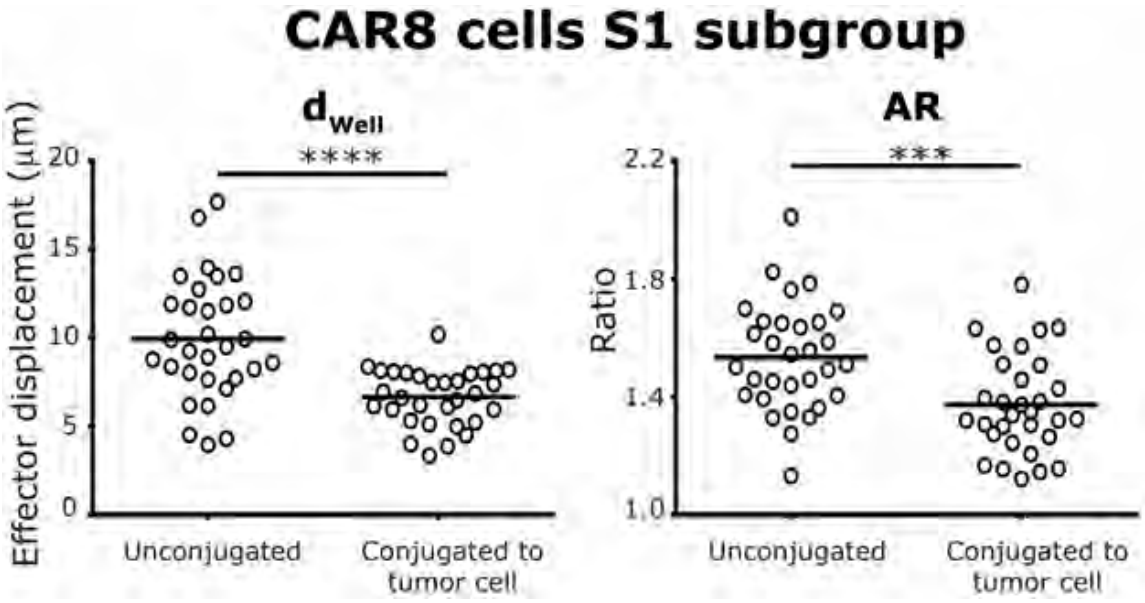

Figure 27: At an E:T ratio of 1:1, CAR8 cells in the S1 subgroup, demonstrate drop in motility and increased circularization upon conjugation to NALM-6 tumor cell.

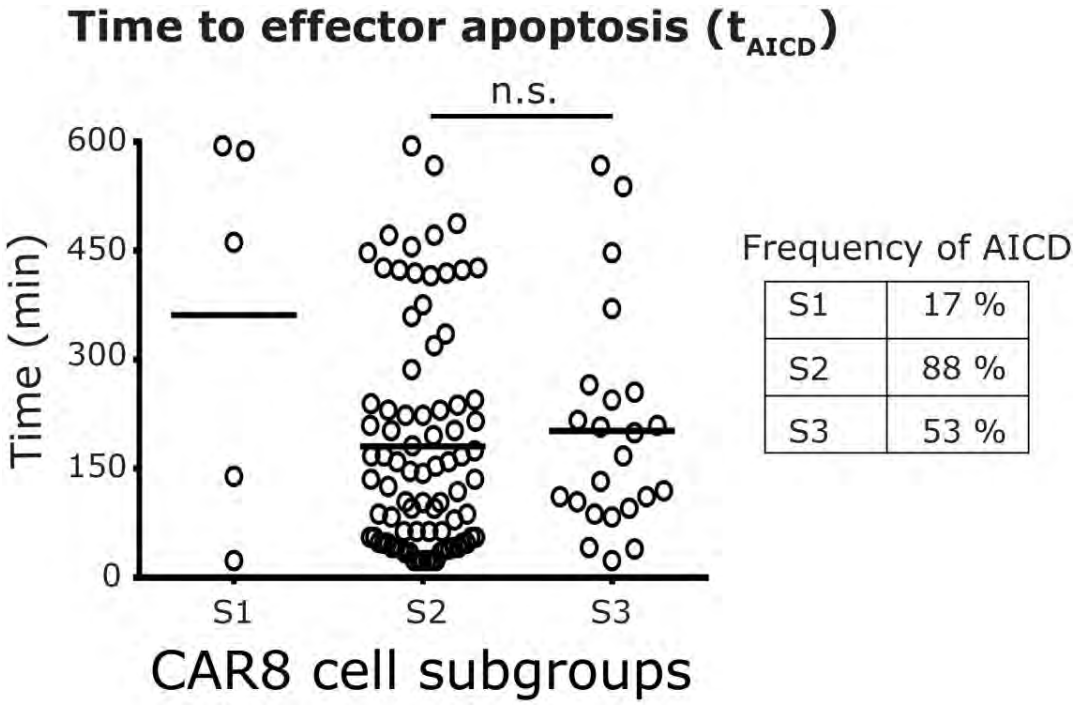

Figure 28: At an E:T ratio of 1:1, CAR8 cells in the different subgroups demonstrate different frequencies and kinetics of AICD subsequent to the interactions with NALM-6 cells.

The representative cell in the dominant subgroup, S2, established conjugation quickly (t_{Seek} 36±6 minutes), and displayed sustained conjugation ($t_{Contact}$ 145±16 minutes) prior to killing (t_{Death} 158±18 minutes) (**Figures 25**). The majority of these T cells did not detach or resume migratory function after tumor-cell lysis, retained a predominantly circular morphology, and continued to remain conjugated >10 hours, even subsequent to the death of the conjugated tumor-cell. Moreover, 88% of S2 effector cells underwent apoptosis within the first ten hours of observation (**Figure 28**). Finally, T cells in the S3 subgroup were rapid killers ($t_{Contact}$ 84±8 minutes and t_{Death} 118±20 minutes) that arrested after conjugation but failed to resume migration after tumor-cell detachment/killing (**Figure 25**). Although these S3 effectors detached from tumor-cells after delivering the lethal hit, 53% then underwent apoptosis (**Figure 28**). Taken together these results demonstrate that at an E:T ratio of 1:1, the dominant subgroup of cells, S2, identified by their lack of motility and early conjugation to tumor cell, underwent AICD. On the contrary, highly motile CAR8 cells, S1, detached efficiently and resumed exploration of the local microenvironment, indicating that the motility of CAR8 cells might help identify efficient killers with decreased propensity for AICD. The observation that the majority of the CAR8 cells (S2 subgroup) maintained extended contact even after the death of the tumor cell is consistent with investigations on HIV-specific CTLs (87).

2.3.4. CAR8 cell motility at increased tumor-cell densities facilitates multiplexed killing:

The efficacy of CAR^+ T cells to eliminate tumor burden in excess of the number of effectors infused is due to their ability to persist and participate in serial killing(68). To facilitate identification of multi-killers, we next profiled the interactions in nanowells containing a single CAR8 cell and 2 to 5 NALM-6 tumor cells (E:T 1:2-5). The frequency of CAR8

cells that were able to simultaneously conjugate to two or more tumor cells increased from 25% to 49% as the number of targets within the nanowell increased, indicating that multiplexed killing might be important (**Figure 29**).

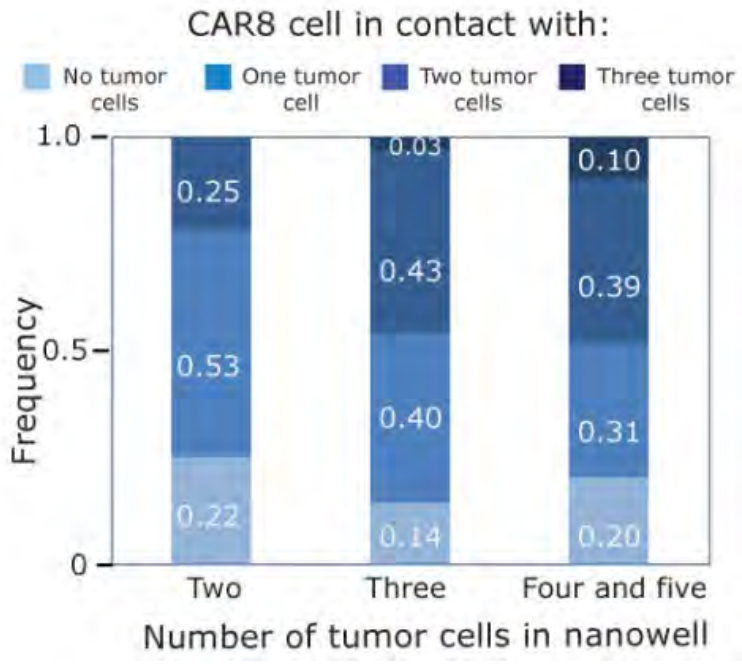

Figure 29: Distribution of the number of simultaneous conjugations of individual CAR8 cells when incubated with increasing number of NALM-6 tumor cells.

The frequency of simultaneous tumor conjugates that result in tumor cell deaths (46% [43-50%]) was not very different from true serial killers that attach, kill, detach and attach to a different tumor cell (49% [44-53%]), suggesting that CAR8 cells are capable of eliciting either mode of killing, likely dependent on tumor cell density. Individual multi-killer CAR8 cells (N_{total} = 70) demonstrated only a small decrease in motility when conjugated to one tumor cell but showed no significant change in motility upon conjugation to multiple tumor cells (d_{Well}(unconjugated): 5.9±0.5 µm vs d_{Well} (single target): 4.6±0.3 µm vs d_{Well} (two targets): 4.7±0.3 µm) (**Figure 30**).

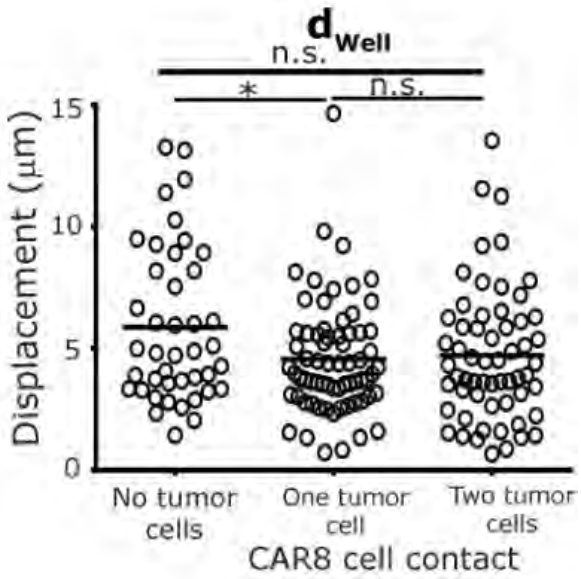

Figure 30: The mean motility of individual multi-killer CAR8 cells. P-values for multiple comparisons were computed using parametric one-way ANOVA.

The only difference for multi-killers when contacting the different tumor cells was in their time to establish conjugates (t_{Seek} $Target_1$: 18±4 minutes vs $Target_2$: 98±13 minutes, **Figure 31**).

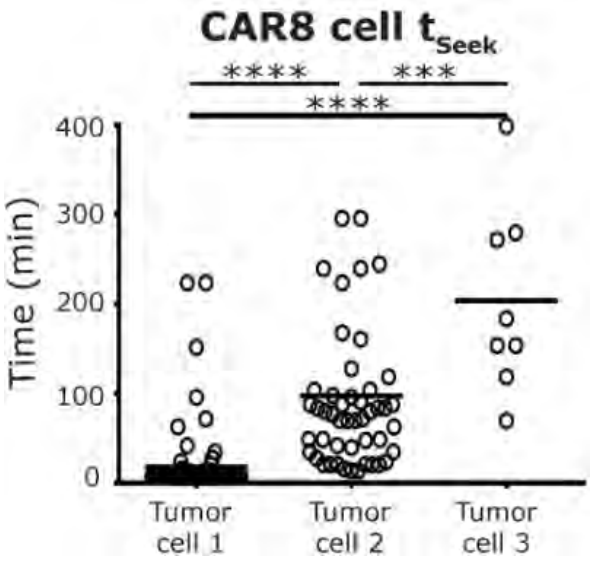

Figure 31: The mean time to first conjugation of individual multi-killer CAR8 cells. P-values for multiple comparisons were computed using parametric one-way ANOVA.

Both, duration of conjugation ($t_{Contact}$Target$_1$: 101±9 minutes vs Target$_2$: 113±15 minutes) and killing efficiency (t_{Death}Target$_1$: 156± 17 minutes vs Target$_2$: 177±24 minutes) were no different (**Figure 32 and 33**).

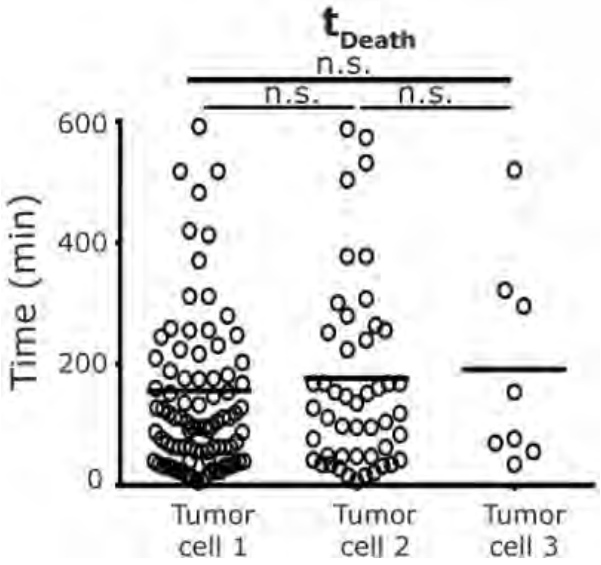

Figure 32: The mean killing efficiency of individual multi-killer CAR8 cells. P-values for multiple comparisons were computed using parametric one-way ANOVA.

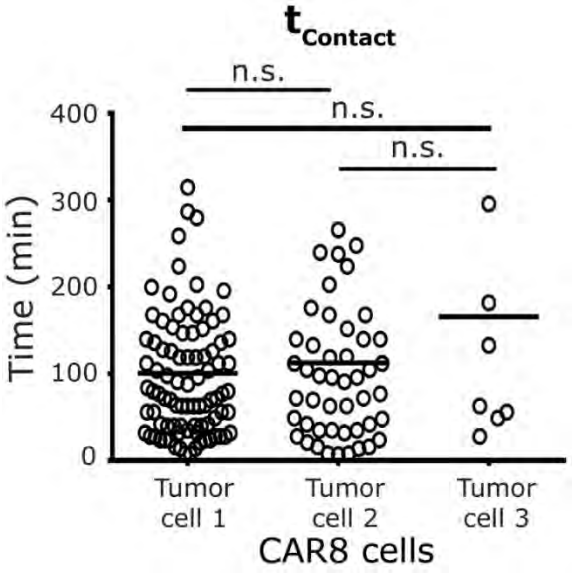

Figure 33: At an E:T ratio of 1:2-5, multi-killer CAR8 cells demonstrate no significant differences in their duration of conjugation prior to killing multiple NALM-6 tumor cells.

In addition to contact duration, the number of CAR8 cell tumor cell conjugations that lead to killing during encounter with the first tumor cells (61% both donors) was also not significantly different from the number of conjugations that resulted in target cell killing during encounter with the second tumor cell (74% [70-79 %]). These TIMING data suggest that the efficiency to kill a second tumor cell is largely unaffected by the hit on a first target (p-value >0.99). Furthermore, in comparison to single killer CAR8 cells, multi-killer CAR8 cells displayed greater motility when conjugated to the tumor cell despite the increased crowding because of higher tumor cell density, (**Figure 34**).

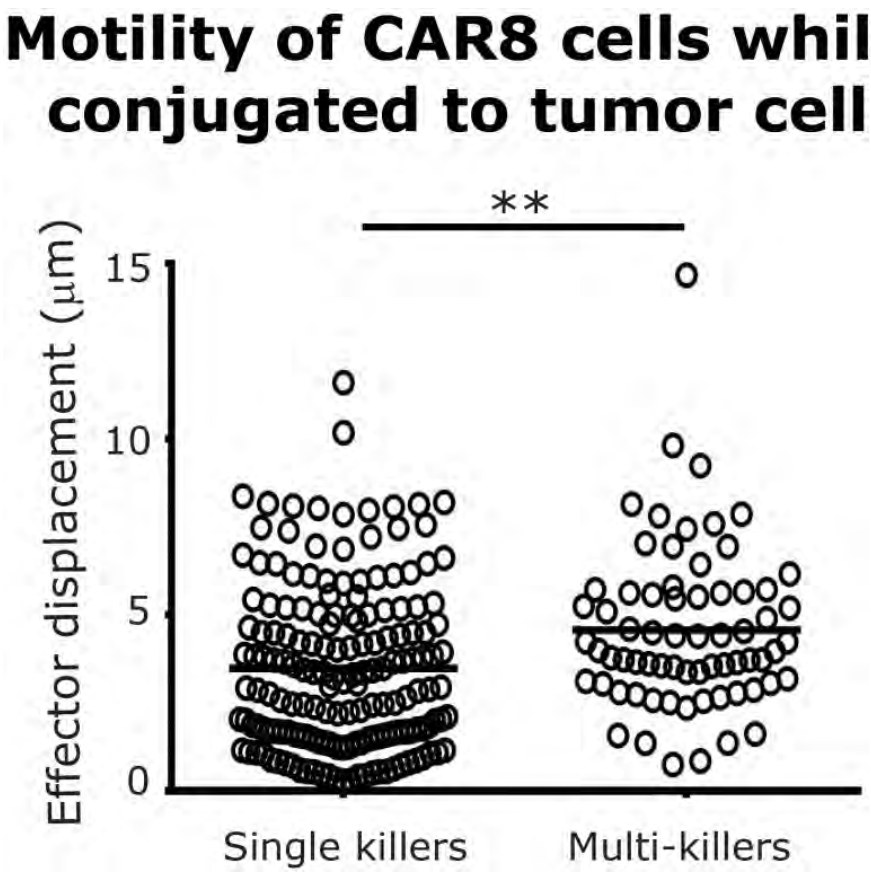

Figure 34: Multi-killer CAR8 cells displayed greater motility when conjugated to tumor cell in comparison to single-killer CAR8 cells that encountered only a single tumor cell despite wells crowding.

2.3.5. Motility can identify a subgroup of CAR4 cells with enhanced cytotoxic efficiency.

We have previously reported that the culture of CAR^+ T cells in the presence of IL-2 and IL-21 on aAPC can lead to outgrowth of CAR4 cells with cytotoxic potential (81). In order to facilitate comparisons to CAR8 cells, and to demonstrate that CAR4 can directly participate in killing and multi-killing, the interaction of individual CAR4 cells from two donor-derived populations (**Figure 35**), with NALM-6 tumor cells were profiled using TIMING.

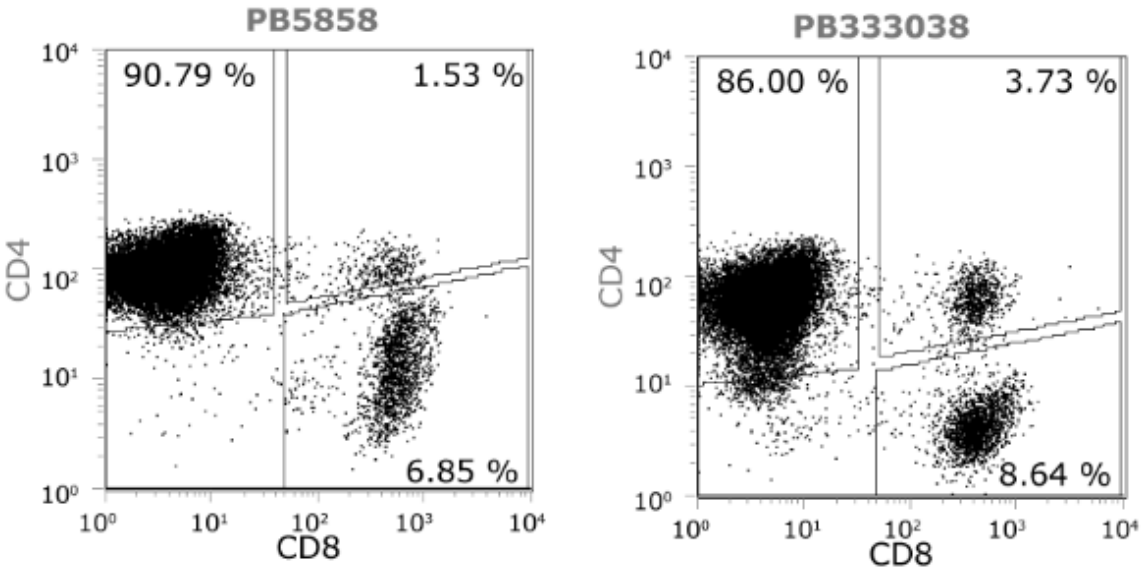

Figure 35: Phenotypic characterization of the CAR^+ T cells from two separate donors that comprise of predominantly $CD4^+CAR^+$ T cells.

At an E:T ratio of 1:1, 55% (N_{total} = 549) of single CAR4 cells that conjugated to a NALM-6 cell subsequently killed the tumor cell. As with the CAR8 cells, the interaction behavior of CAR4 cells with the NALM-6 cells could be classified into three subgroups, S1-S3 (**Figure 36**).

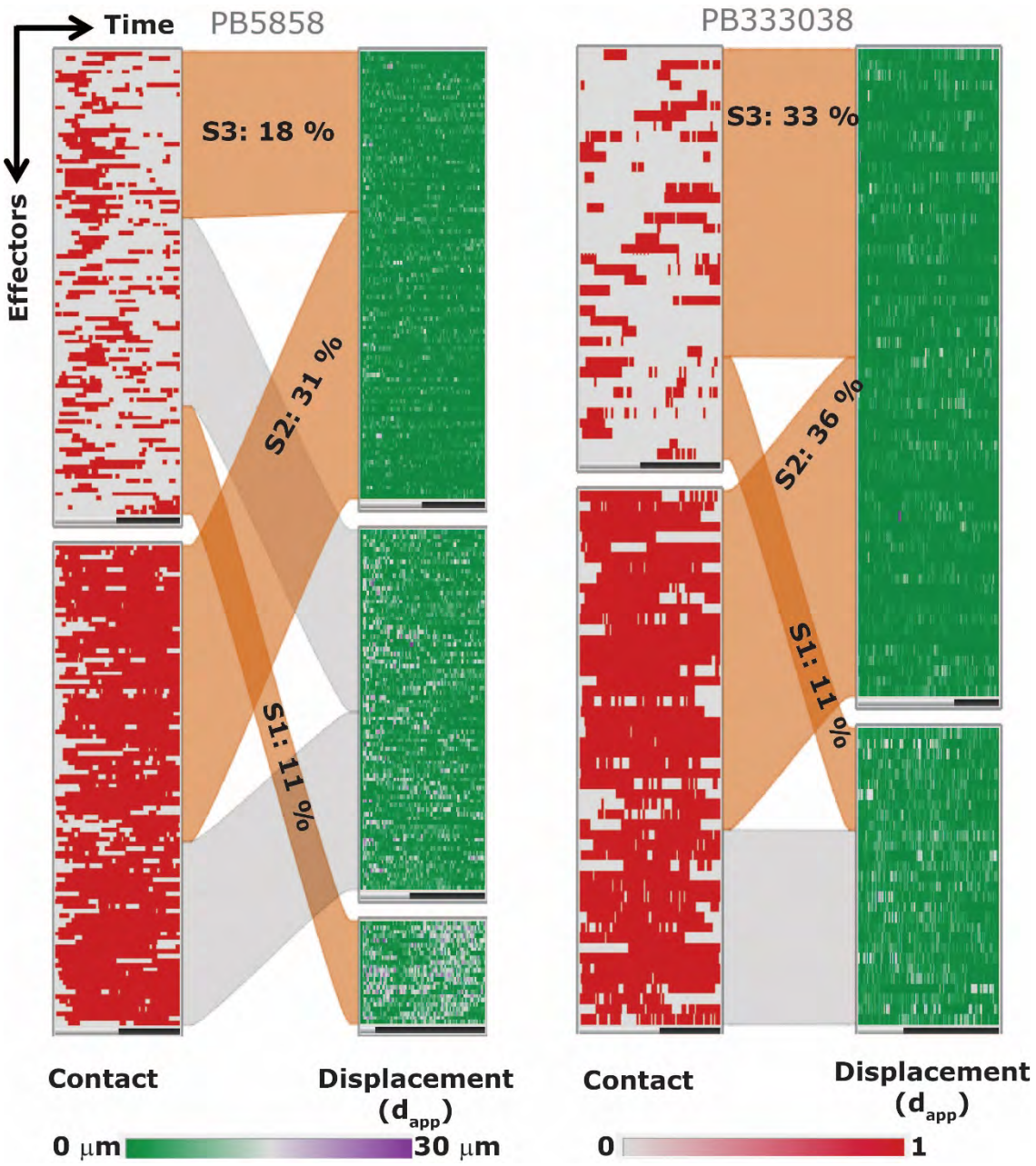

Figure 36: At an E:T ratio of 1:1, identification of subgroups of killer CAR4 cells based on their motility and contact behavior with tumor cells

CAR4 cells in the enhanced motility subgroup, S1 (11% both donors), displayed significantly faster kinetics of tumor cell death (t_{Death} 157±17 minutes) compared to the dominant S2 (34% [31-36 %]) subgroup (t_{Death} 318±23 minutes, **Figure 37-39**).

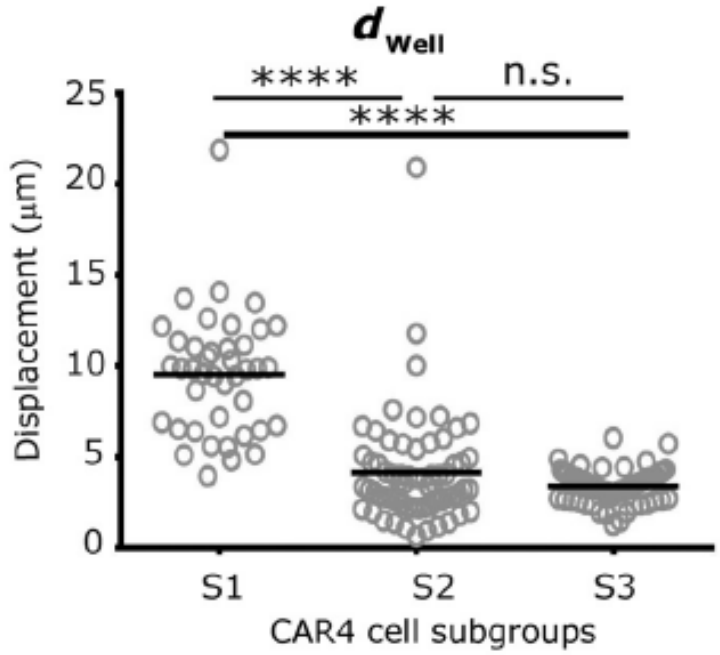

Figure 37: The mean motility of single CAR4 cells in each of three different subgroups.

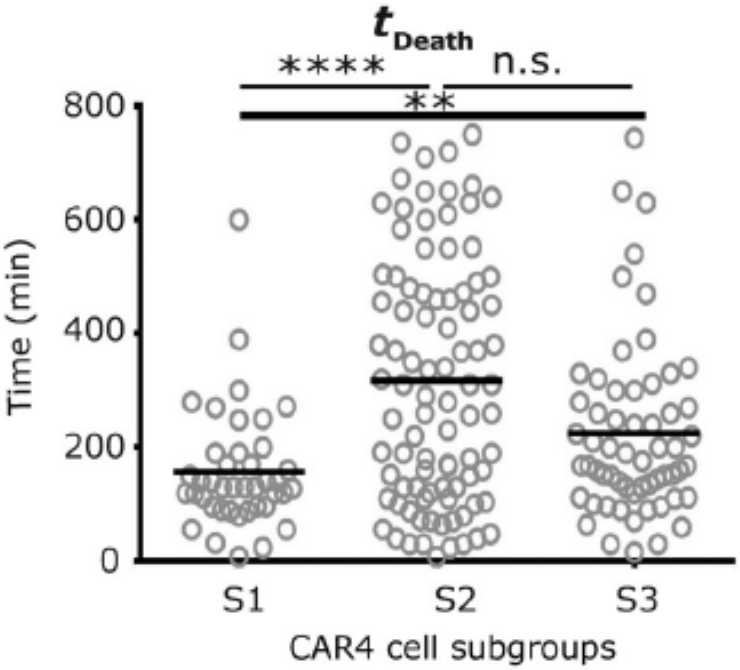

Figure 38: The mean killing efficiency of single CAR4 cells in each of three different subgroups.

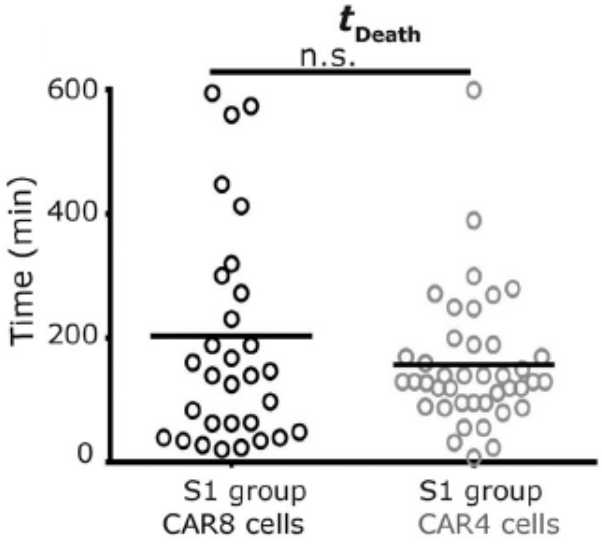

Figure 39: Comparison of the means of the killing efficiencies between single CAR8 and CAR4 cells within the S1 subgroups.

This increased kinetic efficiency was consistent with the decreased conjugation time required by the S1 subgroup of cells ($t_{Contact}$ 122±11 minutes) in comparison to the S2 subgroup ($t_{Contact}$ 300±21 minutes) (**Figure 40**).

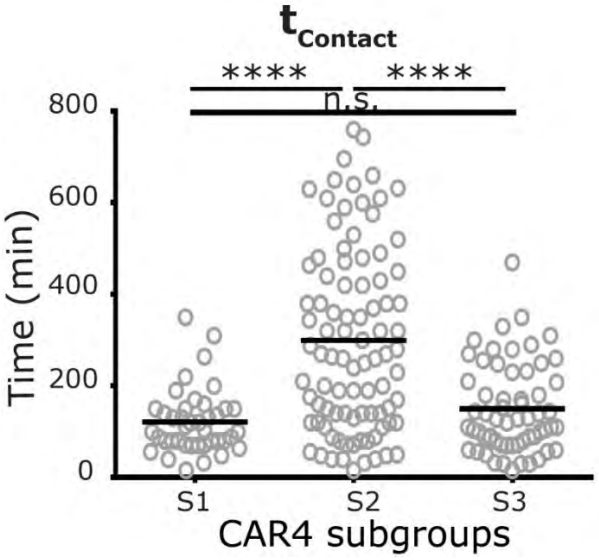

Figure 40: At an E:T of 1:1, the total duration of conjugation prior to NALM-6 tumor cell killing is significantly longer for CAR4 cells in S2 subgroup in comparison to subgroups S1 and S3.

These results suggest that similar to CAR8 cells, the motility of the CAR4 cells may help identify the most efficient killers.

2.3.6. Both single-killer and multi-killer CAR4 cells required longer conjugation and demonstrated delayed kinetics of killing in comparison to CAR8 cells.

At the E:T ratio of 1:1, comparisons of the killing efficiency of CAR4 cells (t_{Death} 284±11 minutes) and CAR8 cells (163±12 minutes) demonstrated that individual CAR4 cells on average required two extra hours to induce tumor cell death (**Figure 41**).

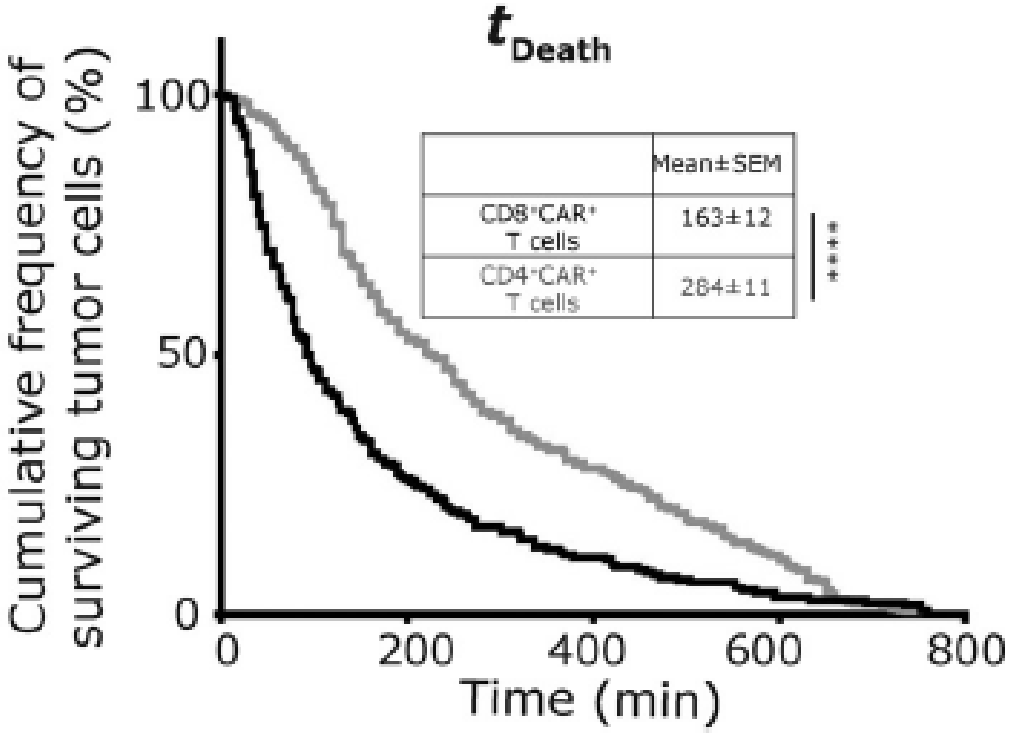

Figure 41: Comparative Kaplan –Meier estimators depicting the differences in killing efficiencies of the entire population of CAR4 cells and CAR8 cells.

Consistent with the observation that the S2 subgroup is the dominant population of CAR^+ T cells, CAR4 cells in the S2 subgroup (t_{Death} 318±23 minutes) demonstrated delayed

kinetics of killing in comparison to CAR8 cells within the S2 subgroup (t_{Death} 158±18 minutes) (**Figure 42**).

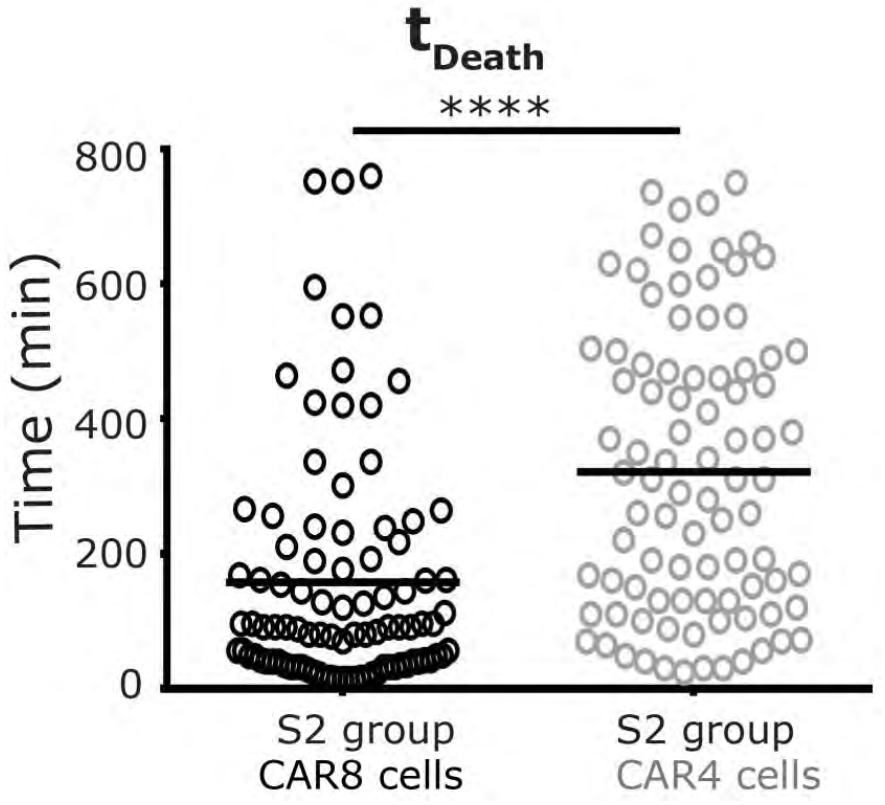

Figure 42: At an E:T of 1:1, CAR4 cells in S2 subgroup induce apoptosis in tumor cells with delayed kinetics in comparison to CAR8 cells in the S2 subgroup.

As mentioned above, since the motility of CAR4 cells could be used to identify the most efficient killers (**Figure 38**), comparisons of the kinetic efficiency of CAR4 cells in the S1 subgroup (t_{Death} 157±17 minutes) with CAR8 cells in the S1 subgroup (t_{Death} 204±34 minutes) demonstrated no significant differences. This further supports the notion that motility might be a useful parameter in identifying efficient cytolytic CAR^+ T cells. Comparisons of the single-cell behavioral interactions of multi-killer CAR4 cells (N_{total} = 78) with the CAR8 cells demonstrated that most features were conserved across cells of

both phenotypes. First, the unconjugated motility of CAR4 cells (d_{well} 6.9±0.5 µm) was no different than CAR8 cells (d_{well} 5.9±0.5 µm, **Figure 43**).

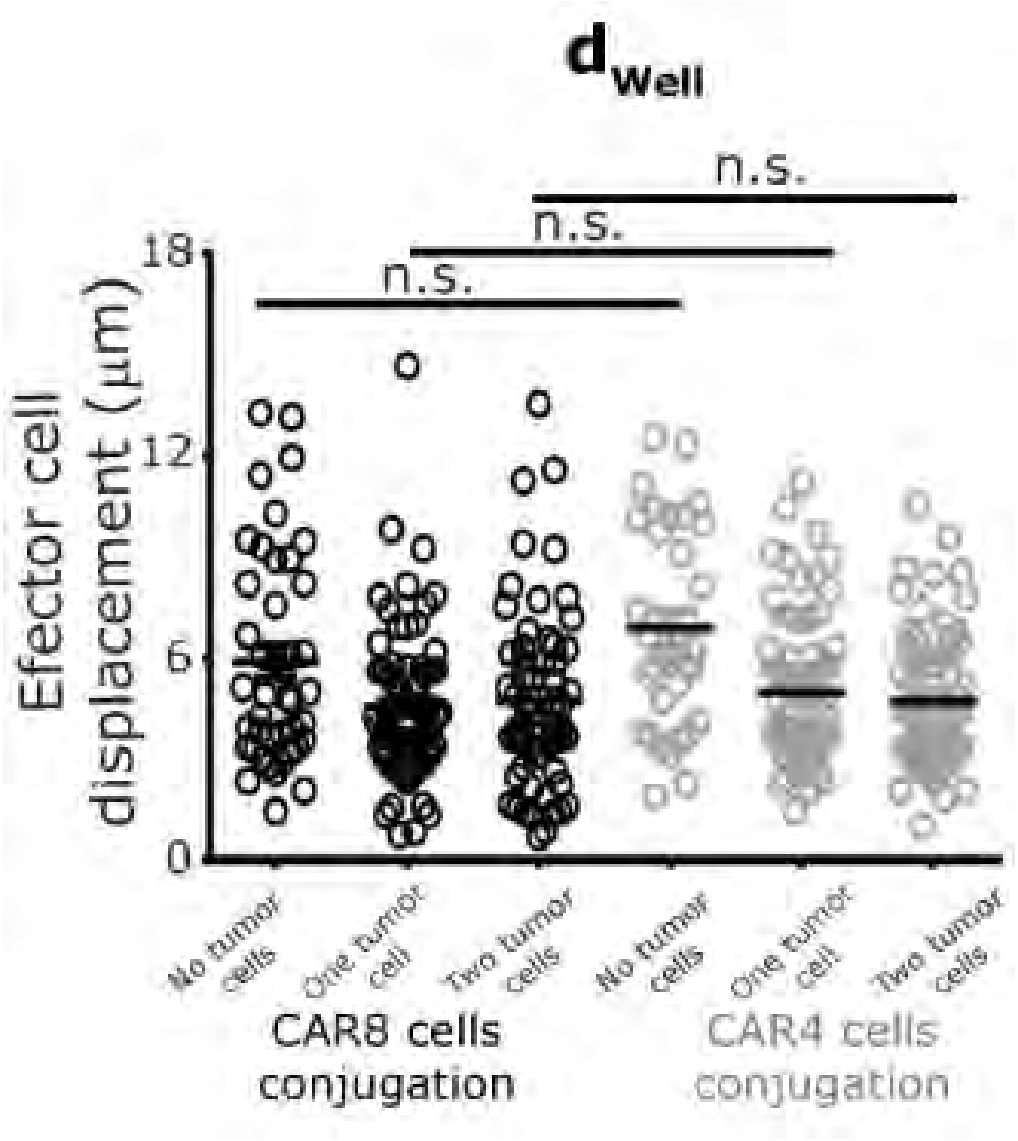

Figure 43: Comparisons between the mean motility of single multi-killer CAR8 cells and CAR4 cells.

Second, like CAR8 cells, CAR4 cells demonstrated a matched decrease in motility (**Figure 43)** and increased circularization when conjugated to one or more tumor cells **(Figure 44**).

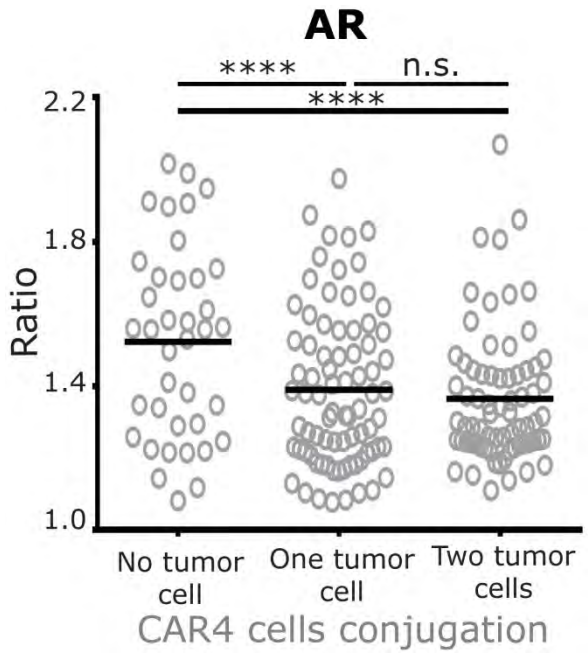

Figure 44: At an E:T ratio of 1:2-5, multi-killer CAR4 cells demonstrate increased circularization upon contact with one or more NALM-6 tumor cells.

Third, the preferred contact mode of the multi-killer CAR4 cells was also simultaneous conjugations to multiple tumor cells (**Figure 45**).

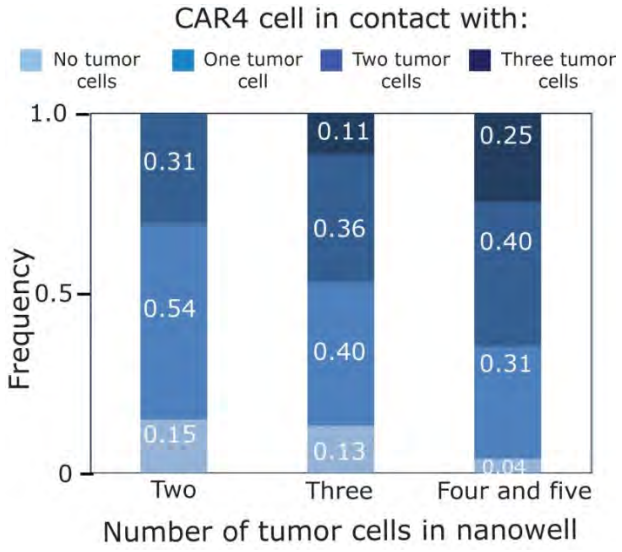

Figure 45: The ability of individual CAR4 cells to simultaneously conjugate to multiple NALM-6 tumor cells increases as the number of tumor cells within the nanowell increases.

Fourth, simultaneous conjugates that result in killing accounted for 61% [60-63%] of multi killing events, indicating that this is an important mode of killing intrinsic to T cells and not just $CD8^+$ T cells. Fifth, comparisons of t_{Death} for the different tumor cells killed by individual multi-killer CAR4 cells demonstrated no differences (**Figure 46**).

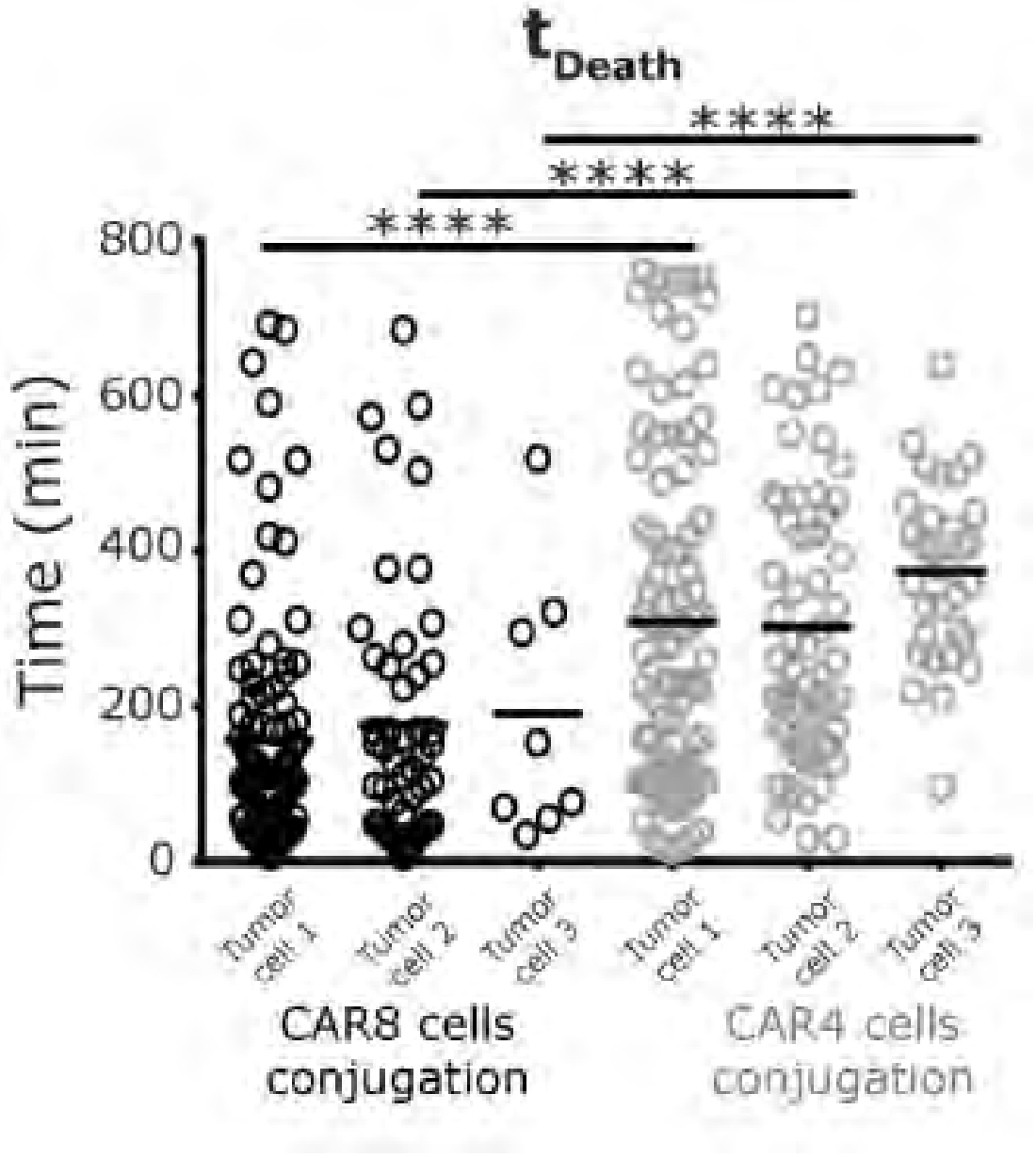

Figure 46: Comparisons between the mean killing efficiency of single multi-killer CAR8 cells and CAR4 cells.

Lastly, the number of CAR4 cell tumor cell conjugations that lead to killing during the first tumor cell encounter (60% [58-61 %]) is not significantly different from the number of contacts that leads to killing when encountering the second tumor cell (60% [57-63 %]), suggesting that the killing efficiency is unchanged.

Consistent with the observations at an E:T of 1:1, multi-killer CAR4 cells required extended conjugation ($t_{Contact}$ 214±18 minutes) and demonstrated slower kinetics prior to killing the first tumor cell (t_{Death} 310±23 minutes) in comparison to CAR8 cells (**Figure 46**). In aggregate, these results demonstrate that the major difference in CAR4 cells and CAR8 cells participating in either single killing or multi-killing is the kinetics of tumor cell death.

2.3.7. Intracellular GzB content can explain differences in killing efficiency.

To test the hypothesis that the varying efficiencies both between cells of the same population and in comparing CAR4 cells with CAR8 cells might be due to differences in expression of cytotoxic enzymes, we employed intracellular staining at the single-cell level using flow cytometry to identify the expression GzB within these cells. To establish baseline controls, the intracellular GzB content of $CD3^+CD4^+$ cells (2.36±0.01) and $CD3^+CD8^+$ cells (3.89±0.04) in PBMC of two separate donors was determined (**Figure 47**).

CAR4 cells (from donors PB5858 and PB333038) and CAR8 cells (from donors PB243566 and PB281848) were profiled using mAb against CD4/CD8/CAR and GzB. Consistent with our previous reports, both CAR4 cells (38.6±0.2) and CAR8 cells (267±2) showed significantly increased expression of GzB, in comparison to the controls (**Figure 47** In agreement with the killing efficiency data (**Figure 46**), CAR4 cells expressed lower

amounts of GzB in comparison to CAR8 cells, suggesting that the origin of the differing kinetic efficiencies of these cells might be the differences in GzB content (**Figure 47**).

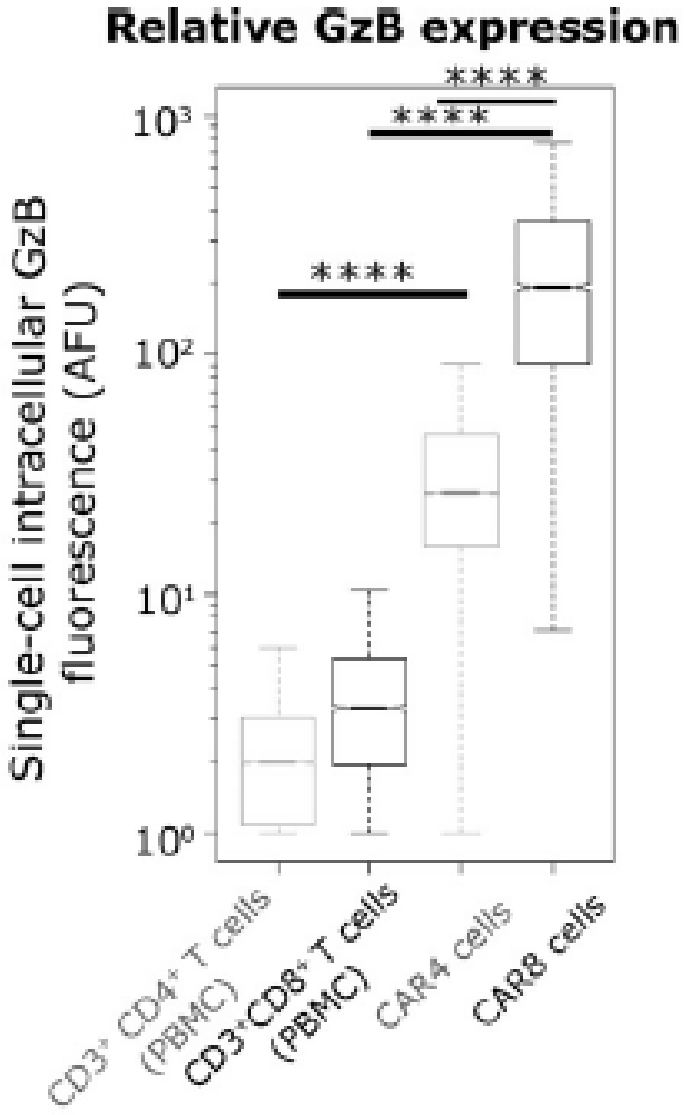

Figure 47: Box and whisker plots (extremities indicate 99% confidence intervals) displaying intracellular expression of Granzyme B identified by immunofluorescent staining and flow-cytometry.

In order to quantify the contribution GzB secretion to tumor cell killing at the single cell level, the ability of CAR4 cells to kill tumor cells in the presence of the calcium chelator EGTA was studied using flow cytometry (88). EGTA blocks cytotoxic granule exocytosis, and hence should eliminate GzB mediated killing. Not surprisingly, CAR4 cells co-cultured with tumor cells in the presence of 5 mM EGTA, demonstrated a substantial reduction in tumor cell killing across three different cell lines, Daudi-β2m, NALM-6 and CD19^{+}EL4 (**Figure 48**). The most striking reduction was seen with Daubi-β2m tumor cells, wherein CAR4 cell mediated killing was completely abolished (**Figure 48**).

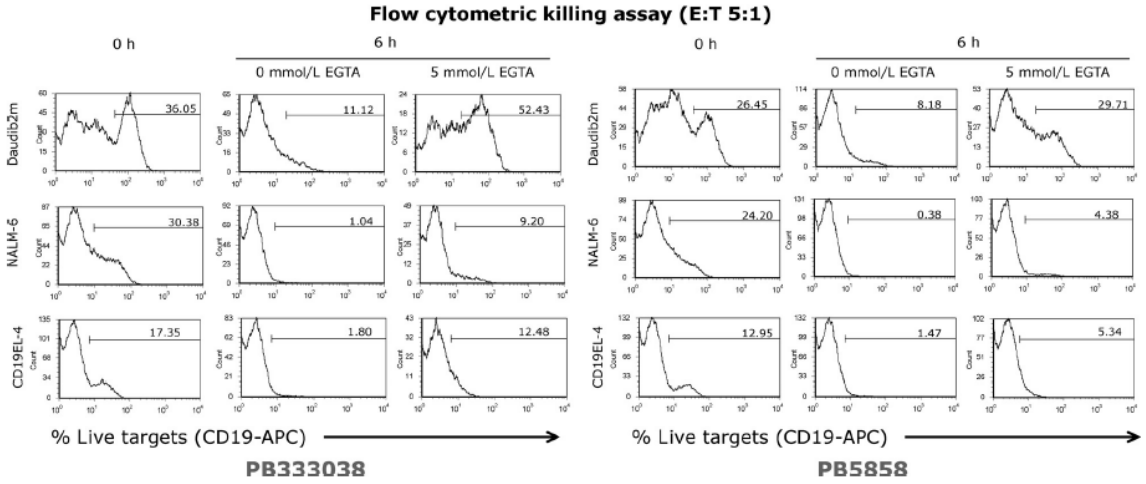

Figure 48: Flow cytometric killing assay (E:T = 5:1) of CAR4 cells incubated with three separate target cell lines (Daudi-β2m, NALM-6 and CD19^{+}EL4) in the absence or presence of 5mM EGTA blockade.

2.3.8. CAR^{+} T-cell fate is dependent on tumor-cell density.

AICD is a mechanism by which T cells undergo programmed apoptosis in response to functional activation (89). The frequency and kinetics of individual cytolytic CAR^{+} T cells to undergo AICD was monitored under the two conditions: at high and low tumor densities. CAR8 cells inducing apoptosis of single targets demonstrated significantly faster

kinetics of AICD (t_{AICD} 221±14 minutes) in comparison to the multi-killer CAR8 cells from the same donors (t_{AICD} 371±29 minutes, **Figure 49**).

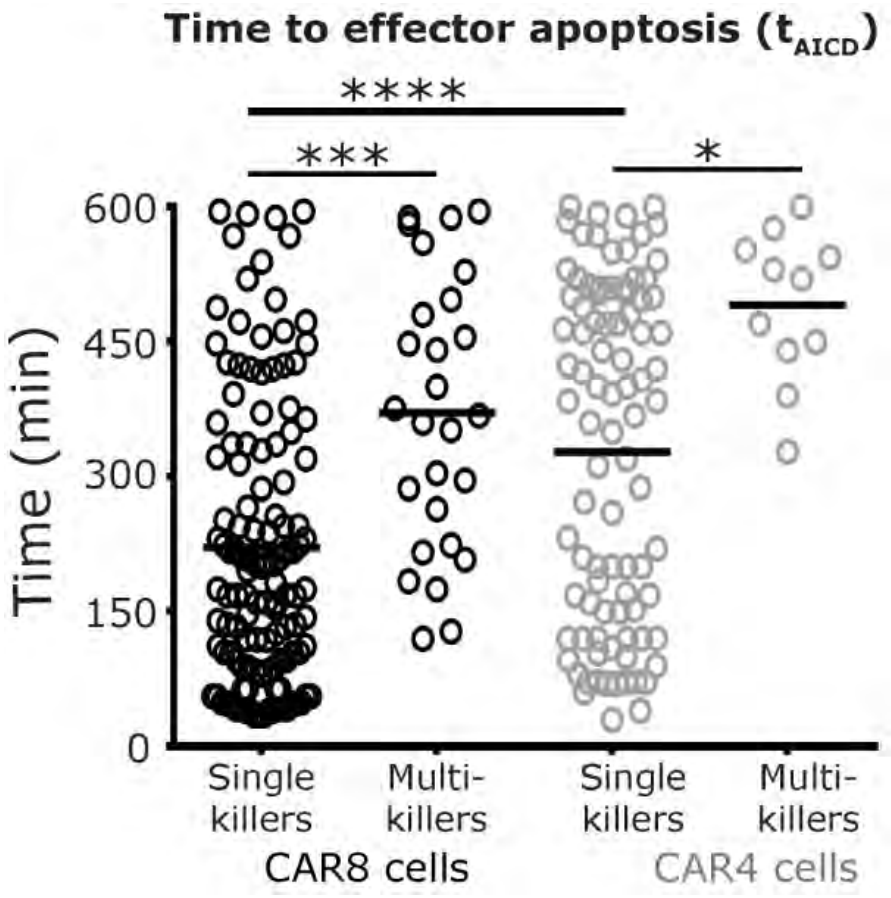

Figure 49: Comparisons of the mean kinetics of effector apoptosis of individual single killer CAR$^+$ T cells (E:T 1:1) with multi-killer CAR$^+$ T cells (E:T 1:2-5). Each circle represents a single-cell

This trend of faster AICD kinetics at lower tumor cell density was also observed with CAR4 cells, although with delayed kinetics (**Figure 49**). Direct comparisons of the cells of different phenotypes at the same tumor cell density indicated that single-killer CAR8 cells underwent faster AICD (t_{AICD}, 221±14 minutes) in comparison to CAR4 cells (t_{AICD} 328±19 minutes) (**Figure 49**). Consistent with the expectation that multi-killers efficiently resist AICD, these T cells from three of four donors displayed low frequencies of cells undergoing AICD (13-25%, **Figure 50**).

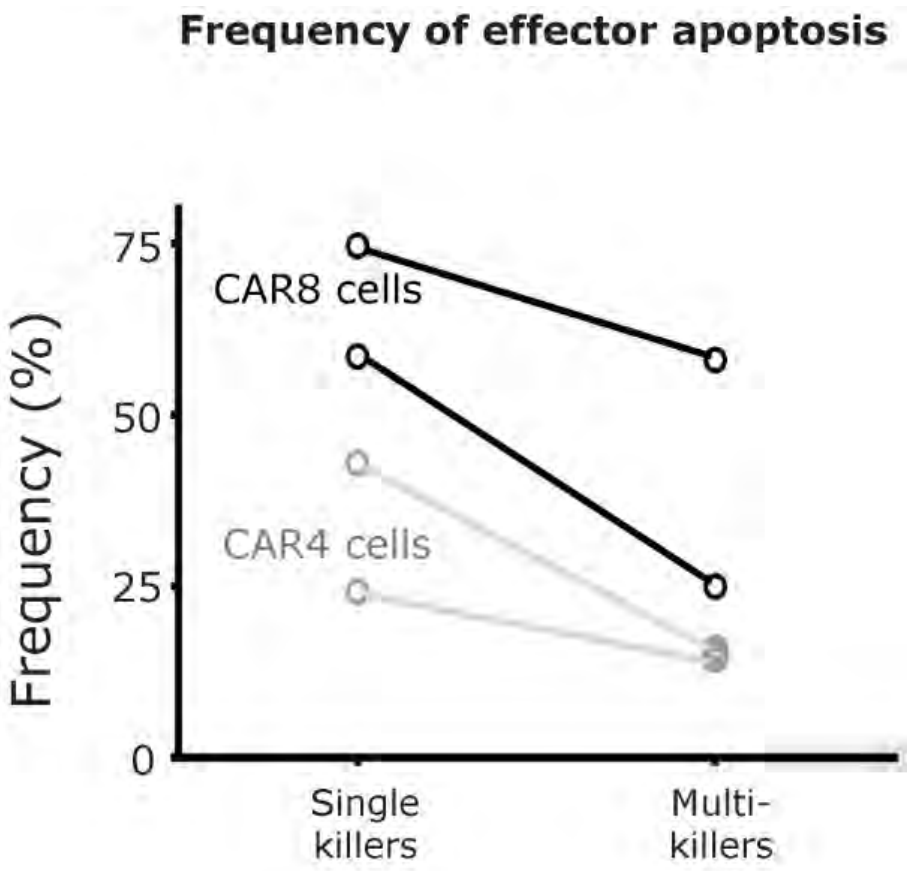

Figure 50: Frequency of killer-cell apoptosis as a function of tumor cell density.

However, multi-killer T cells from the last donor displayed AICD at elevated frequencies (58%) underscoring that the efficiency of multi-killers to execute multiple tumor cells must be evaluated in the context of their ability to resist AICD (**Figure 50**). We confirmed that the effector apoptosis that was observed required functional antigenic stimulation by co-incubating CAR8 cells with $CD19^{-}$EL4 cells within nanowell grids and imaged them using TIMING. The frequency of apoptotic effectors under these conditions was only 4% and this also confirmed that phototoxicity was negligible under the current imaging conditions.

Significantly, across all four donors, the frequencies of cytolytic CAR^+ T cells undergoing AICD was higher at an E:T of 1:1 in comparison to the multi-killer CAR^+ T cells, and this effect was more exaggerated with CAR8 cells (**Figure 50**). These data may help account for the decrease in number and even disappearance of infused CAR^+ T cells when the $CD19^+$ tumor mass is reduced.

2.4. DISCUSSION

We implemented a high-throughput single-cell assay (TIMING) to dynamically profile the functionality of CAR^+ T cells. Our analyses at the single-cell level demonstrate that much like CAR8 cells, CAR4 cells can directly engage in tumor cell killing, albeit with altered kinetics. We further demonstrate that CAR4 cells can participate in multi-killing via simultaneous conjugation to multiple tumor cells.

At low tumor cell densities (E:T 1:1), the majority of the single killer CAR8 cells were significantly faster in killing tumor cells in comparison to individual CAR4 cells (**Figure 41**). By contrast, both single killer CAR8 and CAR4 cells within the S1 subgroup, characterized by their high basal motility, displayed no significant differences in the kinetics of tumor cell killing. Furthermore, in contrast to the rest of the population, effector apoptosis was infrequent amongst CAR8 and CAR4 cells in the S1 subgroup. Collectively, these data suggested that the high basal motility of CAR^+ T cells (CAR4 or CAR8) might help identify efficient killers with decreased propensity for AICD.

When interacting with increased numbers of tumor cells (E:T ratios of 1:2 to 1:5), both individual CAR4 and CAR8 cells efficiently conjugated to multiple tumor cells, facilitating multiplexed killing. Comparisons amongst the different tumor cells killed by these individual multi-killer CAR4/CAR8 cells demonstrated that they displayed an essentially

unchanged efficiency ($t_{Contact}$) of killing of not only the first and second target killed, but also in comparison to (single-killer) CAR^+ T cells that were incubated with only one tumor cell (**Figure 51**).

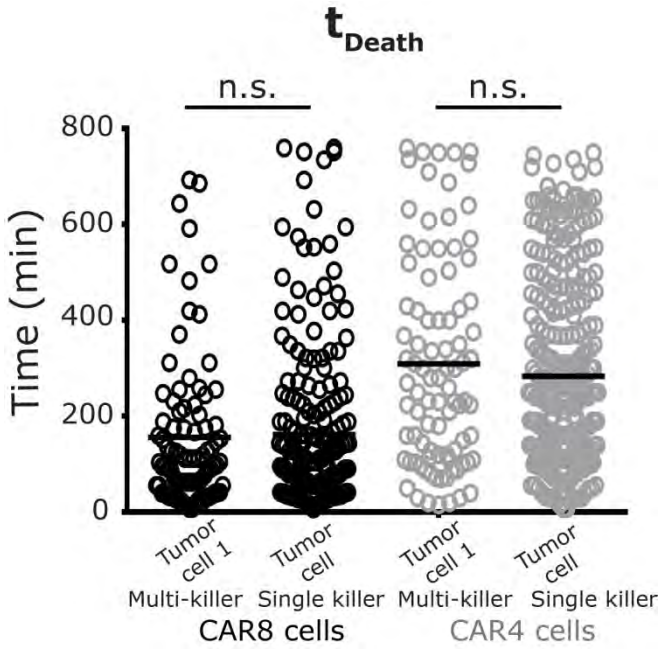

Figure 51: Comparison of the killing efficiency of individual single killer CAR^+ T cells (E:T 1:1) with multi-killer CAR^+ T cells (E:T 1:2-5) that killed multiple NALM-6 tumor cells.

In comparing CAR4 cells with CAR8 cells however, consistent with the observations at an E:T ratio of 1:1 , CAR4 cells were significantly slower in tumor cell killing. Intracellular staining at the single-cell level indicated that the molecular origin of the differences in kinetic efficiency of the CAR4 and CAR8 cells could be attributed to their GzB content and this was further confirmed by blocking granule exocytosis using EGTA (**Figure 47-48**).

For both CAR4 and CAR8 cells, single killer effectors underwent apoptosis at higher frequencies and with faster kinetics in comparison to multi-killer CAR^+ T cells. These data indicate that activation for lysis through multiple targets as opposed to

prolonged conjugation with a single target reduces the propensity for effector apoptosis. Although the mechanistic basis for the responsiveness of these T cells to antigen/target density is not known, it is conceivable that the continuous propagation of these cells on irradiated aAPC at defined ratios, allows for balanced activation while minimizing AICD (90). Collectively, these data could provide mechanistic insights into observations that infused CAR^+ T cells swell in number in response to addressing large numbers of $CD19^+$ tumor cells, but then decline in number as the tumor bioburden is lowered due to the multi-killing by effector T cells (63, 91).

In aggregate, comparisons of the CAR4 cells and CAR8 cells demonstrate that while CAR4 cells can participate in killing and multi-killing, they do so at slower rates, likely due to the lower GzB content. This decreased kinetic efficiency however is likely a minor disadvantage and is counter balanced by their decreased propensity of these cells to undergo AICD in the absence of help from other cells, as profiled in our nanowell system. Indeed, recent preclinical and clinical data have suggested that complete eradication of established tumors can be accomplished by the adoptive transfer of T cells derived exclusively from $CD4^+$ T cells (73-75). Similarly, adoptive transfer of human T helper 17 (T_H17) cells has shown preclinical promise for the treatment of ovarian cancer (92, 93). Although we have focused on the heterogeneity amongst CAR^+ T cells, the results presented here are also likely influenced by the underlying heterogeneity in tumor cells. While the expression of CD19 is uniform on the cells used as targets in our assays (**Figure 7**), it is feasible that there could be subpopulations of tumor cells that are resistant to CAR^+ T-cell mediated killing.

Data from clinical trials have also shown a correlation between *in vivo* persistence of infused CAR^+ T cells and patient outcomes (94). Significantly, the findings of our short-term TIMING data (12h monitoring) that describes motility and ability to resist AICD as important attributes of functional T cells, is consistent with persistence data obtained in mouse models infusing CD19-specific CAR^+ T cells that suggest that these same features are essential for tumor regression (95). Motility is likely a key parameter of the efficacy of T-cell therapies and has a significant role in tumor regression. It has been previously demonstrated that cancer cells from B-cell malignancies effectively dampen anti-tumor responses via disruption of actin-based basal T-cell motility *in vitro* (96-98). Second, the negative costimulatory molecules, PD1 and CTLA4 have opposing effects on T-cell motility both *in vitro* and *in vivo* (99, 100). Finally, recent intravital microscopy data from melanoma models in mice have demonstrated that successful therapeutic anti-CTLA4 treatment correlates with greater T-cell motility (101).

The variation in the composition of CAR^+ T cells within a population of effector cells between donors across samples highlights the challenges in eliciting functional responsiveness in heterogeneous samples. As the field of adoptive immunotherapy takes on the challenge of targeting diseases that vary in burden, biodistribution, and antigen expression and density, it is important that *a priori* definitions of single-cell potency (proliferation, killing, cytokine secretion etc.) be available. We suggest that identifying/quantifying specific biomarkers of efficacy, as described herein, may enable the manufacture of next-generation CAR^+ T cells.

CHAPTER 3

Integrated single-cell functional and molecular profiling of dynamic T cell behavior

Note: this is a reformatted manuscript in preparation for submission to Cancer Research.

3.1. INTRODUCTION

Integrative quantification of single-cell dynamic functional behavior and the underlying mechanisms responsible for the functions is essential to developing a comprehensive understanding of cellular behaviors. Quantifying the heterogeneity at the single-cell level in high-throughput across multiple biological dimensions from the genome and transcriptome, to intracellular and extracellular signaling, and to interaction with other kinds of cells can have a direct impact on improving therapeutic discovery in biotechnology, diagnosis of diseases, and in facilitating immunotherapy (28). While flow cytometry is an excellent tool for providing snapshots of the cellular phenotype, it is not well suited for studying continuous dynamic cellular behaviors. To characterize the complete identity of individual single cells, it is desirable to have a modular method that can quantify and screen for cellular functionality such as motility, interaction with other cells, and protein secretion; and the ability to integrate these parameters with single-cell multiplexed molecular platforms.

T cells are an essential component of the adaptive immune response against pathogens and tumors. A critical hallmark of a robust adaptive immune response against pathogens and tumors is the ability of individual T cells to participate in multiple functions (polyfunctionality) (1, 102). T cells play an important role in mediating anti-tumor

immunity and the presence of tumor infiltrating lymphocytes (TILs, check abbreviations and definitions section) is a positive clinical prognostic marker for certain tumors (103). Among the most well described functional attributes of T-cell anti-tumor efficacy are motility (tumor-trafficking and infiltration) (27), direct cytotoxicity (release of cytotoxic molecules) (23, 24) and secretion of the pro-inflammatory cytokines like IFN-γ (25, 26). Unlike cytotoxicity that only influences the target cell that is directly conjugated to the T cell, secretion of IFN-γ has a more profound influence on all cells within the microenvironment by multiple mechanisms including elevated expression of HLA-class I molecules (104), induction of chemokines that promote immune cell infiltration (105), mediation of angiostasis (106), and prevention of the outgrowth of antigen-loss variants (107). In addition, secretion of IFN-γ can also induce adaptive resistance mechanisms in tumors by inducing the expression of T-cell suppressive molecules and down-modulation of tumor antigen expression (108).

Direct measurement of all these T cell functions at the single-cell level requires the simultaneous monitoring of multiple parameters including cell-cell interactions, cell migration, gene expression, the ability to detect secreted proteins, and the survival of the effector cells. These challenges have been tackled by measuring just a subset of these effector functions and relying on correlative studies to establish a link to cellular functionality. Indeed, while multiphoton microscopy is a useful for studying T-cell motility and cytotoxicity *in situ* or *in vivo* (109-111), the number of T cells that can be simultaneously tracked is small and limited to the field-of-view, potentially leading to sampling bias. *In vitro* dynamic imaging systems (56, 78, 112, 113) may be better suited for studying the longitudinal interactions between T cells and target cells at single-cell

resolution, in a defined environment and high-throughput. Microfabricated nanowell arrays are ideal for tracking both the motility and interaction between cells (56, 78, 112). While elegant methods like microengraving (31, 32) and the single-cell barcode chip (SCBC) (33), have been reported for the analysis of cytokines secreted by single cells, these require capture of the secreted cytokine on a separate glass substrate via encapsulation. Significantly, there are as yet no reports documenting the simultaneous measurement of motility, T-cell target-cell interaction parameters including the kinetics of killing, and cytokine secretion quantified within the same timeframe.

Here, we have developed and validated an integrated methodology that combines microbead-based molecular sensors for detecting cytokine secretion from single T cells concurrently with Timelapse Imaging In Nanowell Grids (TIMING) to monitor T-cell motility and cytotoxicity, without the need for encapsulation (31, 33). We demonstrate that TIMING can be used to combine functional and molecular screening at the single-cell level, by performing multiplexed transcriptional profiling (96 genes) on CD19-specific CAR^+ T cells. Simultaneous quantification of the interaction between individual tumor-specific $CD8^+$ T cells and multiple target cells demonstrated that IFN-γ was the most common function elicited. However, $CD8^+$ T cells with killing ability, especially serial killing ability, required shorter durations of target cell conjugation in comparison to IFN-γ secreting mono-functional cells, indicating rapid synapse termination by T cells capable of killing versus cytokine secretion. The behavioral interaction of polyfunctional T cells exhibiting both killing and IFN-γ secretion was similar to that of serial killers without IFN-γ secretion, suggesting that killing was the dominant determinant of the interaction behavior. Tracking the velocities of these cells by longitudinal time-lapse imaging revealed

that these serial killer T cells (with or without IFN-γ secretion) may be identified based on their higher out-of-contact basal motility. Single-cell multiplexed transcriptional profiling of T cells identified only by their basal motility, confirmed that the motile cells expressed an activated phenotype with significantly increased amounts of perforin and other genes associated with chemotaxis. We propose an integrated model of functional $CD8^+$ T-cell behavior based on these results.

3.2. Methods

3.2.1. Human Subjects Statement. All work outlined in this report was performed according to protocols approved by the Institutional Review Boards at the University of Houston and the University of Texas M.D. Anderson Cancer Center.

3.2.2. Cell lines, primary T cells, TILs, and reagents. Human pre-B cell line NALM-6 (ATCC) and CAR^+ T cells were cultured as described previously (81). The cell lines were routinely tested to ensure that they were free of mycoplasma contamination and flow-cytometry was utilized to confirm the expression of CD19. TILs were isolated and expanded as previously described. Briefly, initial TIL expansion was performed in 24-well plates from either small 3-5 mm^2 tumor fragments or from enzymatic digestion, followed by centrifugation with FICOLL. TILs were then allowed to propagate for 3-5 weeks in TIL-complete media containing 6000 IU/mL human recombinant IL-2 (Prometheus). Once desired number of TIL was achieved, Rapid Expansion Protocol (REP) was performed in which TIL was cultured together with PBMC feeder cells (1 TIL: 200 feeders) preloaded with anti-CD3 (OKT3, eBioscience) in a G-REX 100M flask until the desired number of cells were achieved and harvested. **Table 3** provides a complete listing of reagents used in this study.

Table 3: List of important reagents described in this manuscript

Reagents	Manufacturer	Reference
ProMag™ 3 Series • Goat anti-Mouse IgG (Fc) beads (PMM3N)	Bangs Laboratories, Inc.	http://www.bangslabs.com/sites/default/files/imce/docs/PDS%20723%20Web.pdf
PKH26 Red Fluorescence Cell Linker Kits	Sigma-Aldrich	https://www.sigmaaldrich.com/content/dam/sigma-aldrich/docs/Sigma/Bulletin/mini26bul.pdf
PKH67 Green Fluorescence Cell Linker Kits	Sigma-Aldrich	http://www.sigmaaldrich.com/content/dam/sigma-aldrich/docs/Sigma/Bulletin/midi67bul.pdf
Annexin V-Alexa Fluor 647 (A23204)	Life Technologies	https://tools.lifetechnologies.com/content/sfs/manuals/mp13199.pdf
Mouse anti-human IFNγ mAb 1-D1K (3420-3-250)	Mabtech	https://www.mabtech.com/sites/default/files/datasheets/3420-3-250.pdf
Mouse anti-human IFNγ mAB 7-B6-1 biotinylated (3420-6-250)	Mabtech	https://www.mabtech.com/sites/default/files/datasheets/3420-6-250.pdf
R-Phycoerythrin Streptavidin (Strep –PE) (016-110-084)	Jackson ImmunoResearch Laboratories, Inc.	https://www.jacksonimmuno.com/catalog/products/016-110-084
DNA Suspension Buffer, (10mM Tris, 0.1mM EDTA, pH 8.0)	Teknova	http://www.teknova.com/DNA-SUSPENSION-BUFFER-p/t0221.htm
CellsDirect™ One-Step qRT-PCR Kit	Life Technologies	https://www.lifetechnologies.com/order/catalog/product/11753100
Exonuclease I (E. coli)	New England Biolabs	https://www.neb.com/products/m0293-exonuclease-i-e-coli
TE Buffer 10mM Tris, 1mM EDTA	Teknova	http://www.teknova.com/TE-BUFFER-p/t0224.htm
SsoFast EvaGreen Supermix with Low ROX	Bio-Rad	http://www.bio-rad.com/en-us/sku/172-5211-ssofast-evagreen-supermix-with-low-rox
SUPERase In RNase Inhibitor (20 U/µL)	Life Technologies	https://www.lifetechnologies.com/order/catalog/product/AM2694
96.96 Dynamic Array Chip for Gene Expression	Fluidigm	https://www.fluidigm.com/ifcs

3.2.3. Beads preparation: coating beads with primary capture antibody. 1 µL of Promag 3 Series goat anti-mouse IgG-Fc beads (~2.3 x 10^5 beads) in solution was washed with 10 µL of PBS, and re-suspended in 19.6 µL PBS (~0.05% solids). Mouse anti-human IFN-γ (clone 1D1K) was then added to beads at final concentration of 10 µg/mL and incubated for 30 min at room temperature (RT), followed by washing and re-suspension in 100 µL PBS.

3.2.4. ELISpot assays. ELISpot assay was performed with fresh PBMC and TIL as previously described (31). Briefly, microwell plates were coated with capture antibody anti-human IFNγ-1D1K at 10 µg/mL overnight at 4 °C. The next day, the plates were washed twice in PBS and blocked with RPMI-PLGH +10% FBS for 45 min at 37 °C. Cells were prepared, as follows, in triplicates: (1) 4,000 PBMC stimulated with 10 ng/mL PMA/1 µg/mL ionomycin per well (2) 4,000 melanoma-specific TIL stimulated with 10 ng/mL PMA/1 µg/mL ionomycin per well (3) 200,000 PBMC stimulated with 2 µg/mL CEF peptide (4) Corresponding non-stimulated cells. Next, cells were incubated for 18 hr at 37 °C/5% CO_2, followed by five washes with PBS and 2 hr incubation with biotinylated detection anti-human IFNγ 7-B61 at 37 °C/5% CO_2 in PBS +0.5% FBS. After washing with PBS seven times, the immunosandwich was completed with subsequent addition of extravidin-alkaline phosphatase (1hr incubation at 37 °C/5% CO_2 [Sigma-Aldrich]). The plate was washed five times with PBS, and BCIP/NBT (Sigma-Aldrich) substrate was added and incubated for 15 min at 37 °C/5% CO_2. The plate was subsequently read with ELISpot reader (C.T.L. counter) while taking into account background measurement.

3.2.5. Nanowell array fabrication and cell preparation. Nanowell array fabrication for interrogation of effector functions at single-cell level was performed as described

previously (78). Approximately 1 million effector cells and target cells were both spun down at 400 xg for 5 min followed by labeling with 1 μM PKH67 and PKH26 fluorescent dyes respectively according to manufacturer's protocol. Excess unbound dyes were then washed away and cells were re-suspended at ~2 million cells/mL concentration in complete cell-culture media (RPMI + 10% FBS).

3.2.6. Finite element simulations. The system of partial differential equations to model variation of analyte concentrations, C and C_s, with time, was solved using Transport of diluted species interface, Chemical reaction engineering module in COMSOL Multiphysics 4.1. Mass balance equation involving Cs was solved using its weak form. Change in positions of cell and bead, convective transport, diffusion on the bead surface ($D_s = 10^{-25}$ m^2/s), non-specific adsorption on walls and degradation of analyte were neglected to simplify numerical simulations.

3.2.7. TIMING assays for multiplex study of effector cytolytic phenotypes and IFN-γ secretion. Capture antibody coated beads and labeled effector and target cells were loaded consecutively onto nanowell arrays. Whenever necessary, arrays were washed with 500 μL of cell culture media to remove excess beads or cells. Next, detection solution containing Annexin V - Alexa Fluor 647 (AF647) (Life Technologies) (for detection of target apoptosis) were prepared by adding 50 μL solutions from stock to 2.5 mL of complete cell-culture media without phenol red. Nanowell arrays were then imaged for 5 hr at interval of 5 minutes using LEICA/ZEN fluorescent microscope utilizing a 20x 0.45 NA objectives and a scientific CMOS camera (Orca Flash 4.0). Subsequently, mouse anti-human IFN-γ biotin was added to 2.5 mL cell media above at 1:1000 dilution. This was incubated for 30 minutes followed by washing and incubation with 5 μg/mL Streptavidin - R-Phycoerythrin

(PE). The entire chip was again imaged to determine the intensity of PE signal on the microbeads and the two datasets were matched using custom informatics algorithms.

3.2.8. Image processing, cell segmentation and tracking, and data analytics. Image analysis and cell segmentation/tracking were performed as described previously (113). The pipeline of image processing and cell segmentation ends with statistical data analysis based on the tabular spatio-temporal measurement data generated by the automated segmentation and cell tracking algorithms. Nanowells containing 1 effector and 2-5 tumor cells were selected for further analysis. We then partitioned all these events based on the functionalities of the cells i.e., mono-kill, serial kill, and IFNγ secretions. A size-exclusion filter based on maximum pixel areas were used to effectively differentiate cells from beads.

3.2.9. Gene expression profiling. PKH green stained $CD8^+$ T cells were loaded on a nanowell array, immersed with Annexin-AF647 (Life Technologies) containing phenol red free complete cell-culture medium and imaged for 3 hours using TIMING exactly as described above. After carefully washing the cells on the chip 3 times with cold PBS (4°C), cells were kept at 4°C until retrieval. Time-lapse sequences were manually analyzed to identify live high and low motility cells. The cells were individually collected using an automated micro-manipulating system (CellCelector, ALS) and deposited in nuclease free microtubes containing 5 µL of 2x CellsDirect buffer and RNAse Inhibitor (Invitrogen). Single cell RT-qPCR was then performed using the protocol ADP41 developed by Fluidigm. Ninety-two cells (48 motile and 44 non motile) were assayed, along with bulk samples of 10 and 100 cells, and with no-cell and no-RT controls. The panel of 95 genes **(Table 4)** included genes relevant to T cell activation, signaling and gene regulation, and was designed and manufactured by Fluidigm D3 AssayDesign.

Table 4: List of targeted genes and primer design for DELTAgene qPCR assays

Target	FP	RP	Gene Full Name
ALDOA	CCATGGCGACCGTCACA	TCACTCTGGCCTCCAGACA	aldolase A, fructose-bisphosphate
B2M	TCCGTGGCCTTAGCTGTG	CCCAGACACATAGCAATTCAGG	beta-2-microglobulin
BCL2	GACAGAGGATCATGCTGTACTT	CTTGGCATGAGATGCAGGA	B-cell CLL/lymphoma 2
BCL6B	AACCCCTCAGAGCACACAA	CGGCCCCGGAAAATTGAATA	B-cell CLL/lymphoma 6, member B
BTLA	TCCCATATCTGGACATCTGGAAC	CTCCTGCTAAGATGGAGTGTTCA	B and T lymphocyte associated
CCL3	CCGTCACCTGCTCAGAATCA	CCATGGTGCAGAGGAGGAC	chemokine (C-C motif) ligand 3
CCL4	CGTGACTGTCCTGTCTCTCC	TCTACCACAAAGTTGCGAGGAA	chemokine (C-C motif) ligand 4
CCR1	AACCCAGAAAGCCCCAGAAA	GTGGTGTTTGGAGTTTCCATCC	chemokine (C-C motif) receptor 1
CCR2	ACATACCAGGACTGCCTGAG	GTGGATGTACTGGGGAAATGC	chemokine (C-C motif) receptor 2
CCR4	CATTGCCTCACAGACCTTCC	AGGGTGGTGTCTGCTATATCC	chemokine (C-C motif) receptor 4
CCR5	TGAGACATCCGTTCCCCTACA	TGGCAGGGCTCCGATGTATA	chemokine (C-C motif) receptor 5
CCR6	AGGCAGCGATGTCTGTGAA	AGCTCAAGCCCCAACATCA	chemokine (C-C motif) receptor 6
CCR7	GTGGTGGCTCTCCTTGTCA	TGTGGTGTTGTCTCCGATGTA	chemokine (C-C motif) receptor 7
CD160	AGAAGCCAGAAGTCAGGTATCC	TCCCGTCACTGTGTAGTTCC	CD160 molecule
FAS	AGAAGGGAAGGAGTACACAGAC	CCGGGTGCAGTTTATTTCCA	Fas (TNF receptor superfamily, member 6)
CD2	AGTGCACAGCAGGGAACAA	AGGCTGCCTCCTCCACATA	CD2 molecule
CD244	AACCACAGCCCTTCCTTCAA	GAGCAGGGTTCTGGGCTTTA	CD244 molecule, natural killer cell receptor 2B4
CD27	CACTACTGGGCTCAGGGAAA	TGCTGGTCACAGTCCTTCA	CD27 molecule
CD28	GTCCTGGCTTGCTATAGCTT	CATGTAGTCACTGTGCAGGA	CD28 molecule
CD3D	CGTTTCTCTCTGGCCTGGTA	CTCTACCCATGTGATGCTGGTA	CD3d molecule, delta (CD3-TCR complex)
CD3E	GCTACCCCAGAGGAAGCAAA	TCCATCTCCATGCAGTTCTCAC	CD3e molecule, epsilon (CD3-TCR complex)
CD4	AAAGTTGCATCAGGAAGTGAACC	CCCACACCTCACAGGTCAAA	CD4 molecule
CD40LG	GAGGCCAGCAGTAAAACAAC	AGTTGTTGCTCATGGTGTAGTA	CD40 ligand

Table 4 (continued)

Target	FP	RP	Gene Full Name
CD44	CCGGACACCATGGACAAGTT	CCTGCAAAGCGGCAGGT	CD44 molecule (Indian blood group)
CD58	AATCATTTTGACAACCTGTATCCC	TGTAATTACTGCTAATGGTATGGGTA	CD58 molecule
CD63	GCAGCCAGCCTTGGGAA	GCAAGAACTTCACACATTTCATTCC	CD63 molecule
CD69	TCACCCATGGAAGTGGTCAA	ACACACTTGTCAGACCCTGTA	CD69 molecule
CD80	TGCTGGCTGGTCTTTCTCA	GAGTTTGTGCCAGCTCTTCAA	CD80 molecule
CD86	CGGCCTCGCAACTCTTATA	TGGTCTGTTCACTCTCTTCC	CD86 molecule
CD8A	ACTTCGTGCCGGTCTTCCT	GCTGCGACGCGATGGT	CD8a molecule
CSF2	TGATGGCCAGCCACTACAA	CAAAGGGGATGACAAGCAGAAA	colony stimulating factor 2 (granulocyte-macrophage)
CTLA4	CTTGGATTTCAGCGGCACAA	GCTGCTGGCCAGTACCA	cytotoxic T-lymphocyte-associated protein 4
CX3CL1	CCACCTTCTGCCATCTGAC	CGTGATGTTGCATTTCGTCAC	chemokine (C-X3-C motif) ligand 1
CX3CR1	GTAGTGTTTGCCCTCACCAAC	ATCAGACAAGGCCAGGTTCA	chemokine (C-X3-C motif) receptor 1
CXCL10	GCTGTACCTGCATCAGCATTA	CTGGATTCAGACATCTCTTCTCAC	chemokine (C-X-C motif) ligand 10
CXCL12	AGCCAACGTCAAGCATCTCA	GCTTCGGGTCAATGCACAC	chemokine (C-X-C motif) ligand 12
CXCL9	AGCCCTTCCTGCGAGAAAA	ATCTGCTGAATCTGGGTTTAGACA	chemokine (C-X-C motif) ligand 9
IL8RA	ATCTCTGACTGCAGCTCCTA	TGTCCTCTTCAGTTTCAGCAA	chemokine (C-X-C motif) receptor 1
CXCR3	AACTGTGGCCGAGAAAGCA	TTGAGGCAGCAGTGCATGTA	chemokine (C-X-C motif) receptor 3
CXCR4	ATCTTCCTGCCCACCATCTAC	CCCATGACCAGGATGACCAA	chemokine (C-X-C motif) receptor 4
FASLG	TGGGGATGTTTCAGCTCTTCC	CTGTGTGCATCTGGCTGGTA	Fas ligand (TNF superfamily, member 6)
FOXP3	TGTGGGGTAGCCATGGAAA	GGGTCGCATGTTGTGGAA	forkhead box P3
G6PD	GCCGTCACCAAGAACATTCA	CTCCCGAAGGGCTTCTCC	glucose-6-phosphate dehydrogenase
GAPDH	ACACCATGGGGAAGGTGAAG	GTGACCAGGCGCCCAATA	glyceraldehyde-3-phosphate dehydrogenase
GATA3	CACGGTGCAGAGGTACCC	AGGGTAGGGATCCATGAAGCA	GATA binding protein 3
GZMA	GAAGCCTCCGAGGTGGAA	GAAAACACCCTCGCACAACA	granzyme A (granzyme 1, cytotoxic T-lymphocyte-associated serine esterase 3)

Table 4 (continued)

Target	FP	RP	Gene Full Name
GZMB	CCCCATCCAGCCTATAATCCTAA	CTGGGCCTTGTTGCTAGGTA	granzyme B (granzyme 2, cytotoxic T-lymphocyte-associated serine esterase 1)
GZMK	ATCCACAGTGGGTGCTGAC	AGAGTGTGCGCCTAAAACCA	granzyme K (granzyme 3; tryptase II)
HAVCR2	GGATCCAAATCCCAGGCATAA	CTTGGAAAGGCTGCAGTGAA	hepatitis A virus cellular receptor 2
ICOS	AGTCTGCATTTTGGGATGCA	GTCGTGCACACTGGATGAA	inducible T-cell co-stimulator
ICOSLG	TTGGCTGCTGCATAGAGAAC	CTTGTCTCTCTCTCCGATGTCA	inducible T-cell co-stimulator ligand
IFNG	ACTGCCAGGACCCATATGTAA	GTTCCATTATCCGCTACATCTGAA	interferon, gamma
IFNGR1	AAGCCAGGGTTGGACAAAA	GATATCCAGTTTAGGTGGTCCAA	interferon gamma receptor 1
IL10	CCGTGGAGCAGGTGAAGAA	GTCAAACTCACTCATGGCTTTGTA	interleukin 10
IL12A	CACAGTGGAGGCCTGTTTA	TCTGGAATTTAGGCAACTCTCA	interleukin 12A (natural killer cell stimulatory factor 1, cytotoxic lymphocyte maturation factor 1, p35)
IL12B	TCCCTGACATTCTGCGTTCA	GGTCTTGTCCGTGAAGACTCTA	interleukin 12B (natural killer cell stimulatory factor 2, cytotoxic lymphocyte maturation factor 2, p40)
IL12RB1	GCCATATCCGGATGCAGAC	CAGCTGTGGGACCCTCATA	interleukin 12 receptor, beta 1
IL12RB2	GTCTTGGAAGCTCCTCTTCAC	TCTAATGTCCCACGGAGGAA	interleukin 12 receptor, beta 2
IL13	TGCAGTGCCATCGAGAAGAC	TCGGACATGCAAGCTGGAAA	interleukin 13
IL15	AGCCAACTGGGTGAATGTAA	CACTTTCCGTATATAAAGTAGCATCA	interleukin 15
IL15RA	TGAGCGCTGTGTCTCTCC	CCTCCATGGCTTCCATTTCAAC	interleukin 15 receptor, alpha
IL17A	ACTACAACCGATCCACCTCAC	ACTTTGCCTCCCAGATCACA	interleukin 17A
EOMES	CTGTGGCAAAGCCGACAATA	CTCATCCAGTGGGAACCAGTA	eomesodermin
IL17RA	CCAAACCACCAGTCCAAGAA	CTCATGCATGGCGTGGTTA	interleukin 17 receptor A
IL18	GACCAAGGAAATCGGCCTCTA	TCACAGAGATAGTTACAGCCATACC	interleukin 18 (interferon-gamma-inducing factor)
IL18R1	GGTTCTTCTTGGACCAAAGCTTAA	AGCAGAGCAGTTGAGCCTTA	interleukin 18 receptor 1
IL2	CCCAGGGACTTAATCAGCAATA	TTCTACAATGGTTGCTGTCTCA	interleukin 2
IL21R	TGCATCCTGGAAATGTGGAAC	CCTCGTCCTTCAGCTCTTCATA	interleukin 21 receptor

Table 4 (continued)

Target	FP	RP	Gene Full Name
IL2RA	GCACAGGTGAAATGGAGACC	GACGAGGCAGGAAGTCTCA	interleukin 2 receptor, alpha
IL2RB	ATGGCCATCCAGGACTTCA	TTGCATCTGTGGGTCTCCA	interleukin 2 receptor, beta
IL2RG	GCCCAATGGGAATGAAGACA	TGGAAACACTGAGGGAGTCA	interleukin 2 receptor, gamma
IL4	CAGCTGATCCGATTCCTGAAA	GTTGGCTTCCTTCACAGGAC	interleukin 4
IL4R	GAGCTCCGCCTGTTGTACC	GCGCCTCCGTTGTTCTCA	interleukin 4 receptor
IL5	ACTCTGAGGATTCCTGTTCCTGTA	CCAGTGTGCCTATTCCCTGAAA	interleukin 5 (colony-stimulating factor, eosinophil)
IL7R	GGAGAAAGTGGCTATGCTCAA	CTGCGATCCATTCACTTCCA	interleukin 7 receptor
IRF4	CTACAACCGCGAGGAGGAC	TGTCGATGCCTTCTCGGAAC	interferon regulatory factor 4
KLF4	CTGCGGCAAAACCTACACAA	CGTCCCAGTCACAGTGGTAA	Kruppel-like factor 4 (gut)
KLRG1	ACCCAAGCCCAGAATGACTA	TTGCCACAAGGCAAGAACA	killer cell lectin-like receptor subfamily G, member 1
LAG3	TGGAGCCTTTGGCTTTCAC	GAGGGTGAATCCCTTGCTCTA	lymphocyte-activation gene 3
LEF1	AAGAAAGTGCAGCTATCAACCA	GCTGTCTTTCTTTCCGTGCTA	lymphoid enhancer-binding factor 1
NANOS2	TGTCCCATCCTGAGGCACTA	ACCGTTAAGCGGGCAGTAC	nanos homolog 2 (Drosophila)
NFKB1	CTGGAACCACGCCTCTAGATA	AAACTCTGGCTCATATGGTTTCC	nuclear factor of kappa light polypeptide gene enhancer in B-cells 1
PDCD1	GCAGCCTGGTGCTGCTA	GTGCGCCTGGCTCCTA	programmed cell death 1
PRF1	GTACAGCTTCAGCACTGACAC	CTGGGTGGAGGCGTTGAA	perforin 1 (pore forming protein)
RORA	CAGCAGATAACGTGGCAGAC	GGCACACAATTGCCACATCA	RAR-related orphan receptor A
RORC	CAAGACTCATCGCCAAAGCA	TTTCCACATGCTGGCTACAC	RAR-related orphan receptor C
STAT5A	CCCAGGCTCCCTATAACATGTA	ATGGTCTCATCCAGGTCGAA	signal transducer and activator of transcription 5A
STAT5B	AACAGAGGTTGGTCCGAGAA	GTTTCTGGGACATGGCATCA	signal transducer and activator of transcription 5B
TCF7	TTCAATCTGCTCATGCATTACCC	GTGGGCTGTTGAAATGTTCGTA	transcription factor 7 (T-cell specific, HMG-box)
TGFB1	CGTCTGCTGAGGCTCAAGTTA	TCGCCAGGAATTGTTGCTGTA	transforming growth factor, beta 1
TGFB2	CAAAAGCCAGAGTGCCTGAA	CGCTGGGTTGGAGATGTTAAA	transforming growth factor, beta 2
TGFBR1	GAAATTGCTCGACGATGTTCC	ACTGATGGGTCAGAAGGTACA	transforming growth factor, beta receptor 1

Table 4 (continued)

Target	FP	RP	Gene Full Name
TNFRSF9	GGGGCAGAAAGAAACTCCTGTA	TCTGGAAATCGGCAGCTACA	tumor necrosis factor receptor superfamily, member 9
TNFSF14	AGGTCTCACGAGGTCAACC	CCCAGCTGAGTCTCCCATAA	tumor necrosis factor (ligand) superfamily, member 14
ZAP70	AAGCGCGATAACCTCCTCATA	TTCCGTGTCTGCCTTCTCC	zeta-chain (TCR) associated protein kinase 70kDa

For data analysis, we first extracted Log2Ex value by subtracting Ct values from a threshold of 29, as described previously (114). We then excluded data from i) cells that had less than 40% of genes that were amplified and had a mean of Log2Ex out of the range of population mean±3SD and from ii) genes that were amplified in <10% of cells (115, 116). Post-process analysis was done using Excel (Microsoft), Prism (GraphPad), MeV (117), STrenD (https://github.com/YanXuHappygela/STrenD-release-1.0) and Genemania webtool (http://www.genemania.org/).

3.3. RESULTS

3.3.1. Design of an integrated platform for simultaneous profiling of protein secretion and dynamic cell-cell interactions.

We had previously reported on the ability to measure T-cell functions such as cytotoxicity at the single-cell level, but this was implemented as an end-point functional readout. We also quantified killing and cytokine secretion in different kinetic windows with no information on either intrinsic cellular behaviors like motility, or the nature of their interaction with target cells (50). Here, we sought to design an integrated method that had the ability to add/remove independent modules in determining the polyfunctional nature of the T cells: cytokine secretion, dynamics of interaction with target cells, cytotoxicity, and molecular profiling (**Figure 52**).

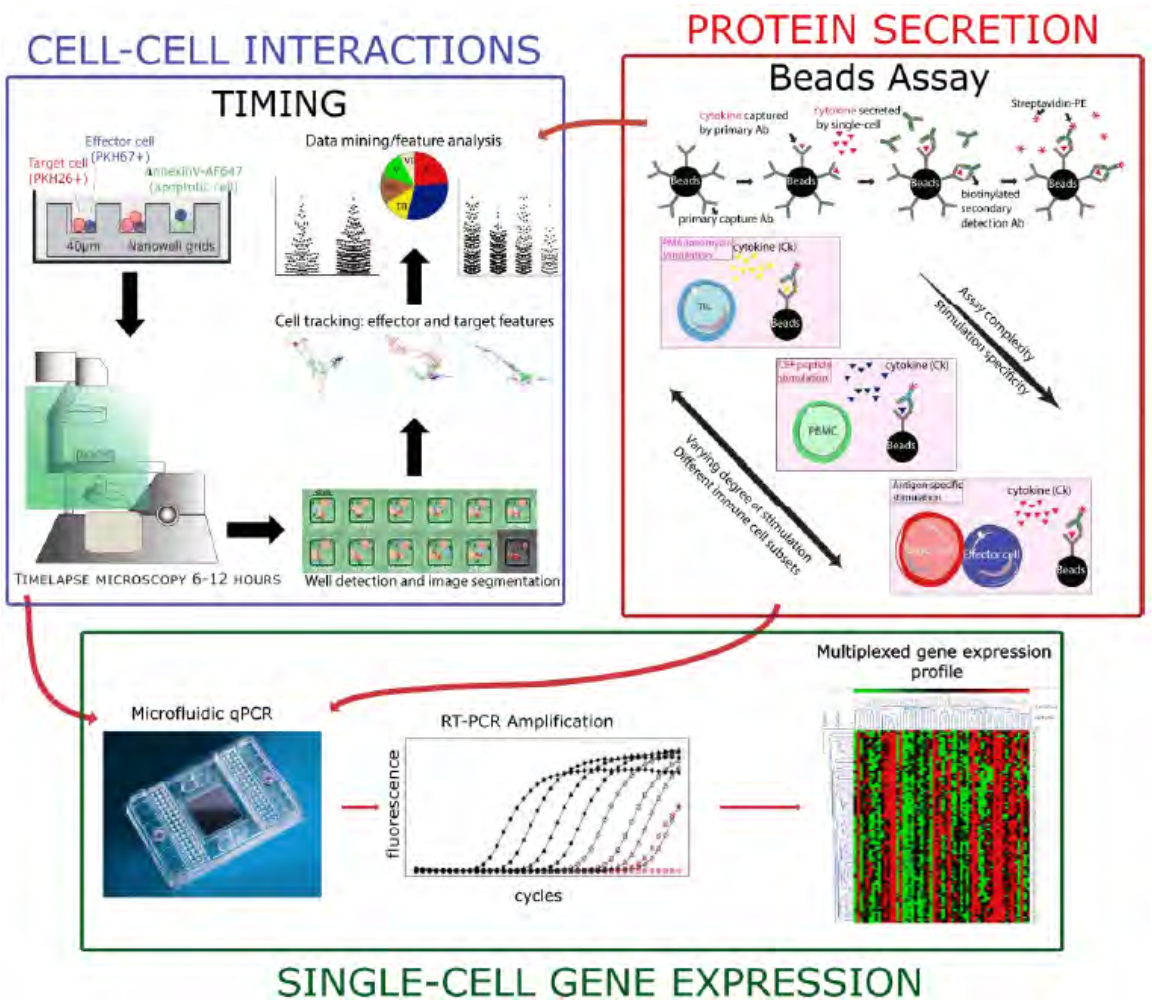

Figure 52: High-throughput multiplexed functional and molecular profiling of single-cell through combination of beads assay, TIMING and microfluidic qPCR

Starting with our recently reported Time-lapse Imaging Microscopy In Nanowell Grids (TIMING) (113), a high-throughput analytical platform for monitoring dynamic cellular behavior, we implemented functionalized beads as biosensors of the local microenvironment within individual nanowells to profile cytokine secretion (**Figure 53**), and microfluidic qPCR to facilitate gene expression profiling. Effector cells and target cells were labeled with PKH67 and PKH26 (Sigma) respectively and cytokine-positive beads fluoresced in red (Streptavidin-PE).

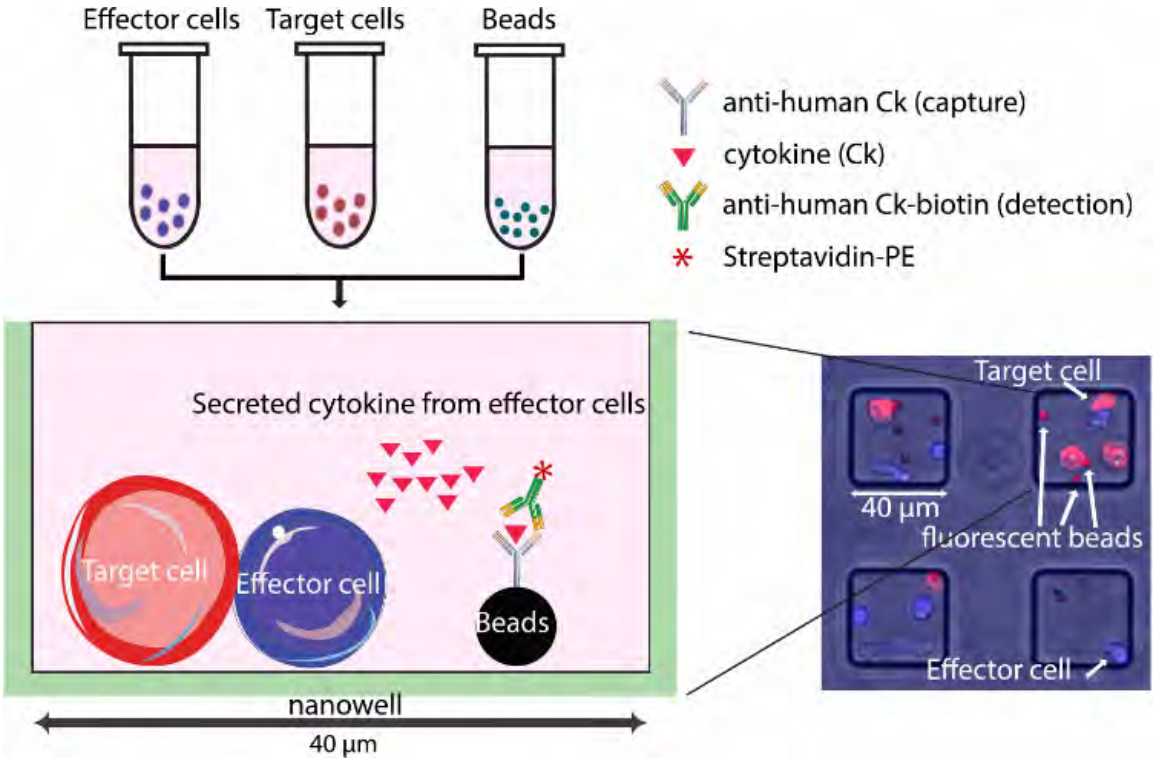

Figure 53: Schematic of beads assay and antibodies sandwich to detect cytokine secreted from single-cell.

This integrated approach could thus be used to profile cytokine secretion simultaneously with cytotoxicity, on one unified microscope platform.

3.3.2. Frequency of IFNγ-secreting T cells enumerated by functionalized microbeads within nanowell arrays is correlated to the same responses determined using ELISpot.

We first tested the ability of functionalized microbeads to efficiently capture proteins secreted by single cells after incubation in individual nanowells by measuring the limit of detection (LoD) of functionalized beads at different concentrations of the analyte. Briefly, antibody-coated beads were incubated with varying concentrations of IFN-γ (0 – 5000 pg/mL) for a period of two hours at 37 °C, loaded onto nanowell arrays, and subsequently detected with a fluorescently labeled secondary antibody. The background

corrected mean fluorescent intensity (MFI) quantified across a minimum of 30 beads confirmed that IFN-γ was detectable at a concentration of 500 pg/mL **(Figure 54)**.

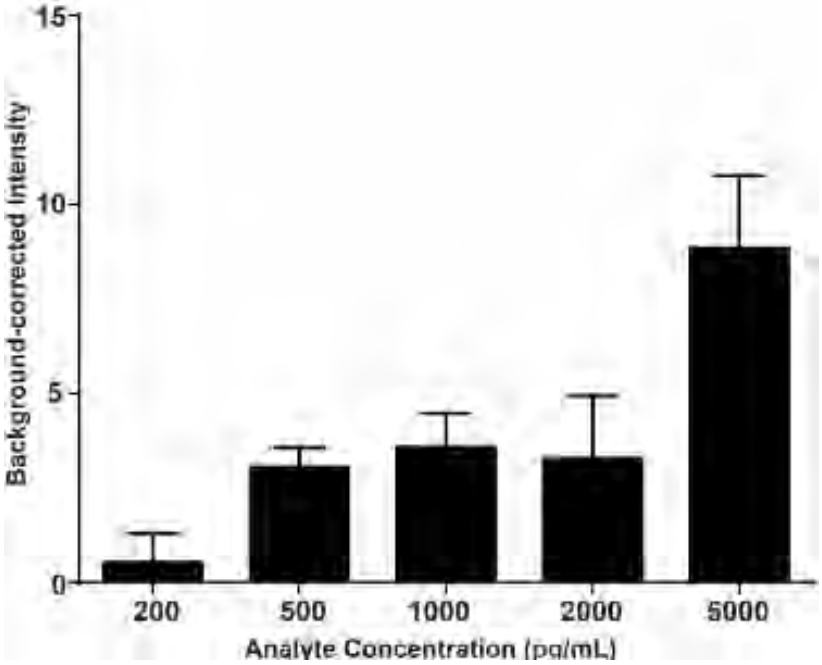

Figure 54: Background-corrected mean fluorescence intensity (MFI) detected from a minimum of 30 IFNγ-positive beads, as a function of IFNγ analyte concentration.

Next, the correlation between the nanowell encapsulated bead assay and ELISpot for quantifying frequencies of single T cells secreting IFN-γ upon activation was determined. To account for variations in stimulus and the diversity of T-cell populations, the frequency of IFN-γ secreting single T cells was enumerated under three sets of conditions: stimulation of peripheral blood mononuclear cells (PBMC) with HLA-class I peptide pools targeting common viral antigens; stimulation of PBMC with phorbol 12-myristate 13-acetate (PMA)/ionomycin; and stimulation of *in vitro* expanded, melanoma-specific TIL with PMA/ionomycin. An aliquot of 10^6 cells were stimulated for a period of 3-5 h and an aliquot of ~100,000 cells was loaded onto a nanowell array (84,672 nanowells, 125pL each). A suspension of 200,000 beads pre-coated with anti-IFN-γ was subsequently

loaded onto the nanowell array and incubated for a period of 2 h at 37 °C. By analyzing an average of 10,182 ± 8,589 (mean ± s.d.) single cells matched to one or more beads within the nanowells, the frequency of the activated T-cell IFN-γ response was determined to be 0.40 – 7.8 %. The magnitude of these responses were similar to those recorded by ELISpot [0.20 – 11.2 %], and results of both assays were significantly correlated ($r^2 = 0.87$, *p*-value = 0.0008), demonstrating that beads can be efficiently utilized to capture cytokine secretion from single cells (**Figure 55)**.

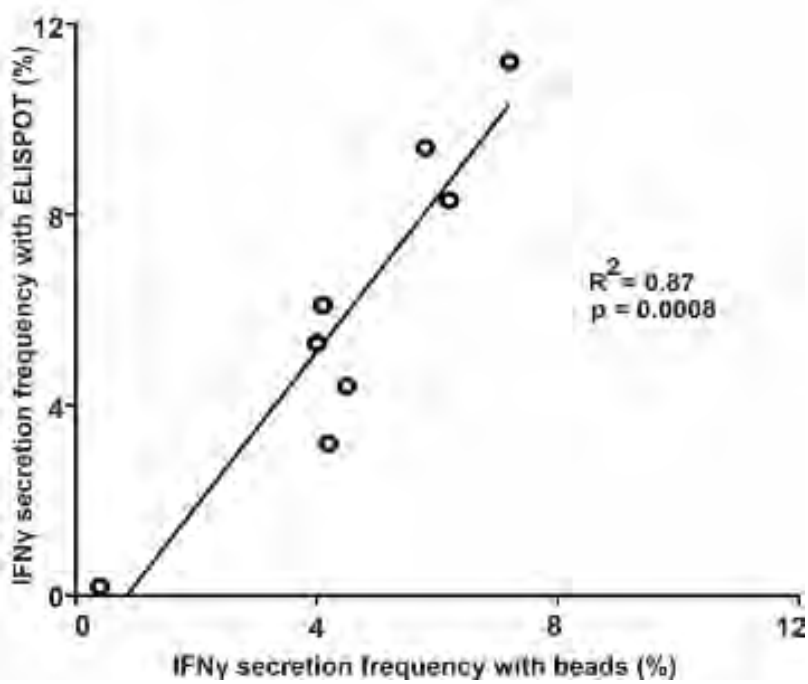

Figure 55: Comparison of the bead assay with ELISpot for detection of single-cell IFNγ secretion of different effector cells (PBMC and TIL) at varying level of antigenic stimulation.

In the absence of stimulation, the frequency of IFN-γ beads detected when incubated with T cells was < 1 in 10,000 and this set the limit of detection of our assay at 0.01%.

3.3.3. In open-well systems, fractional occupancy of analyte on beads increases as the density of the antibody used to capture analyte decreases.

As opposed to encapsulated systems, open-well configurations can be advantageous for the long term monitoring of cell fate and function since they allow continuous exchange of gases and nutrients. Furthermore, they avoid potential alterations of cellular behavior that can arise from the artificially high local concentrations of analytes commonly found in closed systems (118). A disadvantage of open-well systems is that the analyte secreted by an individual cell within a nanowell is subjected to persistent diffusion into the bulk medium, potentially lowering the sensitivity. We therefore sought to quantify the efficiency of analyte capture on beads by modeling a simplified open-well system using finite element simulations (**Figure 56**).

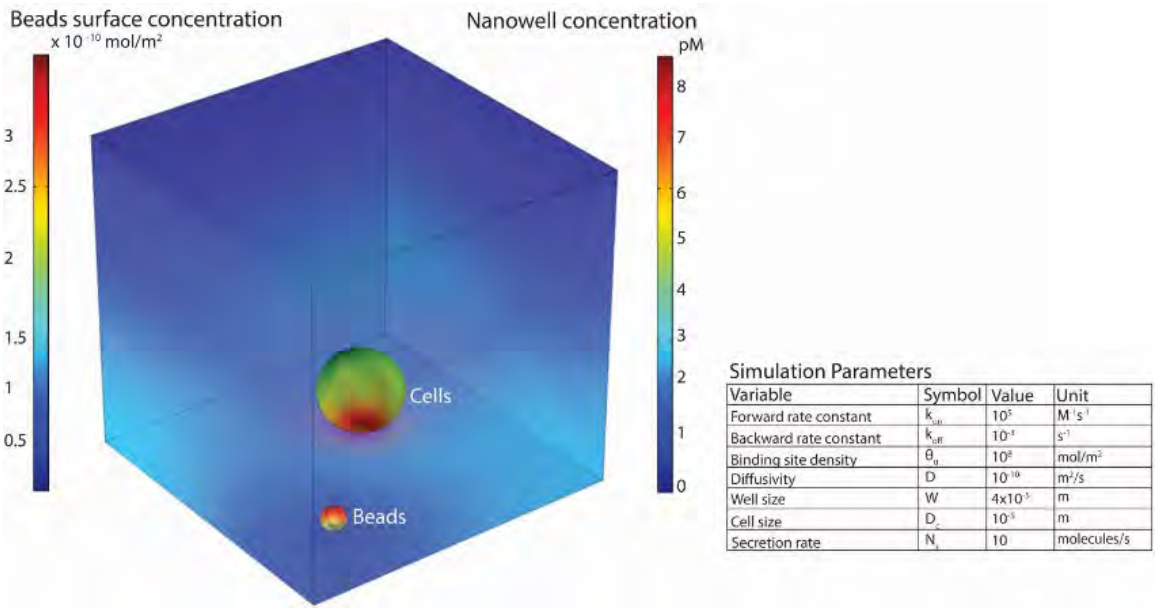

Figure 56: Heat maps showing analyte concentration in liquid phase across the well (right) and on the bead surface (left) after 5 hours of secretion in a 40 µm nanowell.

The concentration of analyte in liquid media (C) can be described using Fick`s 2nd law,

$$\frac{\partial C}{\partial t} = D\nabla^2 C \,, \tag{1}$$

where D represents the diffusion coefficient of the analyte.

Since the walls of the PDMS can be assumed to be largely impermeable to proteins (119), the flux at these boundaries was set to zero. At a constant rate of analyte secretion from the cell (10 molecules/sec), the mass balance of analyte concentration on bead surface (C_s) was determined by the equation:

$$\frac{\partial C_s}{\partial t} = D_s\nabla^2 C_s + k_{on}C(\theta_0 - C_s) - k_{off}C_s \,, \tag{2}$$

where D_s represents diffusivity of analyte on bead surface, k_{on} and k_{off} represent kinetic binding constants determined by strength of capture antibody – analyte interaction and θ_0 represents number of capture antibodies available per unit surface area of the bead.
The choice of parameter values (**Figure 56**) was based on commercially available antibody binding affinities, the known rates of cytokine secretion from T cells, and previously reported numerical simulations of closed systems (119).

Initial concentrations of analyte in liquid media and bead surface were set to zero and increase in fractional occupancy ($\oiint \frac{C_s}{\theta_0}$) of the bead with time as the cell secretes the analyte was modeled. Upon validating the model with previously published data (119), we sought to optimize two key tunable variables, the size of beads and the surface density of capture antibodies to maximize fractional occupancy (and therefore the fluorescent pixel intensity). The simulations demonstrated that the fractional occupancy of all three bead

sizes increased linearly as a function of time (1–6 h), and that regardless of the incubation time, the 3 µm bead had a 1.8-fold and 2.7-fold higher fractional occupancy in comparison to the 5 µm and 7 µm beads (**Figure 57**).

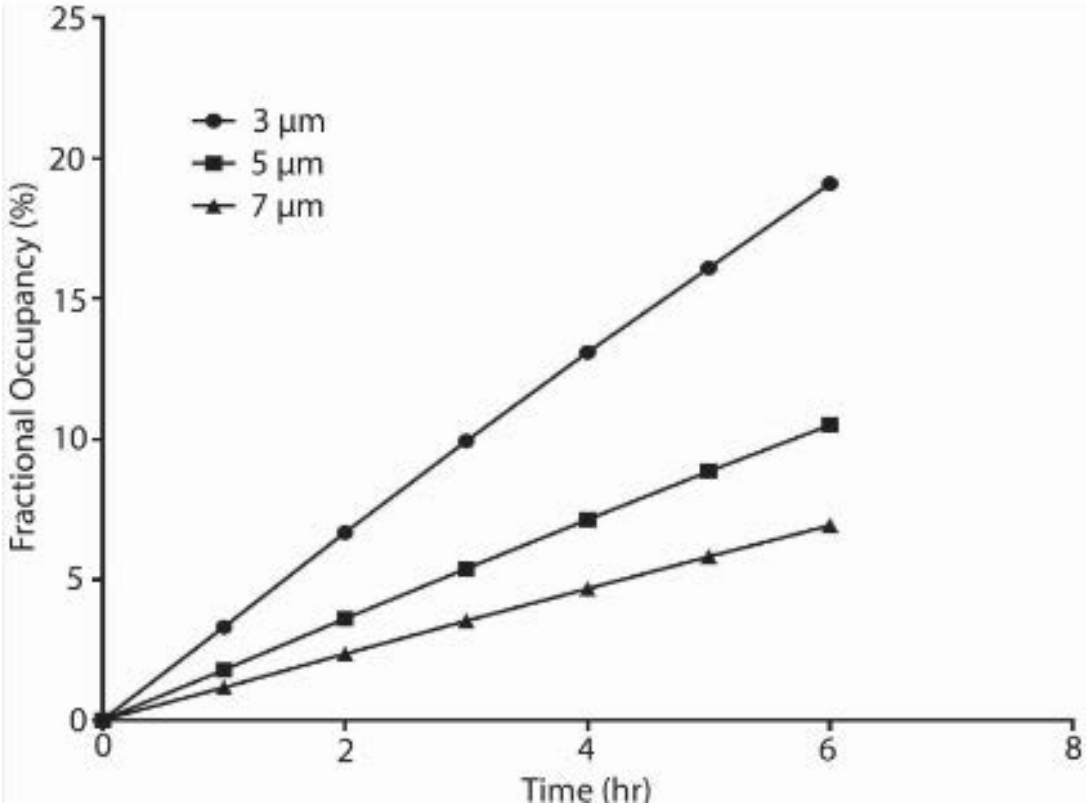

Figure 57: Fractional occupancy of beads of different sizes as a function of incubation time and their ability to capture analyte secreted from single cells.

When the bead diameter was held constant (3 µm), but the binding site density was varied across three orders of magnitude, the beads with the lowest binding site density (10^{-9} mol/m^2) had the highest fractional occupancy (**Figure 58**).

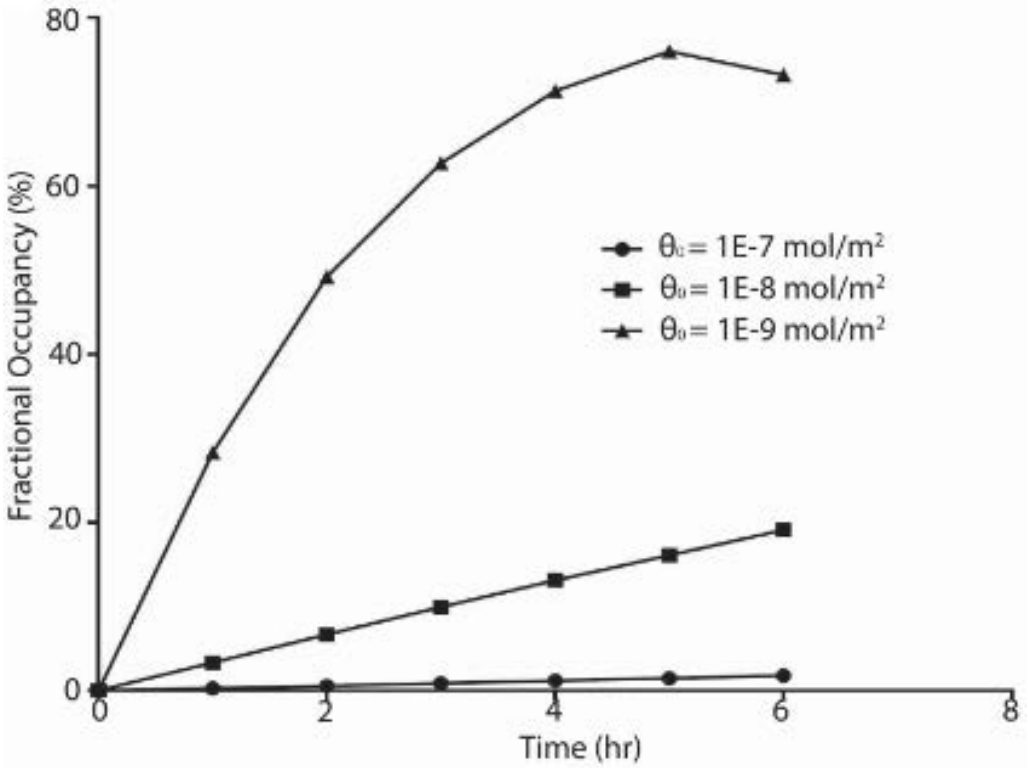

Figure 58: Fractional occupancy of 3 µm beads as a function of incubation time when the binding site density was varied across three orders of magnitude.

These results show that increased fractional occupancy is observed when the total number of binding sites is decreased by either decreasing the bead size, or binding site density, and are consistent with ambient analyte theory that predicts that higher sensitivity can be achieved by lowering the number of antibodies used to capture the analyte (120). Furthermore, for a nanomolar binder at low fractional occupancy (neglecting desorption), the simulations predicted that the kinetics of analyte capture is diffusion limited (**Figure 56**), in agreement with previous studies on antibody microspots, closed-well systems, and two-compartment mathematical models (119, 121). It should however be noted that unlike microspot assays, the present system does not conform to ambient analyte conditions as depletion of analyte by capture on the bead surface is not negligible in comparison to total analyte available.

3.3.4. Simultaneous quantification of cytotoxicity and IFN-γ secretion in tumor-specific CD8$^+$ CAR$^+$ T cells using TIMING.

We have recently developed TIMING as a method to interrogate the dynamics of cell-cell interactions in high-throughput by utilizing nanowell grids and automated time-lapse microscopy (112, 113). Since the end-point experiments confirmed the ability to detect IFN-γ from single T cells upon activation, and the modeling suggested that the beads should work well in an open-well system, we integrated the beads into the TIMING workflow to enable measurement of effector target interactions while also capturing any secreted IFN-γ protein, at single-cell resolution. We chose to interrogate the polyfunctionality of tumor-specific individual CD8$^+$ T cells with regards to cytokine secretion and cytotoxicity. Genetically modified and propagated T cells were generated from the peripheral blood mononuclear cells (PBMC) of a healthy donor to enforce expression of a second generation CD19-specific CAR (designated CD19RCD28) that activates T cells via a chimeric CD3 and CD28 endodomain (**Figure 59**) (81).

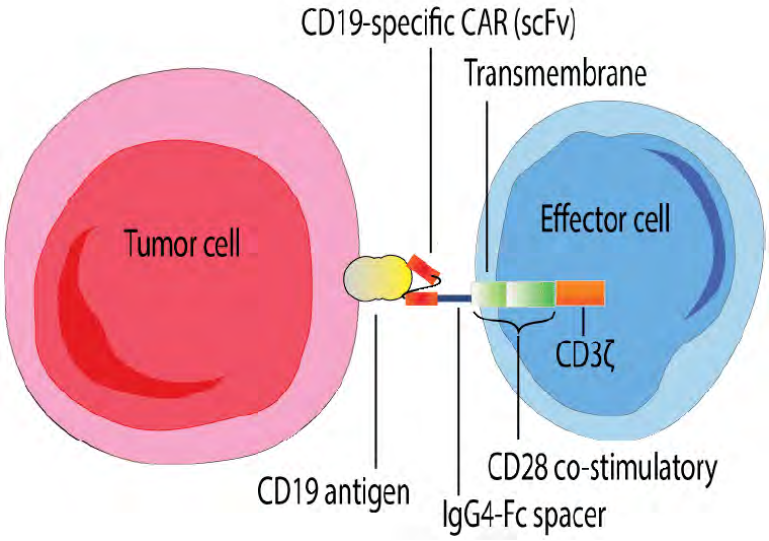

Figure 59: Schematic of effector cell (blue) that recognizes CD19 antigen on tumor cell (red) with second generation chimeric antigen receptor (CAR) that activates through CD3ζ and CD28 endodomains.

Subsequent to numeric expansion on activating and propagating cells (AaPC) for a period of four weeks, the CAR$^+$ T cells were predominantly CD8$^+$ (>99%, **Figure 60**).

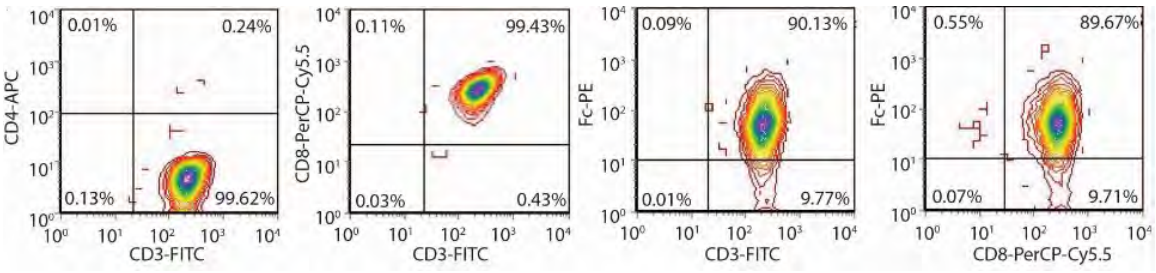

Figure 60: Phenotypic characterization of CAR$^+$ T cells with flow cytometry showed that the cells were predominantly CD8$^+$ with >90% expression of CAR.

Phenotypic characterization of the CD8$^+$CAR$^+$ T cells demonstrated that the dominant subset of T cells were naïve like (CD45RA$^+$CD62L$^+$, 60.7 %, **Figure 61**).

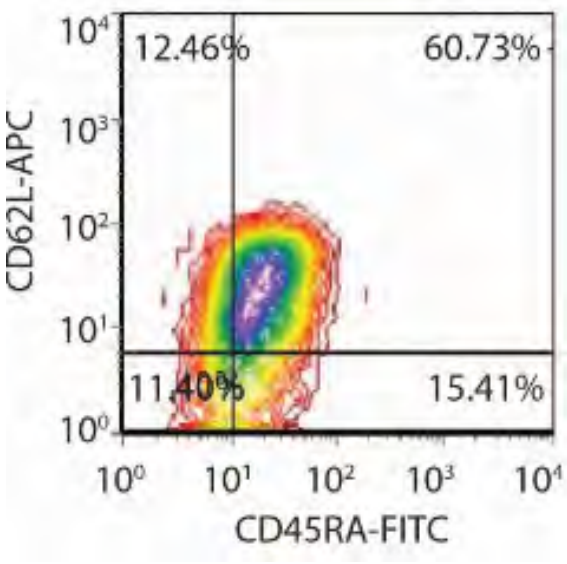

Figure 61: Dot plots obtained by staining with CD62L and CD45RA showed that the dominant subset of CAR$^+$ T cells (60.73 %) were naïve-like.

The ability of these T cells to specifically secrete IFN-γ upon interaction with cells presenting CD19 antigen was confirmed by co-incubating with both NALM-6 tumor cells (CD19 positive) and EL4 cells (CD19 negative, **Figure 62**).

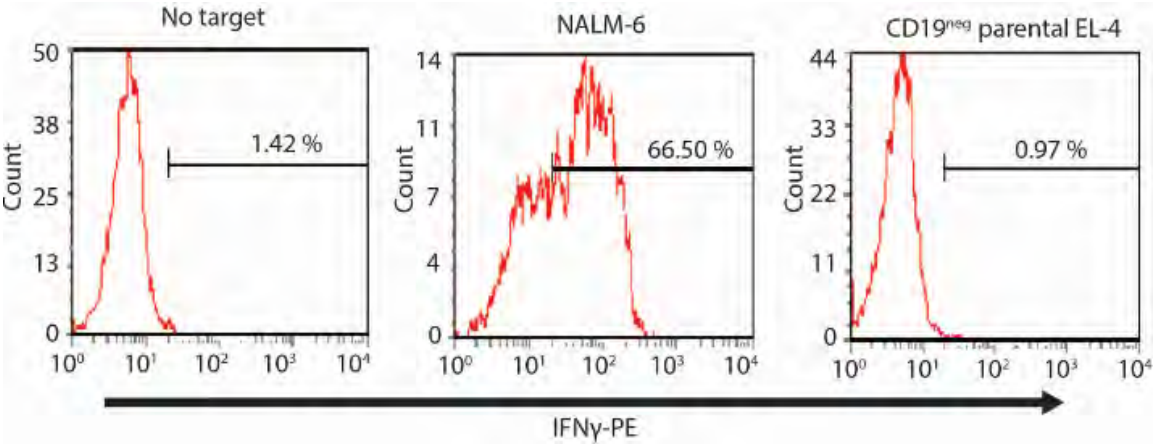

Figure 62: Intracellular staining confirmed the ability of CAR$^+$ T cells to specifically upregulate IFNγ expression upon recognition of target cells expressing cognate antigen. Effector: Target ratio 1:5.

CAR$^+$ T cells as effectors, NALM-6 tumor cells as targets, and pre-functionalized beads coated with IFN-γ capture antibody as cytokine sensors, were loaded sequentially onto a nanowell grid array. Effector-mediated tumor lysis was detected using Annexin V staining and every individual nanowell (14,400 wells, 64 pL each) was profiled for a period of 5 h, and cytokine secretion was quantified by the formation of immune-sandwiches on beads (**Figure 63**).

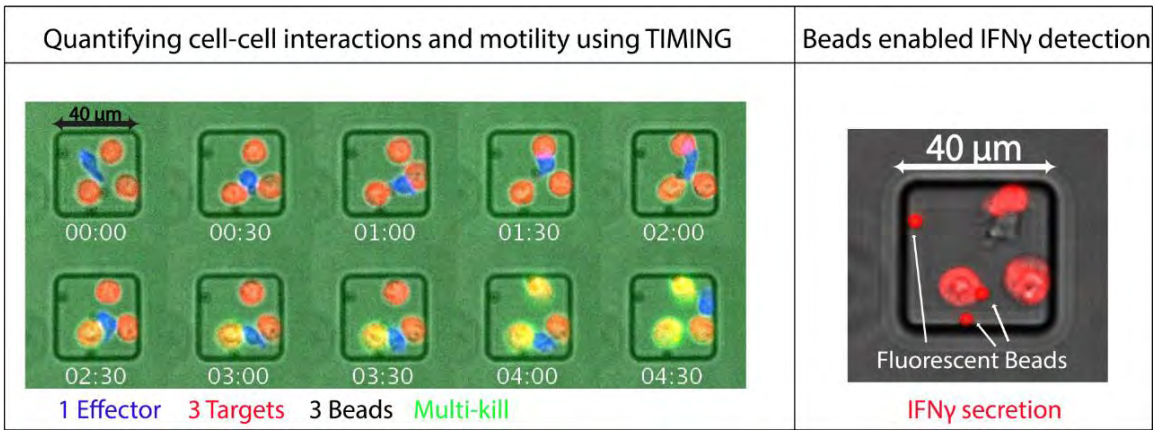

Figure 63: Combining TIMING with bead based assays to interrogate multi-functionality of CAR$^+$ T cells at the single-cell level.

We modified our previously-reported image analysis algorithms to not only enable the automated segmentation and tracking of cells, but to now facilitate the identification of fluorescence intensity on the beads to report on the secretion of IFN-γ. After a simple diameter-based gating, we identified 1,178 wells of interest containing a single T cell, 2 to 5 tumor cells, and one or more beads. Nanowells containing multiple tumor cells were specifically chosen to allow observation of individual T cells participating in multiple killing events. Within this subset, since every T cell was incubated with multiple tumor cells, three separate functional definitions were employed: serial killer cells that killed at least two tumor cells, mono-killer cells that killed exactly one tumor cell, and IFN-γ secreting cells. Subsequent to conjugation to one or more tumor cells, IFN-γ secretion was the most commonly observed function recorded in single T cells (64.2 %, **Figure 64**).

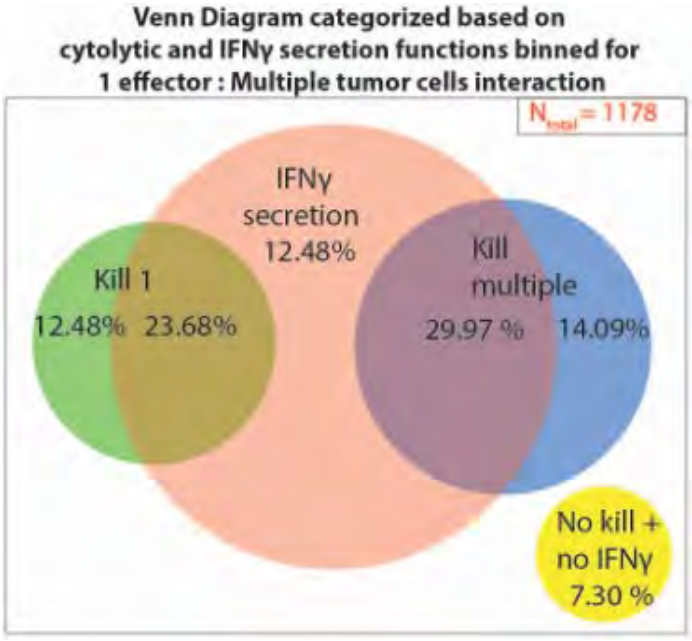

Figure 64: Venn Diagram showing breakdown of CD8⁺ T cell functionality based on killing (no kill, kill one, and kill multiple) and/or IFNγ secretion

Polyfunctional cells defined as either CAR^+ T cells that killed multiple tumor cells (44.1 %) or cells that were able to kill at least one tumor cell and simultaneously secrete IFN-γ was only slightly lower (53.6 %, **Figure 64).** The subset of cells capable of both multi-killing and IFN-γ secretion comprised 30% of the population.

3.3.5. Killer CAR^+ T cells detach faster from target cells in comparison to IFN-γ secreting cells.

Since TIMING assays, as described above, have the ability to monitor both conjugate formation and functional readouts, and since the $CD8^+$ T cells uniformly expressed the high-affinity immunoreceptor, we quantified the threshold for activation by analyzing the total duration of conjugation prior to functional readout. T cells that only secreted IFN-γ (monofunctional), exhibited the longest conjugation durations of all functional T cells (159±8 min). This duration was significantly longer than cells that killed either only one tumor cell with (94±5 min) or without IFN-γ (89±6 min) secretion, or multiple tumor cells with (74±2 min) or without IFN-γ (79±4 min) (**Figure 65**). * $P<0.05$, ** $P< 0.01$, *** $P< 0.001$, and **** $P< 0.0001$.

These results suggest that the duration of conjugation between T cells and tumor cells that results in killing has a lower threshold for functional activation in comparison to IFN-γ (monofunction). To define the kinetics of the interaction between individual T cells and tumor cells that lead to subsequent killing, two interaction parameters, $t_{Contact}$, cumulative duration of conjugation between first contact to target death; and t_{Death}, time between first contact and target apoptosis, were computed (**Figure 21**). The $t_{Contact}$ parameter reflects the duration of stable conjugation and t_{Death} reflects the kinetics of target

apoptosis. For both mono-killers and serial killers, $t_{Contact}$ was significantly lower than t_{Death} demonstrating that T cell detachment preceded tumor-cell Annexin V staining (**Figure 66**).

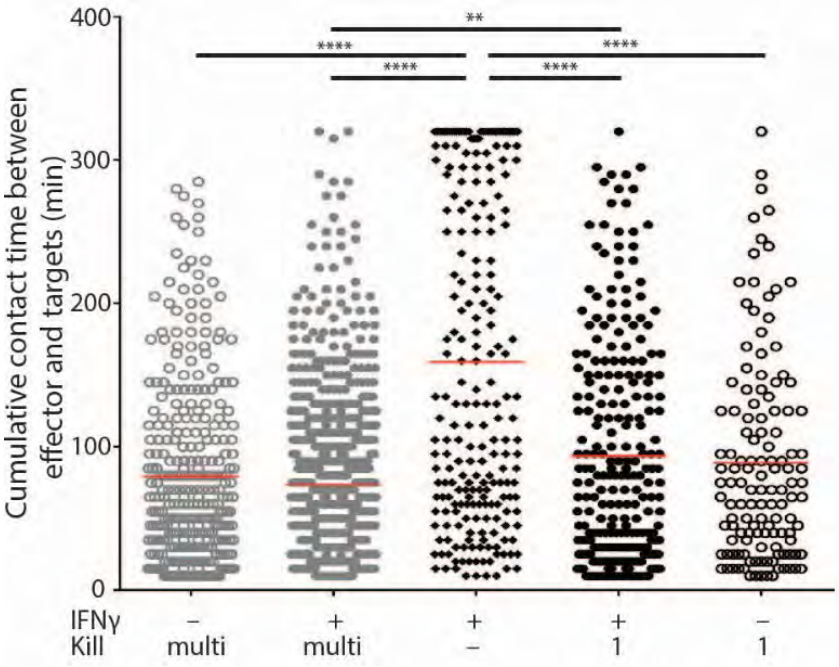

Figure 65: Cumulative contact duration between effector and targets (min) leading to the different functional outcomes.

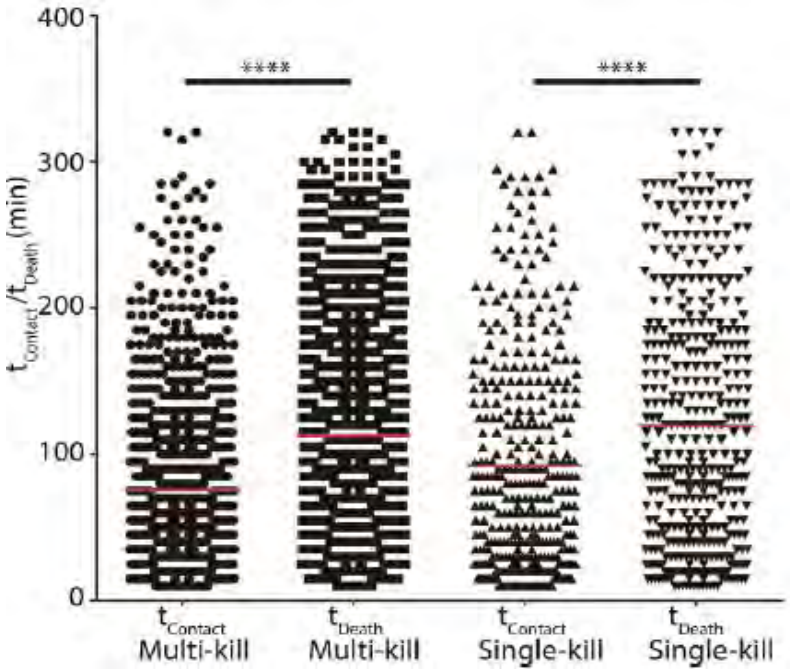

Figure 66: $t_{Contact}/t_{Death}$ comparison for multi-killer vs mono-killer T cells.

Second, the total duration of conjugation of all killer T cells (81±2 min) was lower than non-killer T cells (154±6 min) [*p-value* <0.0001, **Figure 67]**.

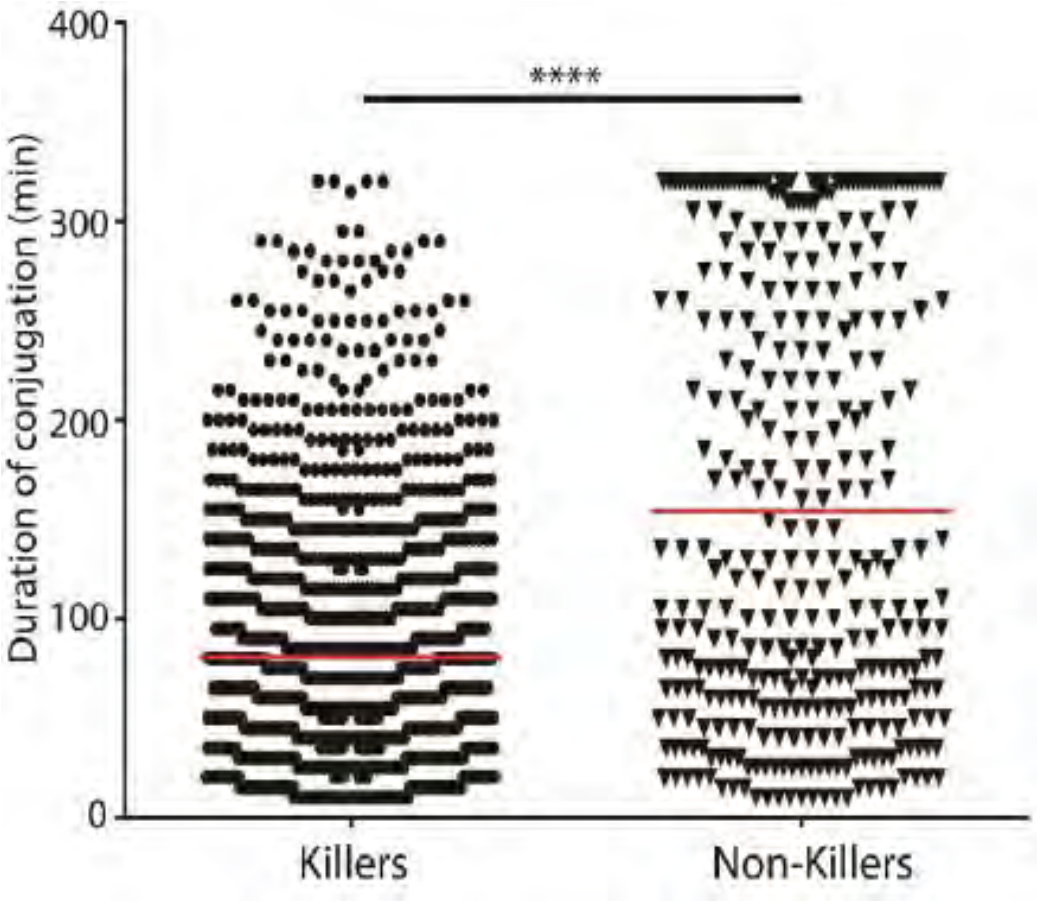

Figure 67: Comparison of duration of conjugation of killers and non-killer T cells (irrespective of IFNγ secretion).

These results suggest that while at the single-cell level the relationship between exact time at which single T cells terminate the synapse and time of target cell apoptosis is heterogeneous; in aggregate killer T cells terminated the synapse upon initiation of killing but prior to appearance of the apoptosis markers on tumor cells.

No significant differences were observed in the $t_{Contact}$ when comparing serial killer CAR^+ T cells, with or without IFN-γ secretion (**Figure 68**), suggesting that killing is the dominant behavior in determining duration of conjugation.

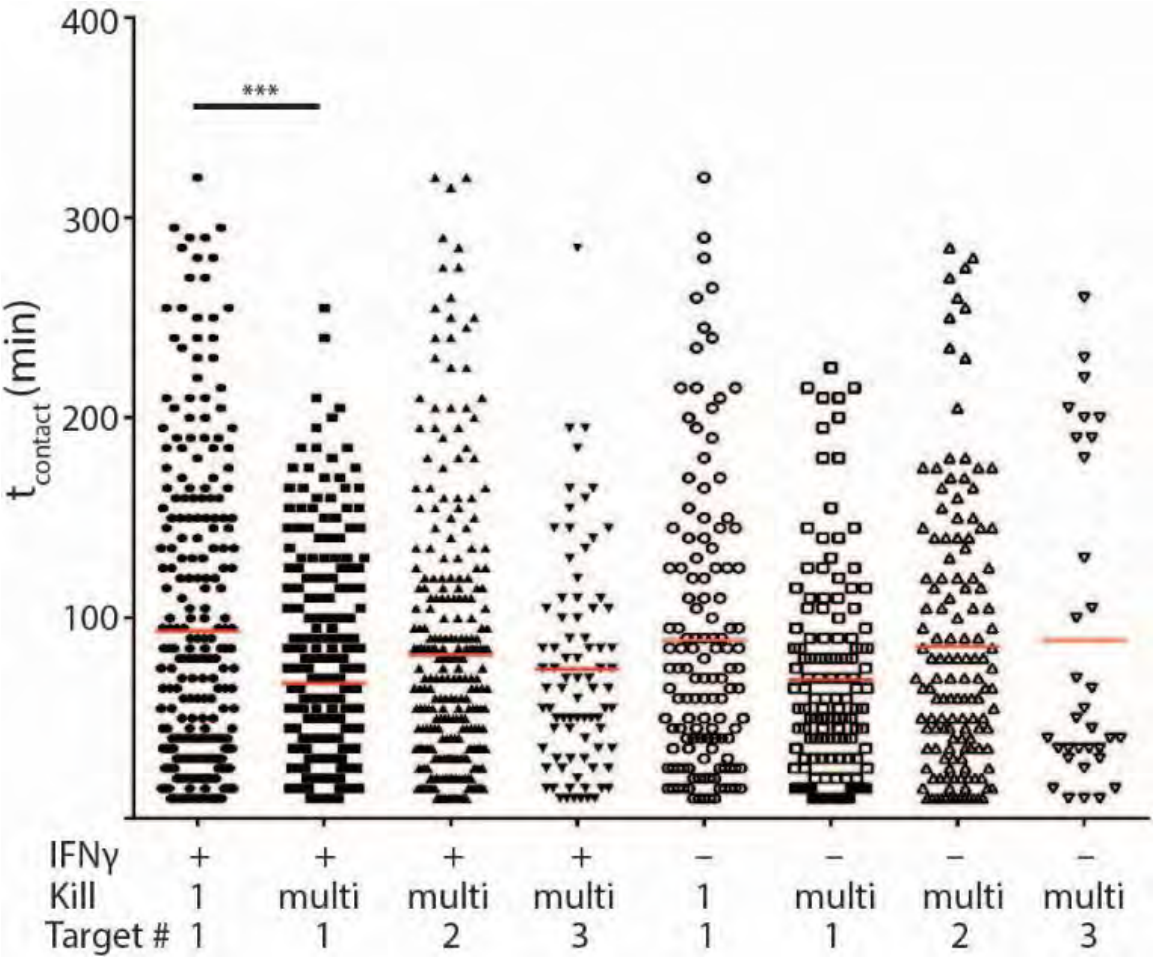

Figure 68: Kinetics of killing based on $t_{Contact}$ of mono-killer and multi killer (first, second, and third target killed respectively) for subsets of effector that participate in killing and/or IFNγ secretion.

The frequency of individual serial killer T cells however that either secreted IFN-γ (353/1178 = 30 %) or did not secrete IFN γ (166/1178 = 14 %) was not significantly different from T cells that only secreted IFN-γ (147/1178 = 12 %) (Fisher 2x2 test, *p-value*

= 0.2) confirming that shorter duration of conjugation still provided sufficient activation for cytokine secretion.

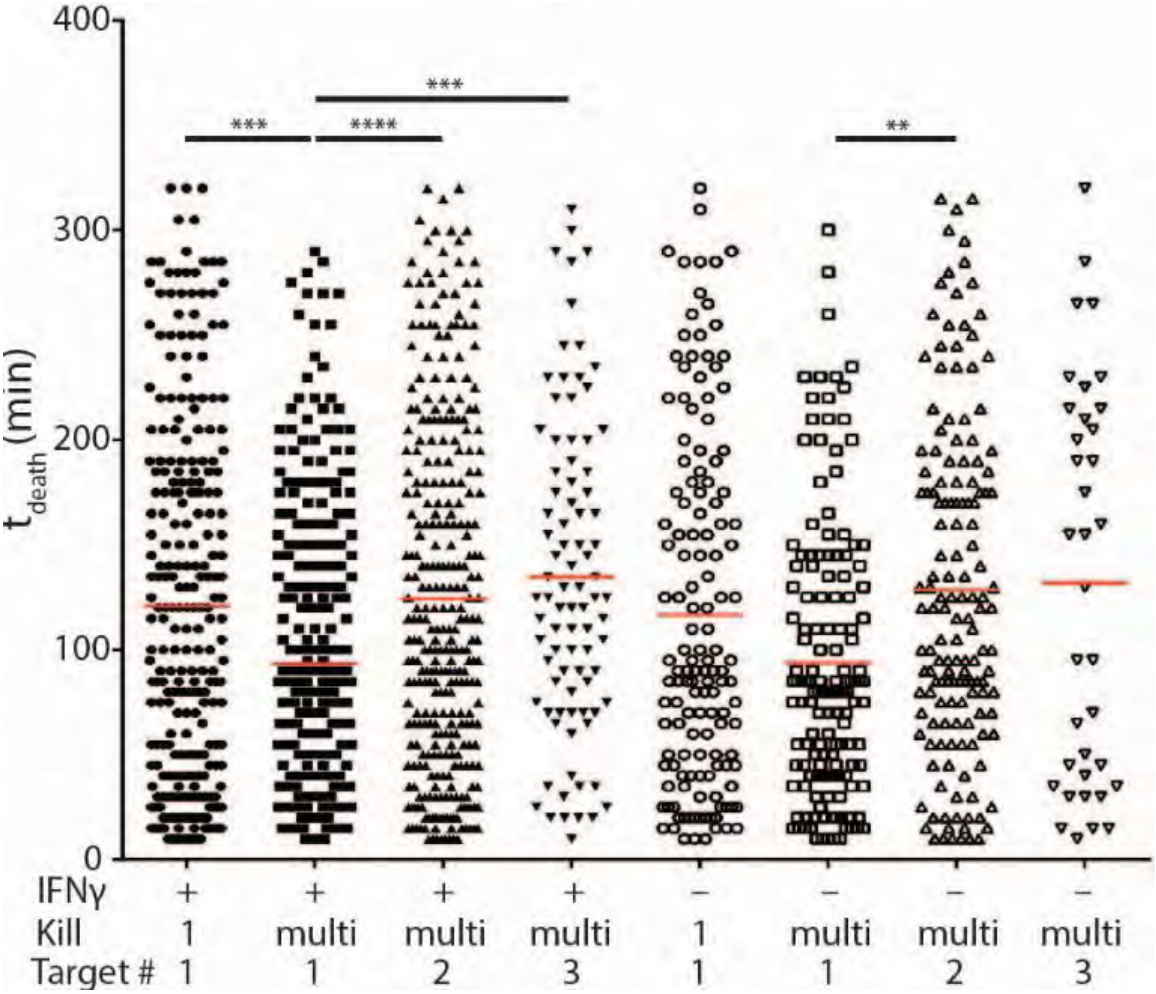

Figure 69: Kinetics of killing based on and t_{Death} of mono- and multi-killer (first, second, and third target killed respectively) for subsets of effector that participate in killing and/or IFNγ secretion.

We next compared mono-killers and serial killers, with and without concomitant IFN-γ secretion, measured by $t_{Contact}$ and t_{Death}. In order to facilitate direct comparisons, each of the targets killed by the serial killer T cells was sorted based on the order in which they made contact with the effector cell. In the absence of IFN-γ secretion, serial killer effector cells showed no significant differences in either $t_{Contact}$ (69±5 min) or t_{Death} (94±6 min) in

killing of the first target encountered, in comparison to mono-killers ($t_{Contact}$: 89±6 min, t_{Death}: 117±7 min, **Figure 68 and 69**).

In contrast, serial killer effector cells that also secreted IFN-γ showed a decreased duration of conjugation ($t_{Contact}$: 68±3 min) and an increased efficiency (t_{Death}: 93±4 min) in killing of the first target encountered, in comparison to mono-killers that secreted IFN-γ ($t_{Contact}$: 94±5 min, t_{Death}: 121±5 min). This difference was only observed for the first target since subsequent targets killed by the serial killers did not show significant differences in either $t_{Contact}$ or t_{Death} (**Figure 68 and 69**). In summary, these results showed that polyfunctional T cells that are able to participate in both serial killing and secrete IFN-γ, have a lower threshold for the duration of activation prior to a functional response.

3.3.6. Basal motility when not in target cell contact may be used to identify serial killer polyfunctional CAR$^+$ T cells.

Next, we investigated if intrinsic T-cell behavioral parameters like basal motility (d_{Well}: average mean displacement within the nanowell over 5 minute periods) prior to tumor cell conjugation, might offer insights into their functional capacity subsequent to tumor cell conjugation. Individual CAR$^+$ T cells that failed to display any functionality (killing/IFN-γ secretion) upon tumor cell conjugation also had the least out-of-contact motility (d_{Well}: 1.3 ± 0.1 μm) of the T cells subgroups profiled (**Figures 70**). In contrast, effector cells that were able to kill multiple tumor cells and secrete IFN-γ exhibited a significantly higher out-of-contact motility (d_{Well}: 2.2 ± 0.1 μm) compared to those that only secreted IFN-γ without killing (d_{Well}: 1.6 ± 0.1 μm), and the aforementioned non-functional T cells (*p*-value = 0.043 and 0.002 respectively) (**Figure 70)**.

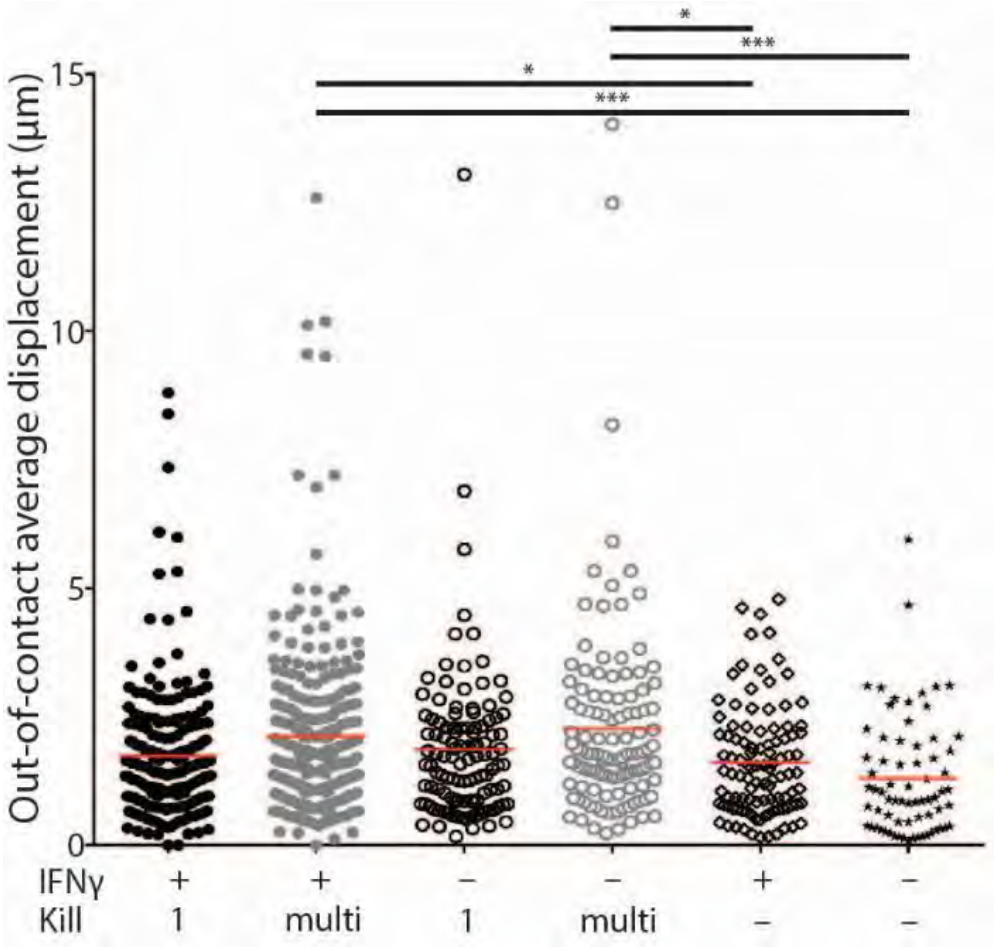

Figure 70: Average displacement, d_{Well} (µm) calculated for different combination of functionality of killing and IFNγ secretion of CAR^+ T cell.

This observation of higher motility was also recorded with serial killer effector cells that did not secrete IFN-γ (d_{Well}: 2.4 ± 0.2 µm) in comparison with effector cells that only secreted IFN-γ or non-functional cells (*p-value* =0.007 and 0.0002 respectively). Remarkably, these observations, however were not true for effector cells that were only capable of killing one tumor cell, as their average displacement were not significantly higher compared to those that did not kill, suggesting that serial killers perhaps benefit from the high motility allowing for rapid discovery of targets within the local micro-environment. These observations were only true for the out-of-contact motility and not

surprisingly, regardless of the function elicited, all functional effector cells showed no differences in motility during conjugation with the tumor cell (**Figure 71**).

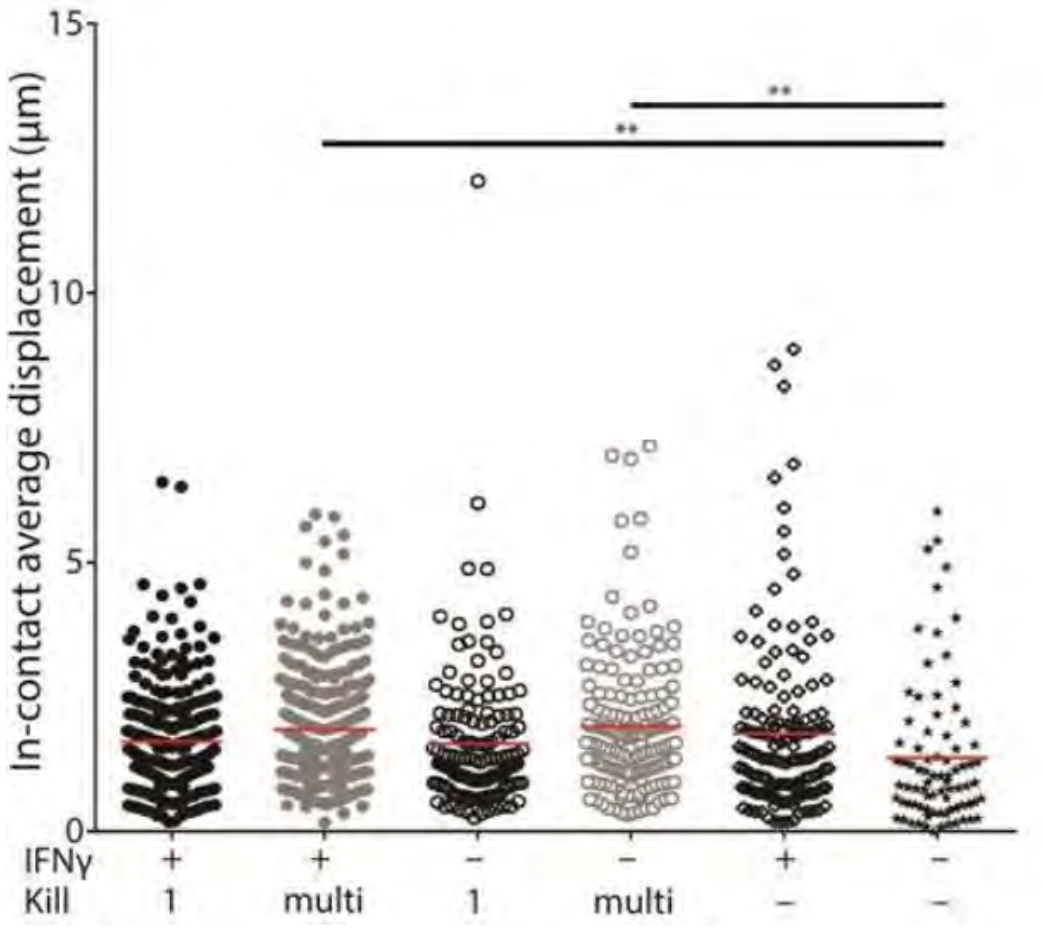

Figure 71: Average displacements of effector cells during conjugation of effector with target cells per frame interval (5 min) at E:T ratio of 1:2-5

3.3.7. Transcriptional profiling of motile CAR$^+$ T cells reveals an activated phenotype.

Since the TIMING results indicated that the basal motility may be able to identify polyfunctional killer cells, we next sought to define the underlying molecular profile of motile CD8$^+$ T cells. Accordingly, a set of 90 genes relevant to T-cell function were identified, and multiplexed, single cell, RT-qPCR was performed (**Table 4**). In order to study the basal motility of these CD8$^+$ T cells, a TIMING experiment was set up to track

individual live T cells without the influence of the tumor cells. Single cells were picked up based on their motility profile: "motile or high motility" (d_{well}: 2.6 ± 0.8µm, n=41) or "non-motile or low motility" (d_{well}: 0.8 ± 0.4µm n=43) and their transcriptional profile determined (**Figure 72** and **Figure 73**). X, Y coordinates are shown in microns relative to initial cell position set to the origin. Color map represents aspect ratio of cell polarization with red denoting circular cells and increasing shades of green and blue denoting elongated cells.

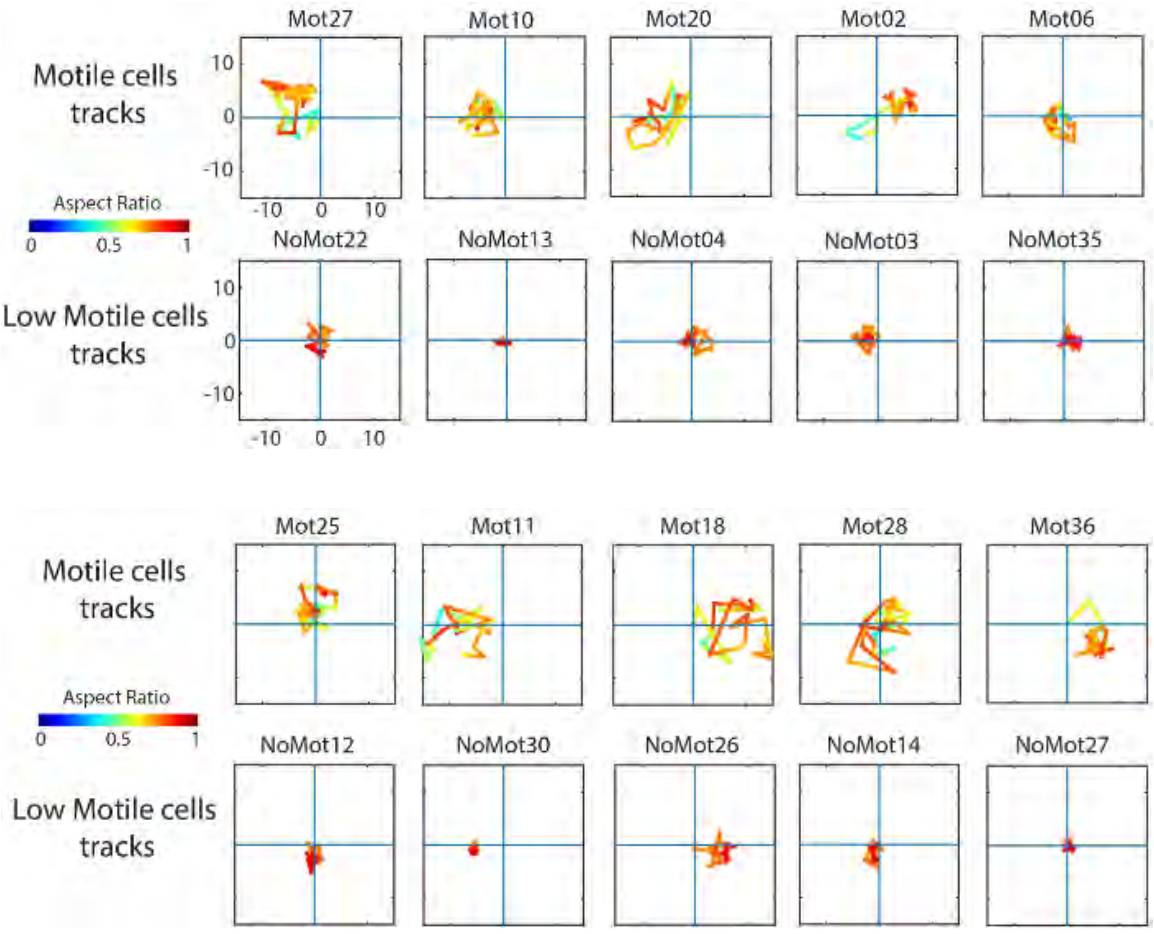

Figure 72: Representatives examples of high and low motility cell tracks during the 3 hour TIMING experiment.

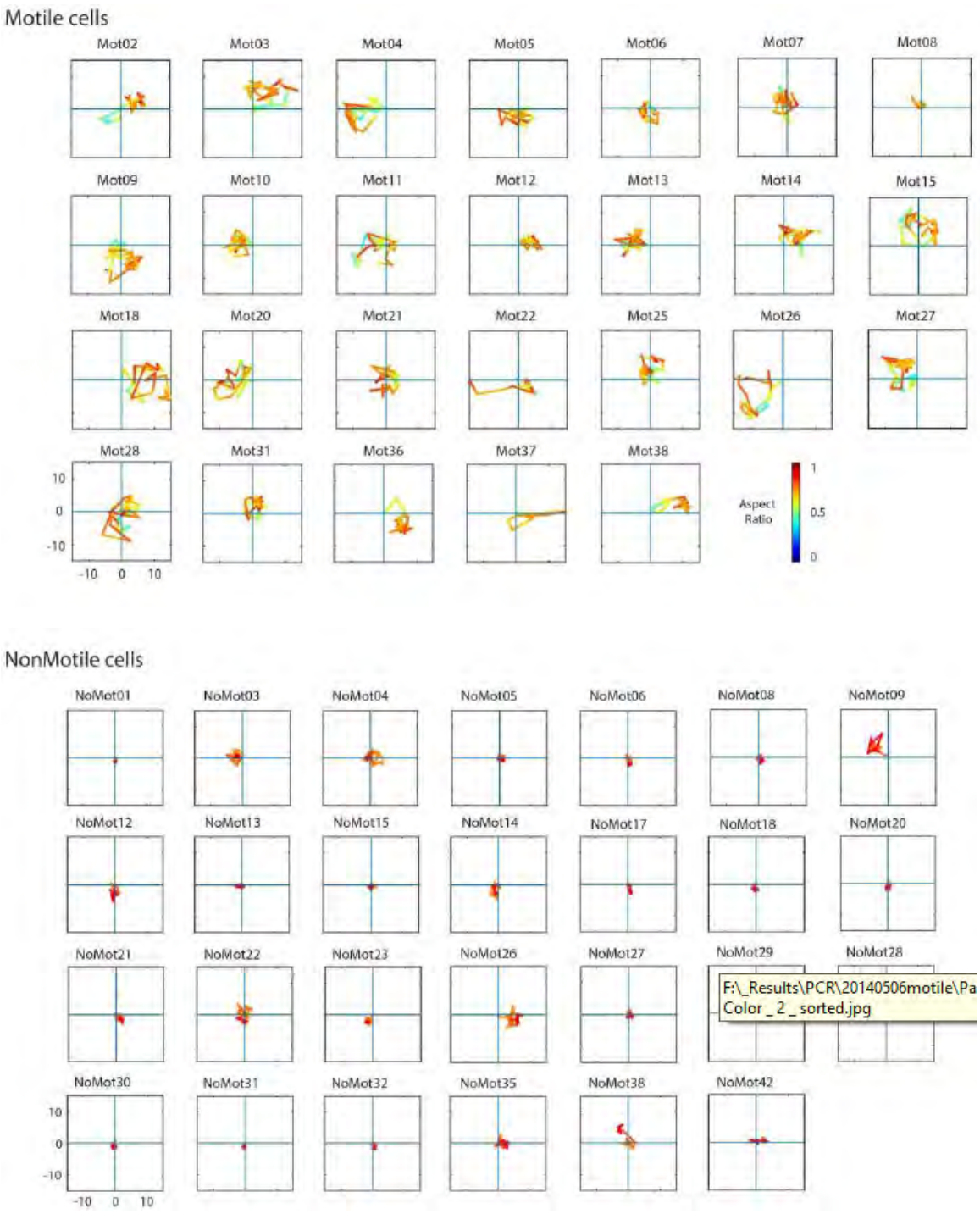

Figure 73: Position tracks of high and low motility CD8⁺ T cells during 3 hours of TIMING experiment, showing the larger scanning area and the lower circularity of high motility cells.

After microfluidic qPCR, and subsequent to filtering, t-test comparisons of 62 genes between the motile and non-motile groups showed that 15 genes had significantly altered level of expression ($p < 0.05$) and more than a 1.5 fold change: *CD244, CD58, LAG3, CTLA4, CD86* (activation markers)*; CCR1*, *CXCR3, 1L18R1, IL2RB, IL4R* (chemokine and cytokine receptors), and *GATA3* (transcription factor) were upregulated, while *CX3CR1*, *CCR4* (chemokine receptors); *CD69* (activation marker), and *IRF4* (transcription factor) and were down-regulated (**Figure 74**).

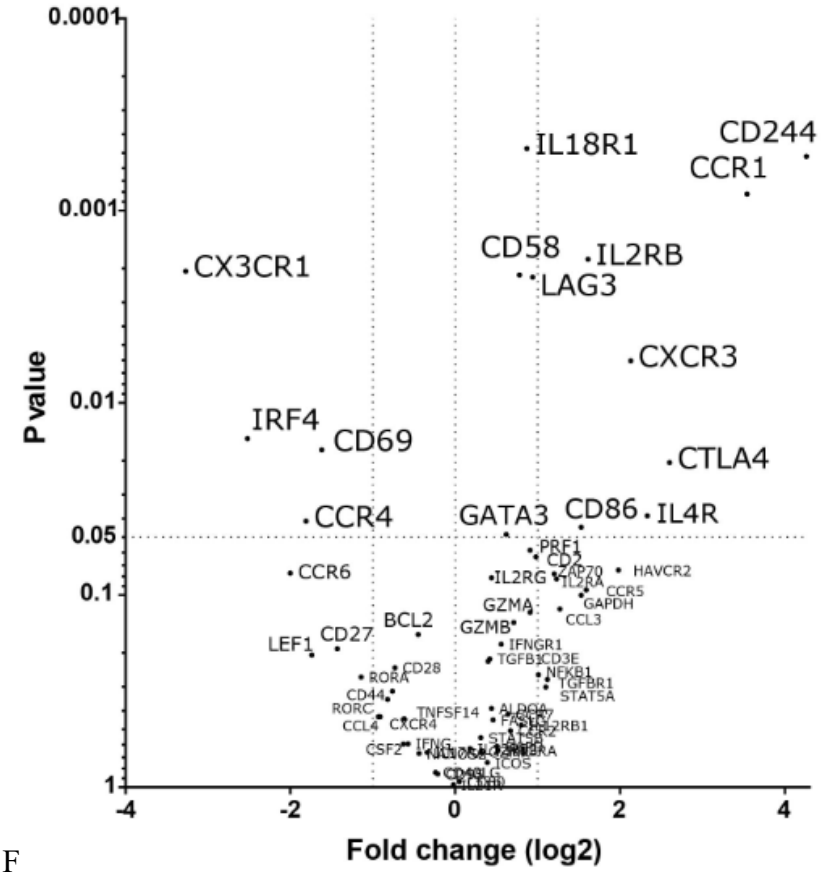

F

Figure 74: Volcano plot demonstrating the significance (t-test) and magnitude of fold-change comparing high and low motility CD8$^+$ T cells.

Unsupervised hierarchical clustering (analysis with MeV, Pearson correlation and complete linkage) (122) was performed with gene- and cell-normalized data of these 15

genes, and the sample clustering achieved a classification according to the known categories (motile *vs.* non motile) with 83% accuracy (**Figure 75**). * and + denote the individual motile and non-motile cells whose tracks are shown in **Figure 72**. When we repeated the agglomerative clustering with the motility-specific features d_{well} and aspect ratio (AR, ratio of minor/major axes,) along the genes, the cluster tree structure was largely unaltered and d_{well} was closely clustered with expression of *CD244* and *IL2RB*, while AR was highly correlated to *IRF4* (**Figure 76**).

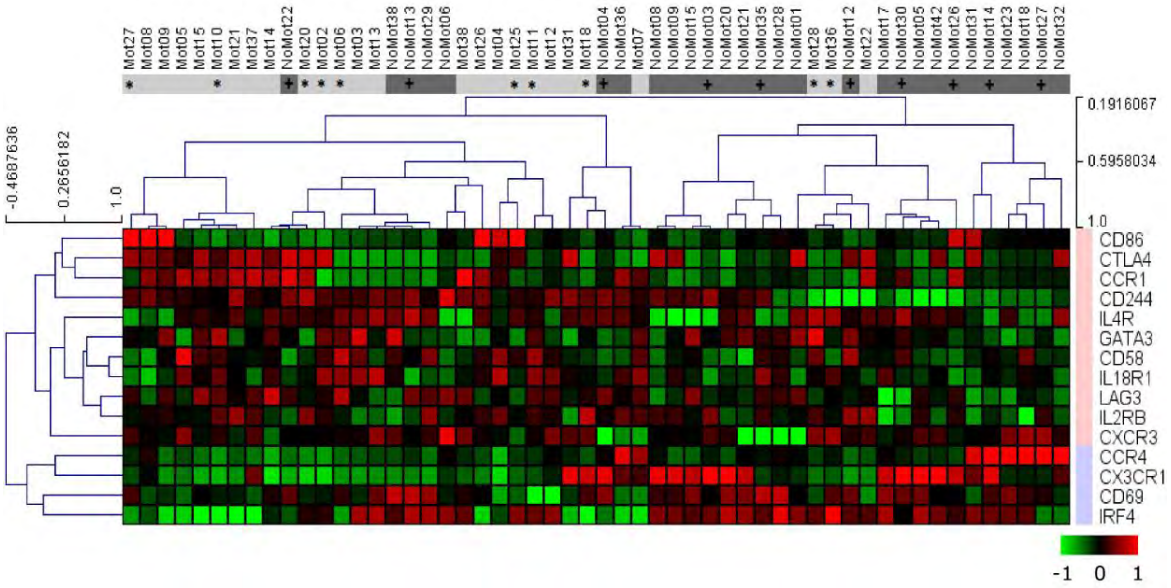

Figure 75: Unsupervised hierarchical bi-clustering of samples and of the genes identified as having a significant difference (p-value < 0.05) and net fold-change of >1.5.

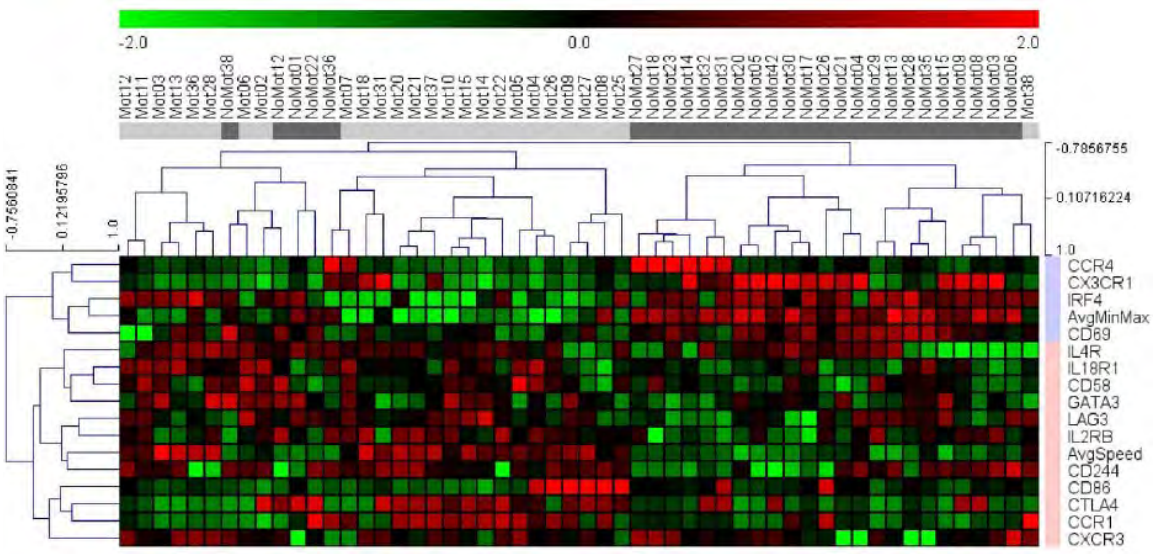

Figure 76: Unsupervised hierarchical bi-clustering represented as heatmap of samples and of the genes along with the average speed and average aspect ratio (Min/Max) of the individual T cells.

While the comparisons of transcriptional profiles with student's t-test and hierarchical clustering enabled us to infer differences between the motile and non-motile groups, we hypothesized that the heterogeneity of this cell population could be also described as a progression of cells characterized by gradual changes in gene expression from cell to cell. The set of fifteen differentially expressed genes and the two motility parameters, d_{Well} and AR, were used as the base set for the subspace trend discovery tool STrenD that identified ten genes considered to support the progression (**Figure 77**) (123).

With the selected genes and features, STrenD outputs a tree structure representing the progression of cells identified by the input features (**Figure 78**). By visualizing and coloring the tree using TreeVis (124), we can clearly identify non motile cells clustered together at the center-right side of the tree, while motile cells split out of this pool into two branches, one with high expression of *IL2RB*, *IL18R1, CD58*, *LAG3* and *GATA3* (**Figure 69**, upper left branch), one with low expression of these and with very low expression of

IRF4, but still with high motility and high *CD244* expression (**Figure 78**, lower left branch).

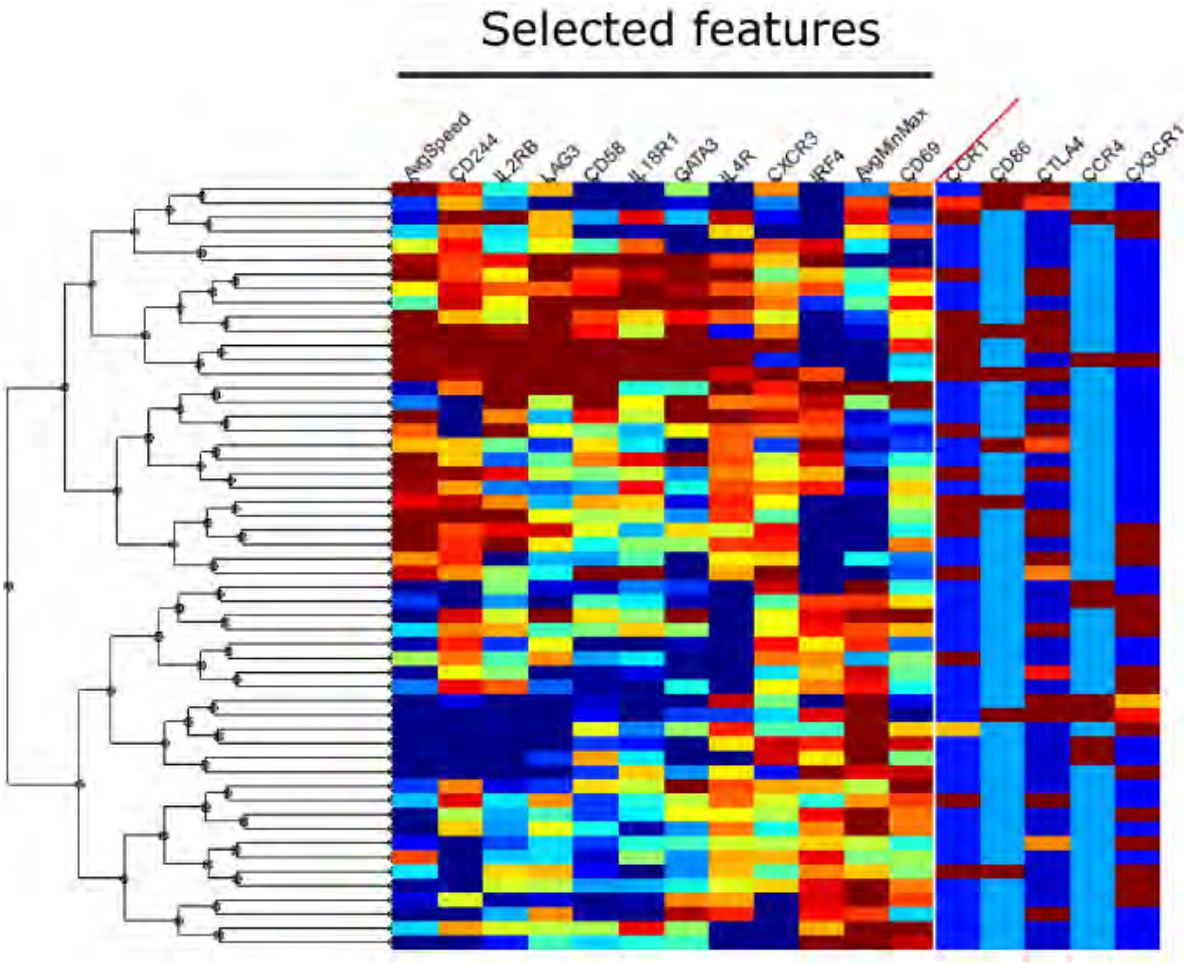

Figure 77: Trend discovery with STrenD allows selecting the genes that are the most relevant for description of the progressive states between cells

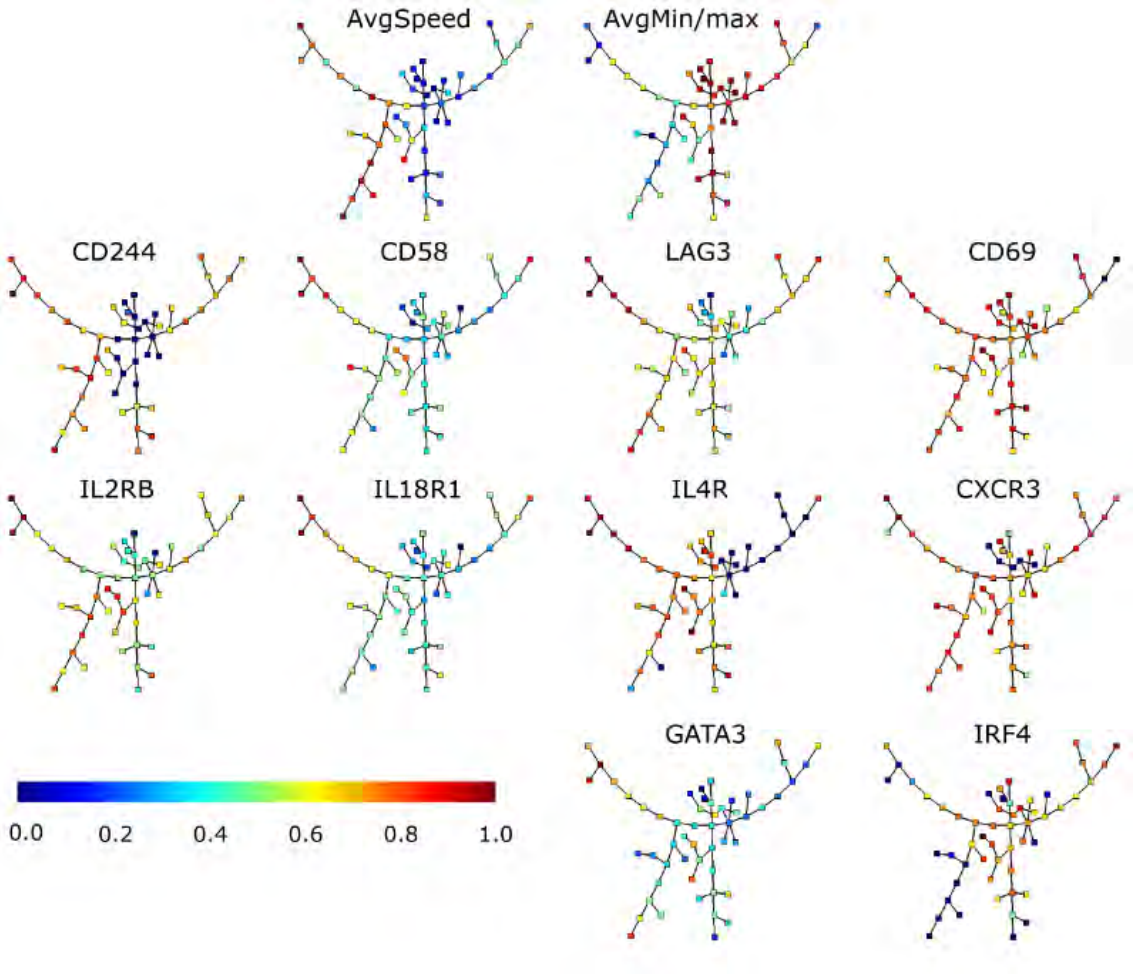

Figure 78: Visualization of the consecutives states in a tree shape structure illustrating how each gene localizes differentially with high or low motility cells.

Consistent with the observations outlined here, network analysis using GeneMania (125) confirmed that the major pathways associated with the identified transcripts were related to positive T-cell activation and lymphocyte migration (**Figure 79**).

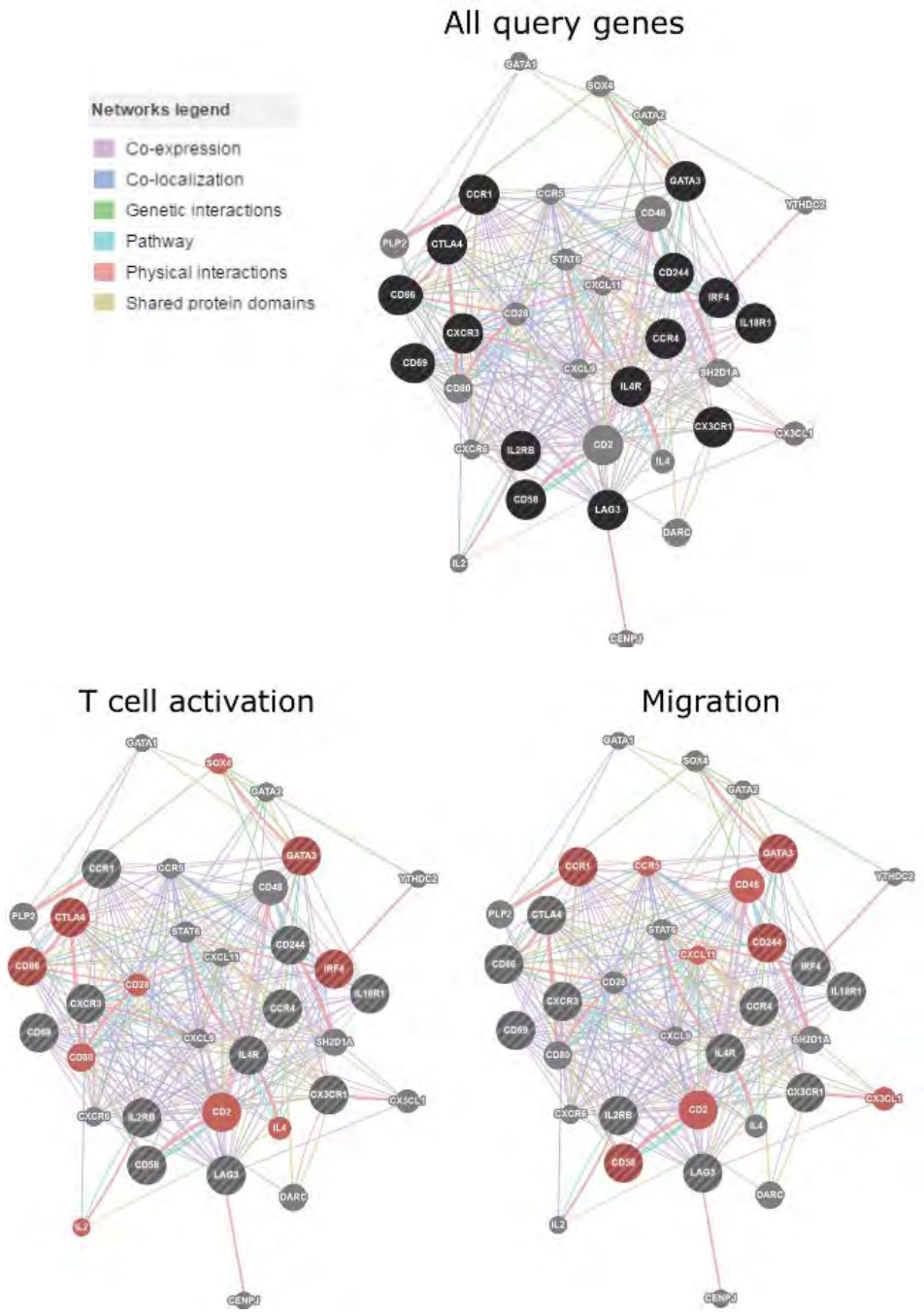

Figure 79: Protein interaction network analysis using Genemania of differentially expressed genes demonstrating their segregation into T-cell activation and cell migration pathways

Lastly, since one of the major mechanisms of immediate cytotoxicity mediated by $CD8^+$ T cells is through the granzyme B/ Perforin pathway, and since our TIMING results indicated that polyfunctional serial killer $CD8^+$ T cells had a higher basal motility, we

quantified the differences in expression of these specific transcripts within motile and non-motile cells. Although *GZMB* was not significantly differentially expressed, *PRF1* transcripts were detected at significantly higher levels in motile cells (p-value = 0.03, **Figure 80**).

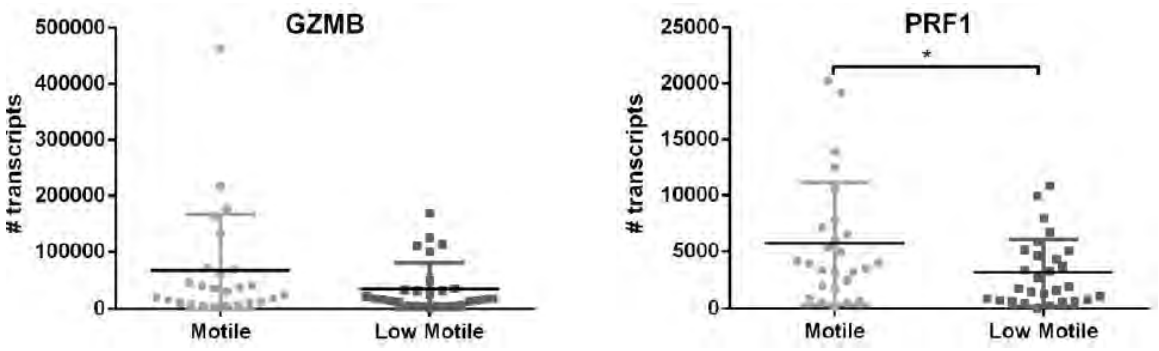

Figure 80: Comparisons of relative number of Granzyme B and perforin transcripts in high and low motility $CD8^+$ T cells.

3.4. DISCUSSION

We have demonstrated an integrated and modular high-throughput analytical pipeline for combined functional and molecular profiling of T-cell behaviors. This single-cell assay provides an integrated method which not only tracks the key functional attributes of T cells including motility, cytotoxicity, and cytokine secretion directly, but also serves as a front-end screen for identifying functional attributes that can be interrogated at the molecular level using multiplexed transcriptional profiling. Although we have demonstrated the application of this method in the context of T-cell behaviors, the platform can be adapted to other cell types for monitoring combined cellular behaviors, protein secretion, and transcriptional profiling.

The polyfunctionality of tumor-specific individual $CD8^+$ CAR^+ T cells, with regards to IFN-γ secretion and killing (and multi-killing) upon ligation with tumor cells was evaluated. Among all functional T cells, the group that secreted IFN-γ as a monofunction displayed the longest duration of conjugation to the tumor cell, in comparison to the T cells that participated in lysis of target cells. Since all T cells were uniformly modified with the CAR, and since the concentration of antigen on the target cells was uniform (**Figure 16**), our results reveal that the duration of stable conjugation leading to different functional outcomes (IFN-γ *vs*. killing) can be heterogeneous. Our results thus complement previous studies obtained by titrating antigen concentration to show that $CD8^+$ T cells can form a short lytic synapse at low antigen densities, and a long stable stimulatory synapse leading to IFN-γ at high antigen densities (126, 127). Significantly, our results at the single-cell level suggest that detachment from target cells might be enabled by killing, and the decision to terminate conjugation can occur prior to Annexin V staining (**Figure 66-67**). In tracking the frequencies of serial killer T cells with and without simultaneous IFN-γ secretion, no significant differences were observed, suggesting that the early termination of conjugation did not affect T-cell activation for IFN-γ secretion. Our results demonstrating at the single-cell level that the duration of conjugation of T cells to target cells might reflect different functional outcomes are in concordance with a recent report combining population level functional studies and single-cell calcium activation on mouse/human T cells which showed that failed target detachment can lead to prolonged IFN-γ hyper-secretion from T cells and that initiation of caspase within target cells likely enabled T cells to terminate the synapse (128).

In addition, tracking the displacement of $CD8^+CAR^+$ T cells revealed that polyfunctional cells and specifically serial killer T cells, exhibited elevated out-of-contact basal motility in comparison to either non-functional T cells, or those effector cells that only secreted IFN-γ. In order to gain molecular insights into the immunological state of highly motile cells, multiplexed transcriptional profiling was performed at the single-cell level, targeting genes associated with T-cell activation, differentiation and memory. Combined statistical testing using t tests and hierarchical clustering followed by progression discovery modeling identified a core set of immunological genes that may be useful in distinguishing motile and non-motile T cells. Consistent with TIMING observations that motile T cells are enriched within the polyfunctional subset, molecular profiling indicated that markers associated with recent activation including *CD244 (2B4), CD58, LAG3, IL2RB (CD122), IL18R1*, the chemokine receptor *CXCR3* and the transcription factor *GATA3* were upregulated within motile cells. Similarly, the transcripts for the pore forming protein, perforin, required for immediate cytotoxicity mediated by $CD8^+$ T cells, were also upregulated within motile T cells (**Figure 80**).

Individual T cells with increased motility also showed a matched increase in *CXCR3* transcripts (**Figure 81**) which is one of the major chemokine receptors associated with trafficking to the tumor microenvironment and is expressed on activated TILs in diverse cancers including breast cancer and melanoma (129, 130).

The expression of *CXCR3* is up-regulated upon $CD8^+$ T-cell activation, and in addition to its functional role in chemotaxis, *CXCR3* derived signaling is believed to also affect the development of both effector and memory $CD8^+$ T cells (131-133). Similarly,

the number of *CD2* transcripts showed a positive correlation with T-cell motility (**Figure 82**).

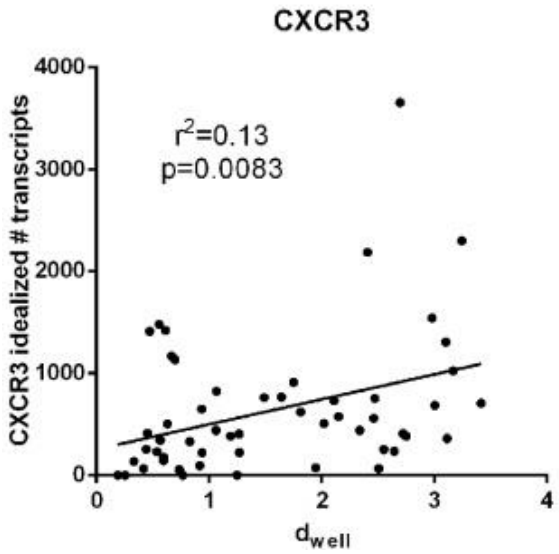

Figure 81: Correlation between idealized numbers of CXCR3 transcripts and average speed of the cell (d_{well})

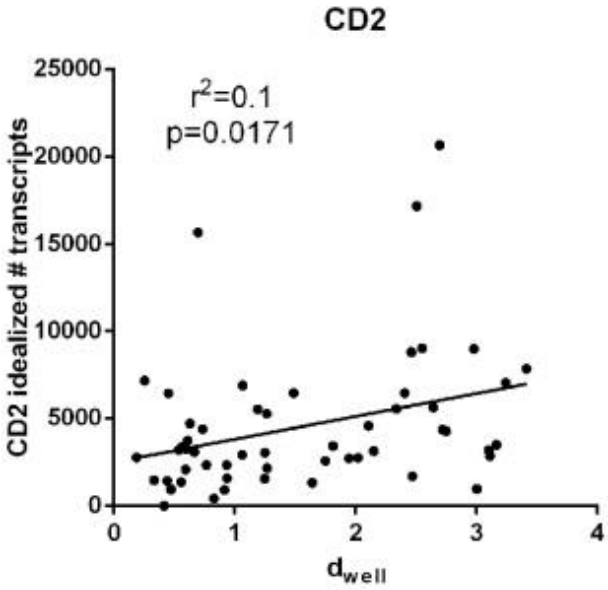

Figure 82: Correlation between idealized numbers of CD2 transcripts and average speed of the cell (d_{well})

The dynamic molecular interaction between CD2 and its binding partner CD58 facilitates T-cell recognition by stabilization of inter-cell contacts (134, 135). Since the single-cell transcriptional profiling indicated a matched up-regulation of *CD58* and *CD2* on motile T cells (**Figure 83**), it is possible that these molecules can mediate homotypic T-cell/T-cell interactions and cluster formation, both of which are known to promote T-cell activation, proliferation and differentiation *in vitro* and *in vivo* (136). Of note, *CD244* was also upregulated on motile T cells and is a similar adhesion molecule that can regulate T-cell homotypic interactions by binding to CD48 (**Figure 84**). We thus propose an integrated model that summarizes all of our results integrating motility, serial killing, IFN-γ secretion and transcriptional profiling (**Figure 85**).

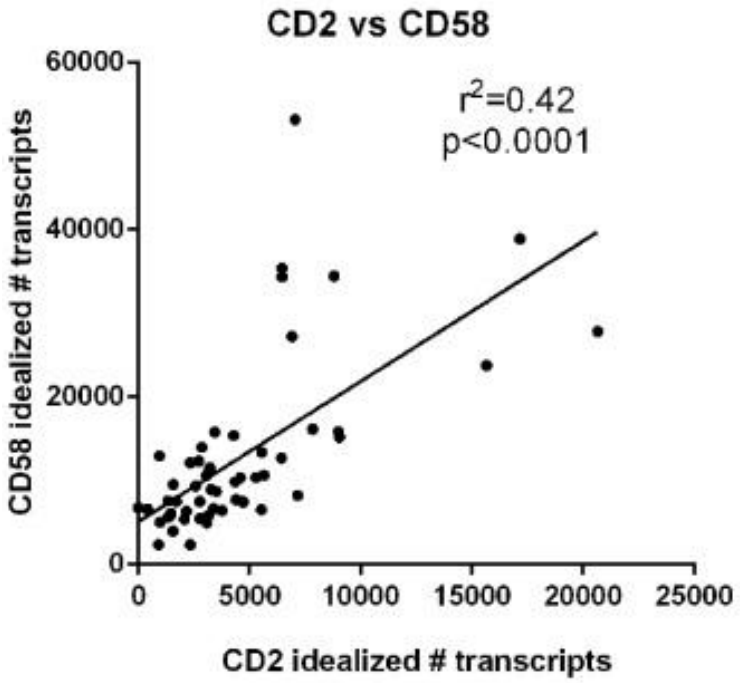

Figure 83: CD2 and CD58 expression are linearly correlated at the single-cell level.

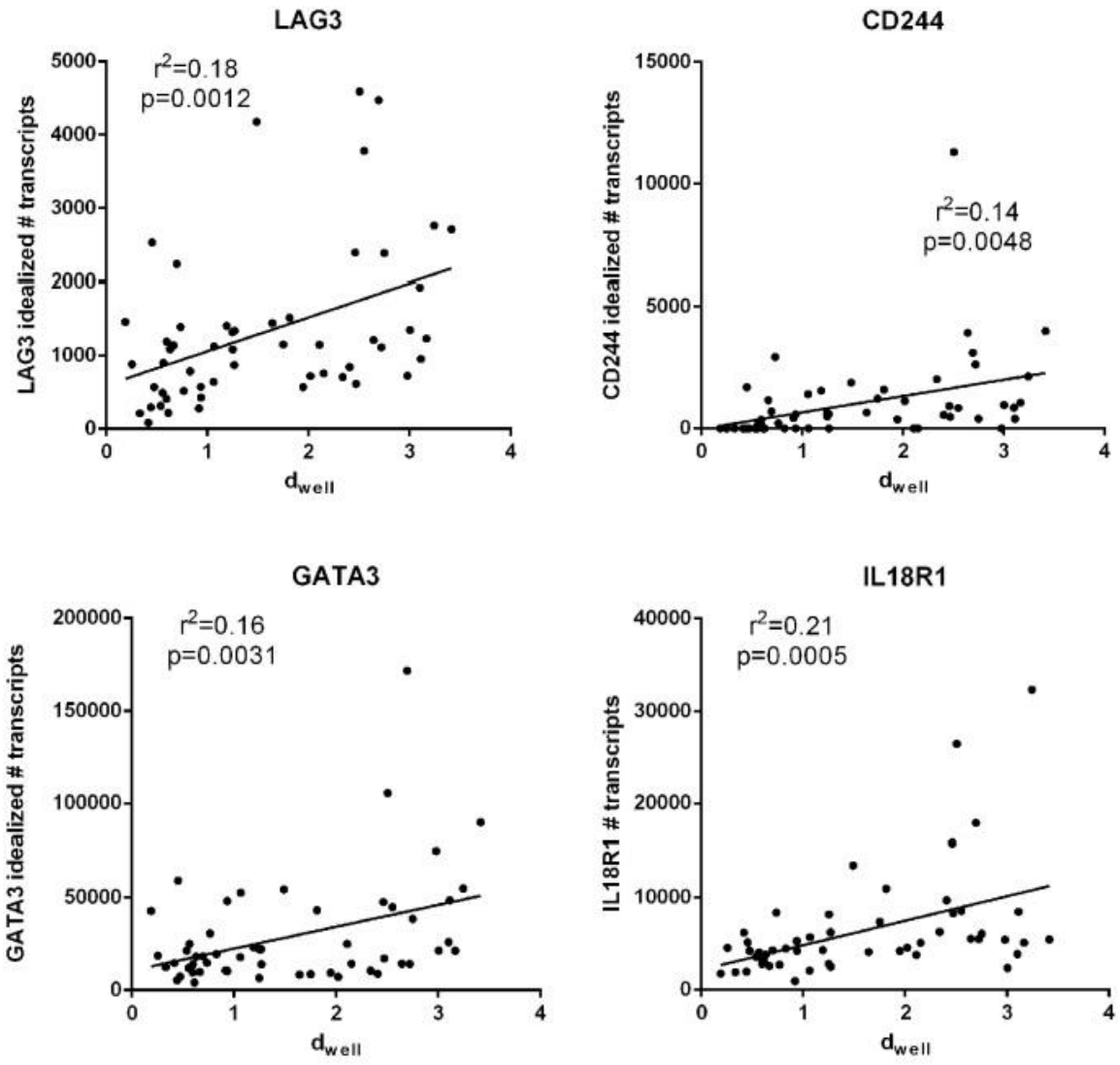

Figure 84: LAG3, CD244 (2B4), GATA3 and IL18R1 transcripts are more highly expressed in high motility in comparison to low motility cells.

In summary, our integrated methodology combining functional and molecular screening enables investigation of complex cellular behaviors at single-cell resolution. Our modular and scalable method is suitable for screening combinations of the different T cell functions that might be required for the efficacy of T cells engineered with a panel of CARs and predicting whether an introduced immunoreceptor will result in therapeutic success in vivo (137).

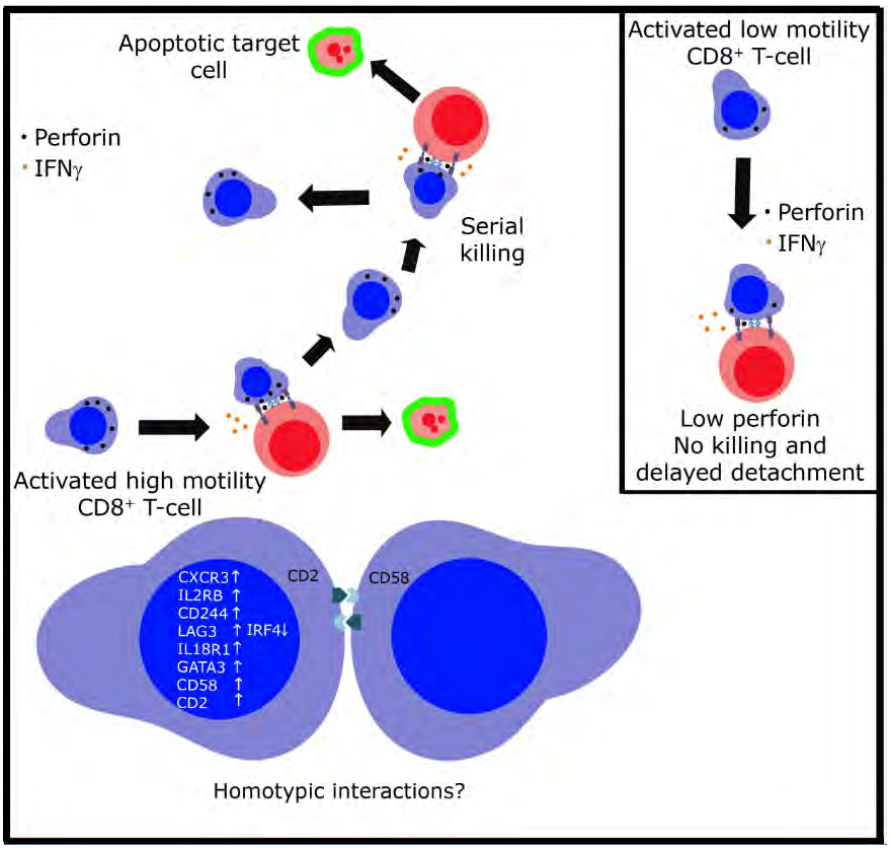

Figure 85: Schematic summarizing integrated T-cell functionality

The therapeutic potential of CAR$^+$ T cells for treatment of B-cell malignancies raises the question whether similarly-engineered T cells with alternative specificities will also have anti-tumor effects in humans. Thus, the study of genetically modified CD19-specific T cells serves as a foundation to advance our understanding of CAR$^+$ T cells that target other hematologic malignancies and solid tumors. Currently, most investigators rely on mouse experiments to inform on which CAR design and TIL population to advance to human application, but this is not readily amenable to scale up. As demonstrated here, we propose that high throughput *in vitro* systems can be employed to evaluate the functional characteristics of panels of T cells before selecting subsets for preclinical and clinical translation. The implementation of the microscopy tools revealed in this report and the observation that motility correlates with killing of tumor cells may provide investigators

with an approach to identify genetically modified T cells without the need for testing in small animals.

REFERENCES

1. Wilde, S., D. Sommermeyer, M. Leisegang, B. Frankenberger, B. Mosetter, W. Uckert, and D. J. Schendel. 2012. Human antitumor CD8+ T cells producing Th1 polycytokines show superior antigen sensitivity and tumor recognition. *J Immunol* 189: 598-605.
2. CDC. 2015. Data and statistics. *www.cdc.gov.*
3. Medicine, N. L. o. 2015. Drugs, herbs, and supplements. *www.nlm.nih.gov.*
4. Robak, T. 2005. Therapy of chronic lymphocytic leukemia with purine analogs and monoclonal antibodies. *Transfusion and apheresis science : official journal of the World Apheresis Association : official journal of the European Society for Haemapheresis* 32: 33-44.
5. Robak, T., A. Dmoszynska, P. Solal-Celigny, K. Warzocha, J. Loscertales, J. Catalano, B. V. Afanasiev, L. Larratt, C. H. Geisler, M. Montillo, I. Zyuzgin, P. S. Ganly, C. Dartigeas, A. Rosta, J. Maurer, M. Mendila, M. W. Saville, N. Valente, M. K. Wenger, and S. I. Moiseev. 2010. Rituximab plus fludarabine and cyclophosphamide prolongs progression-free survival compared with fludarabine and cyclophosphamide alone in previously treated chronic lymphocytic leukemia. *J Clin Oncol* 28: 1756-1765.
6. WebMD. 2015. Chemotherapy. *www.webmd.com.*
7. Kantoff, P. W., C. S. Higano, N. D. Shore, E. R. Berger, E. J. Small, D. F. Penson, C. H. Redfern, A. C. Ferrari, R. Dreicer, R. B. Sims, Y. Xu, M. W. Frohlich, P. F. Schellhammer, and I. S. Investigators. 2010. Sipuleucel-T immunotherapy for castration-resistant prostate cancer. *N Engl J Med* 363: 411-422.

8. Levy, Y., R. Thiebaut, M. Montes, C. Lacabaratz, L. Sloan, B. King, S. Perusat, C. Harrod, A. Cobb, L. K. Roberts, M. Surenaud, C. Boucherie, S. Zurawski, C. Delaugerre, L. Richert, G. Chene, J. Banchereau, and K. Palucka. 2014. Dendritic cell-based therapeutic vaccine elicits polyfunctional HIV-specific T-cell immunity associated with control of viral load. *Eur J Immunol* 44: 2802-2810.

9. Precopio, M. L., M. R. Betts, J. Parrino, D. A. Price, E. Gostick, D. R. Ambrozak, T. E. Asher, D. C. Douek, A. Harari, G. Pantaleo, R. Bailer, B. S. Graham, M. Roederer, and R. A. Koup. 2007. Immunization with vaccinia virus induces polyfunctional and phenotypically distinctive CD8(+) T cell responses. *J Exp Med* 204: 1405-1416.

10. Akondy, R. S., N. D. Monson, J. D. Miller, S. Edupuganti, D. Teuwen, H. Wu, F. Quyyumi, S. Garg, J. D. Altman, C. Del Rio, H. L. Keyserling, A. Ploss, C. M. Rice, W. A. Orenstein, M. J. Mulligan, and R. Ahmed. 2009. The yellow fever virus vaccine induces a broad and polyfunctional human memory CD8+ T cell response. *J Immunol* 183: 7919-7930.

11. Gaucher, D., R. Therrien, N. Kettaf, B. R. Angermann, G. Boucher, A. Filali-Mouhim, J. M. Moser, R. S. Mehta, D. R. Drake, 3rd, E. Castro, R. Akondy, A. Rinfret, B. Yassine-Diab, E. A. Said, Y. Chouikh, M. J. Cameron, R. Clum, D. Kelvin, R. Somogyi, L. D. Greller, R. S. Balderas, P. Wilkinson, G. Pantaleo, J. Tartaglia, E. K. Haddad, and R. P. Sekaly. 2008. Yellow fever vaccine induces integrated multilineage and polyfunctional immune responses. *J Exp Med* 205: 3119-3131.

12. Fellner, C. 2012. Ipilimumab (yervoy) prolongs survival in advanced melanoma: serious side effects and a hefty price tag may limit its use. *P & T : a peer-reviewed journal for formulary management* 37: 503-530.

13. Graziani, G., L. Tentori, and P. Navarra. 2012. Ipilimumab: a novel immunostimulatory monoclonal antibody for the treatment of cancer. *Pharmacological research : the official journal of the Italian Pharmacological Society* 65: 9-22.

14. Pardoll, D. M. 2012. The blockade of immune checkpoints in cancer immunotherapy. *Nature reviews. Cancer* 12: 252-264.

15. Andtbacka, R. H., M. R. Donaldson, T. L. Bowles, G. M. Bowen, K. Grossmann, H. Khong, D. Grossman, C. Anker, S. R. Florell, A. Bowen, K. L. Duffy, S. A. Leachman, and R. D. Noyes. 2013. Sentinel lymph node biopsy for melanoma in pregnant women. *Annals of surgical oncology* 20: 689-696.

16. Russell, S. J., M. J. Federspiel, K. W. Peng, C. Tong, D. Dingli, W. G. Morice, V. Lowe, M. K. O'Connor, R. A. Kyle, N. Leung, F. K. Buadi, S. V. Rajkumar, M. A. Gertz, M. Q. Lacy, and A. Dispenzieri. 2014. Remission of disseminated cancer after systemic oncolytic virotherapy. *Mayo Clinic proceedings* 89: 926-933.

17. Drake, J. M., J. K. Lee, and O. N. Witte. 2014. Clinical targeting of mutated and wild-type protein tyrosine kinases in cancer. *Molecular and cellular biology* 34: 1722-1732.

18. Tiseo, M., M. Bartolotti, F. Gelsomino, and P. Bordi. 2010. Emerging role of gefitinib in the treatment of non-small-cell lung cancer (NSCLC). *Drug design, development and therapy* 4: 81-98.

19. Togashi, Y., H. Hayashi, K. Nakagawa, and K. Nishio. 2014. Clinical utility of erlotinib for the treatment of non-small-cell lung cancer in Japanese patients: current evidence. *Drug design, development and therapy* 8: 1037-1046.

20. Hinrichs, C. S., and S. A. Rosenberg. 2014. Exploiting the curative potential of adoptive T-cell therapy for cancer. *Immunol Rev* 257: 56-71.

21. Restifo, N. P., M. E. Dudley, and S. A. Rosenberg. 2012. Adoptive immunotherapy for cancer: harnessing the T cell response. *Nat Rev Immunol* 12: 269-281.

22. June, C. H., S. R. Riddell, and T. N. Schumacher. 2015. Adoptive cellular therapy: a race to the finish line. *Sci Transl Med* 7: 280ps287.

23. Listopad, J. J., T. Kammertoens, K. Anders, B. Silkenstedt, G. Willimsky, K. Schmidt, A. A. Kuehl, C. Loddenkemper, and T. Blankenstein. 2013. Fas expression by tumor stroma is required for cancer eradication. *Proc Natl Acad Sci U S A* 110: 2276-2281.

24. Prevost-Blondel, A., M. Neuenhahn, M. Rawiel, and H. Pircher. 2000. Differential requirement of perforin and IFN-gamma in CD8 T cell-mediated immune responses against B16.F10 melanoma cells expressing a viral antigen. *Eur J Immunol* 30: 2507-2515.

25. Becker, C., H. Pohla, B. Frankenberger, T. Schuler, M. Assenmacher, D. J. Schendel, and T. Blankenstein. 2001. Adoptive tumor therapy with T lymphocytes enriched through an IFN-gamma capture assay. *Nat Med* 7: 1159-1162.

26. Matsushita, H., A. Hosoi, S. Ueha, J. Abe, N. Fujieda, M. Tomura, R. Maekawa, K. Matsushima, O. Ohara, and K. Kakimi. 2015. Cytotoxic T Lymphocytes Block

Tumor Growth Both by Lytic Activity and IFNgamma-Dependent Cell-Cycle Arrest. *Cancer Immunol Res* 3: 26-36.

27. Slaney, C. Y., M. H. Kershaw, and P. K. Darcy. 2014. Trafficking of T cells into tumors. *Cancer Res* 74: 7168-7174.

28. Yu, J., J. Zhou, A. Sutherland, W. Wei, Y. S. Shin, M. Xue, and J. R. Heath. 2014. Microfluidics-based single-cell functional proteomics for fundamental and applied biomedical applications. *Annu Rev Anal Chem (Palo Alto Calif)* 7: 275-295.

29. Love, J. C., J. L. Ronan, G. M. Grotenbreg, A. G. van der Veen, and H. L. Ploegh. 2006. A microengraving method for rapid selection of single cells producing antigen-specific antibodies. *Nature biotechnology* 24: 703-707.

30. Ogunniyi, A. O., C. M. Story, E. Papa, E. Guillen, and J. C. Love. 2009. Screening individual hybridomas by microengraving to discover monoclonal antibodies. *Nature protocols* 4: 767-782.

31. Varadarajan, N., D. S. Kwon, K. M. Law, A. O. Ogunniyi, M. N. Anahtar, J. M. Richter, B. D. Walker, and J. C. Love. 2012. Rapid, efficient functional characterization and recovery of HIV-specific human CD8+ T cells using microengraving. *Proc Natl Acad Sci U S A* 109: 3885-3890.

32. Han, Q., N. Bagheri, E. M. Bradshaw, D. A. Hafler, D. A. Lauffenburger, and J. C. Love. 2012. Polyfunctional responses by human T cells result from sequential release of cytokines. *Proc Natl Acad Sci U S A* 109: 1607-1612.

33. Ma, C., R. Fan, H. Ahmad, Q. Shi, B. Comin-Anduix, T. Chodon, R. C. Koya, C. C. Liu, G. A. Kwong, C. G. Radu, A. Ribas, and J. R. Heath. 2011. A clinical

microchip for evaluation of single immune cells reveals high functional heterogeneity in phenotypically similar T cells. *Nat Med* 17: 738-743.

34. Shi, Q., L. Qin, W. Wei, F. Geng, R. Fan, Y. S. Shin, D. Guo, L. Hood, P. S. Mischel, and J. R. Heath. 2012. Single-cell proteomic chip for profiling intracellular signaling pathways in single tumor cells. *Proc Natl Acad Sci U S A* 109: 419-424.

35. Wei, W., Y. S. Shin, C. Ma, J. Wang, M. Elitas, R. Fan, and J. R. Heath. 2013. Microchip platforms for multiplex single-cell functional proteomics with applications to immunology and cancer research. *Genome medicine* 5: 75.

36. Wang, J., D. Tham, W. Wei, Y. S. Shin, C. Ma, H. Ahmad, Q. Shi, J. Yu, R. D. Levine, and J. R. Heath. 2012. Quantitating cell-cell interaction functions with applications to glioblastoma multiforme cancer cells. *Nano letters* 12: 6101-6106.

37. Lu, Y., Q. Xue, M. R. Eisele, E. S. Sulistijo, K. Brower, L. Han, A. D. Amir el, D. Pe'er, K. Miller-Jensen, and R. Fan. 2015. Highly multiplexed profiling of single-cell effector functions reveals deep functional heterogeneity in response to pathogenic ligands. *Proc Natl Acad Sci U S A* 112: E607-615.

38. Herderschee, J., C. Fenwick, G. Pantaleo, T. Roger, and T. Calandra. 2015. Emerging single-cell technologies in immunology. *Journal of leukocyte biology*.

39. Bendall, S. C., E. F. Simonds, P. Qiu, A. D. Amir el, P. O. Krutzik, R. Finck, R. V. Bruggner, R. Melamed, A. Trejo, O. I. Ornatsky, R. S. Balderas, S. K. Plevritis, K. Sachs, D. Pe'er, S. D. Tanner, and G. P. Nolan. 2011. Single-cell mass cytometry of differential immune and drug responses across a human hematopoietic continuum. *Science* 332: 687-696.

40. Bodenmiller, B., E. R. Zunder, R. Finck, T. J. Chen, E. S. Savig, R. V. Bruggner, E. F. Simonds, S. C. Bendall, K. Sachs, P. O. Krutzik, and G. P. Nolan. 2012. Multiplexed mass cytometry profiling of cellular states perturbed by small-molecule regulators. *Nature biotechnology* 30: 858-867.

41. Konry, T., A. Golberg, and M. Yarmush. 2013. Live single cell functional phenotyping in droplet nano-liter reactors. *Scientific reports* 3: 3179.

42. Chokkalingam, V., J. Tel, F. Wimmers, X. Liu, S. Semenov, J. Thiele, C. G. Figdor, and W. T. Huck. 2013. Probing cellular heterogeneity in cytokine-secreting immune cells using droplet-based microfluidics. *Lab Chip* 13: 4740-4744.

43. Tuleuova, N., and A. Revzin. 2010. Micropatterning of Aptamer Beacons to Create Cytokine-Sensing Surfaces. *Cellular and molecular bioengineering* 3: 337-344.

44. Tuleuova, N., C. N. Jones, J. Yan, E. Ramanculov, Y. Yokobayashi, and A. Revzin. 2010. Development of an aptamer beacon for detection of interferon-gamma. *Anal Chem* 82: 1851-1857.

45. Raphael, M. P., J. A. Christodoulides, J. B. Delehanty, J. P. Long, and J. M. Byers. 2013. Quantitative imaging of protein secretions from single cells in real time. *Biophysical journal* 105: 602-608.

46. Raphael, M. P., J. A. Christodoulides, J. B. Delehanty, J. P. Long, P. E. Pehrsson, and J. M. Byers. 2013. Quantitative LSPR imaging for biosensing with single nanostructure resolution. *Biophysical journal* 104: 30-36.

47. Fan, H. C., G. K. Fu, and S. P. Fodor. 2015. Expression profiling. Combinatorial labeling of single cells for gene expression cytometry. *Science* 347: 1258367.

48. Flatz, L., R. Roychoudhuri, M. Honda, A. Filali-Mouhim, J. P. Goulet, N. Kettaf, M. Lin, M. Roederer, E. K. Haddad, R. P. Sekaly, and G. J. Nabel. 2011. Single-cell gene-expression profiling reveals qualitatively distinct CD8 T cells elicited by different gene-based vaccines. *Proc Natl Acad Sci U S A* 108: 5724-5729.

49. Shalek, A. K., R. Satija, J. Shuga, J. J. Trombetta, D. Gennert, D. Lu, P. Chen, R. S. Gertner, J. T. Gaublomme, N. Yosef, S. Schwartz, B. Fowler, S. Weaver, J. Wang, X. Wang, R. Ding, R. Raychowdhury, N. Friedman, N. Hacohen, H. Park, A. P. May, and A. Regev. 2014. Single-cell RNA-seq reveals dynamic paracrine control of cellular variation. *Nature* 510: 363-369.

50. Varadarajan, N., B. Julg, Y. J. Yamanaka, H. Chen, A. O. Ogunniyi, E. McAndrew, L. C. Porter, A. Piechocka-Trocha, B. J. Hill, D. C. Douek, F. Pereyra, B. D. Walker, and J. C. Love. 2011. A high-throughput single-cell analysis of human CD8(+) T cell functions reveals discordance for cytokine secretion and cytolysis. *J Clin Invest* 121: 4322-4331.

51. Khorshidi, M. A., B. Vanherberghen, J. M. Kowalewski, K. R. Garrod, S. Lindstrom, H. Andersson-Svahn, H. Brismar, M. D. Cahalan, and B. Onfelt. 2011. Analysis of transient migration behavior of natural killer cells imaged in situ and in vitro. *Integr Biol (Camb)* 3: 770-778.

52. Forslund, E., K. Guldevall, P. E. Olofsson, T. Frisk, A. E. Christakou, M. Wiklund, and B. Onfelt. 2012. Novel Microchip-Based Tools Facilitating Live Cell Imaging and Assessment of Functional Heterogeneity within NK Cell Populations. *Frontiers in immunology* 3: 300.

53. Vanherberghen, B., P. E. Olofsson, E. Forslund, M. Sternberg-Simon, M. A. Khorshidi, S. Pacouret, K. Guldevall, M. Enqvist, K. J. Malmberg, R. Mehr, and B. Onfelt. 2013. Classification of human natural killer cells based on migration behavior and cytotoxic response. *Blood* 121: 1326-1334.

54. Sackmann, E. K., E. Berthier, E. A. Schwantes, P. S. Fichtinger, M. D. Evans, L. L. Dziadzio, A. Huttenlocher, S. K. Mathur, and D. J. Beebe. 2014. Characterizing asthma from a drop of blood using neutrophil chemotaxis. *Proc Natl Acad Sci U S A* 111: 5813-5818.

55. Abonnenc, M., M. Borgatti, E. Fabbri, R. Gavioli, C. Fortini, F. Destro, L. Altomare, N. Manaresi, G. Medoro, A. Romani, M. Tartagni, E. Lo Monaco, P. Giacomini, R. Guerrieri, and R. Gambari. 2013. Lysis-on-chip of single target cells following forced interaction with CTLs or NK cells on a dielectrophoresis-based array. *J Immunol* 191: 3545-3552.

56. Zaretsky, I., M. Polonsky, E. Shifrut, S. Reich-Zeliger, Y. Antebi, G. Aidelberg, N. Waysbort, and N. Friedman. 2012. Monitoring the dynamics of primary T cell activation and differentiation using long term live cell imaging in microwell arrays. *Lab Chip* 12: 5007-5015.

57. Dura, B., S. K. Dougan, M. Barisa, M. M. Hoehl, C. T. Lo, H. L. Ploegh, and J. Voldman. 2015. Profiling lymphocyte interactions at the single-cell level by microfluidic cell pairing. *Nature communications* 6: 5940.

58. Kalos, M., and C. H. June. 2013. Adoptive T cell transfer for cancer immunotherapy in the era of synthetic biology. *Immunity* 39: 49-60.

59. Sadelain, M., R. Brentjens, and I. Riviere. 2013. The basic principles of chimeric antigen receptor design. *Cancer Discov* 3: 388-398.

60. Dotti, G., S. Gottschalk, B. Savoldo, and M. K. Brenner. 2014. Design and development of therapies using chimeric antigen receptor-expressing T cells. *Immunol Rev* 257: 107-126.

61. Kochenderfer, J. N., and S. A. Rosenberg. 2013. Treating B-cell cancer with T cells expressing anti-CD19 chimeric antigen receptors. *Nat Rev Clin Oncol* 10: 267-276.

62. Brentjens, R. J., M. L. Davila, I. Riviere, J. Park, X. Wang, L. G. Cowell, S. Bartido, J. Stefanski, C. Taylor, M. Olszewska, O. Borquez-Ojeda, J. Qu, T. Wasielewska, Q. He, Y. Bernal, I. V. Rijo, C. Hedvat, R. Kobos, K. Curran, P. Steinherz, J. Jurcic, T. Rosenblat, P. Maslak, M. Frattini, and M. Sadelain. 2013. CD19-targeted T cells rapidly induce molecular remissions in adults with chemotherapy-refractory acute lymphoblastic leukemia. *Sci Transl Med* 5: 177ra138.

63. Grupp, S. A., M. Kalos, D. Barrett, R. Aplenc, D. L. Porter, S. R. Rheingold, D. T. Teachey, A. Chew, B. Hauck, J. F. Wright, M. C. Milone, B. L. Levine, and C. H. June. 2013. Chimeric antigen receptor-modified T cells for acute lymphoid leukemia. *N Engl J Med* 368: 1509-1518.

64. Jena, B., G. Dotti, and L. J. Cooper. 2010. Redirecting T-cell specificity by introducing a tumor-specific chimeric antigen receptor. *Blood* 116: 1035-1044.

65. Spear, P., A. Barber, and C. L. Sentman. 2013. Collaboration of chimeric antigen receptor (CAR)-expressing T cells and host T cells for optimal elimination of established ovarian tumors. *Oncoimmunology* 2: e23564.

66. Morgan, R. A., L. A. Johnson, J. L. Davis, Z. Zheng, K. D. Woolard, E. A. Reap, S. A. Feldman, N. Chinnasamy, C. T. Kuan, H. Song, W. Zhang, H. A. Fine, and S. A. Rosenberg. 2012. Recognition of glioma stem cells by genetically modified T cells targeting EGFRvIII and development of adoptive cell therapy for glioma. *Hum Gene Ther* 23: 1043-1053.

67. Louis, C. U., B. Savoldo, G. Dotti, M. Pule, E. Yvon, G. D. Myers, C. Rossig, H. V. Russell, O. Diouf, E. Liu, H. Liu, M. F. Wu, A. P. Gee, Z. Mei, C. M. Rooney, H. E. Heslop, and M. K. Brenner. 2011. Antitumor activity and long-term fate of chimeric antigen receptor-positive T cells in patients with neuroblastoma. *Blood* 118: 6050-6056.

68. Kalos, M., B. L. Levine, D. L. Porter, S. Katz, S. A. Grupp, A. Bagg, and C. H. June. 2011. T cells with chimeric antigen receptors have potent antitumor effects and can establish memory in patients with advanced leukemia. *Sci Transl Med* 3: 95ra73.

69. Dudley, M. E., J. C. Yang, R. Sherry, M. S. Hughes, R. Royal, U. Kammula, P. F. Robbins, J. Huang, D. E. Citrin, S. F. Leitman, J. Wunderlich, N. P. Restifo, A. Thomasian, S. G. Downey, F. O. Smith, J. Klapper, K. Morton, C. Laurencot, D. E. White, and S. A. Rosenberg. 2008. Adoptive cell therapy for patients with metastatic melanoma: evaluation of intensive myeloablative chemoradiation preparative regimens. *J Clin Oncol* 26: 5233-5239.

70. Janssen, E. M., E. E. Lemmens, T. Wolfe, U. Christen, M. G. von Herrath, and S. P. Schoenberger. 2003. CD4+ T cells are required for secondary expansion and memory in CD8+ T lymphocytes. *Nature* 421: 852-856.

71. Antony, P. A., C. A. Piccirillo, A. Akpinarli, S. E. Finkelstein, P. J. Speiss, D. R. Surman, D. C. Palmer, C. C. Chan, C. A. Klebanoff, W. W. Overwijk, S. A. Rosenberg, and N. P. Restifo. 2005. CD8+ T cell immunity against a tumor/self-antigen is augmented by CD4+ T helper cells and hindered by naturally occurring T regulatory cells. *J Immunol* 174: 2591-2601.

72. Dudley, M. E., J. R. Wunderlich, P. F. Robbins, J. C. Yang, P. Hwu, D. J. Schwartzentruber, S. L. Topalian, R. Sherry, N. P. Restifo, A. M. Hubicki, M. R. Robinson, M. Raffeld, P. Duray, C. A. Seipp, L. Rogers-Freezer, K. E. Morton, S. A. Mavroukakis, D. E. White, and S. A. Rosenberg. 2002. Cancer regression and autoimmunity in patients after clonal repopulation with antitumor lymphocytes. *Science* 298: 850-854.

73. Hunder, N. N., H. Wallen, J. Cao, D. W. Hendricks, J. Z. Reilly, R. Rodmyre, A. Jungbluth, S. Gnjatic, J. A. Thompson, and C. Yee. 2008. Treatment of metastatic melanoma with autologous CD4+ T cells against NY-ESO-1. *N Engl J Med* 358: 2698-2703.

74. Quezada, S. A., T. R. Simpson, K. S. Peggs, T. Merghoub, J. Vider, X. Fan, R. Blasberg, H. Yagita, P. Muranski, P. A. Antony, N. P. Restifo, and J. P. Allison. 2010. Tumor-reactive CD4(+) T cells develop cytotoxic activity and eradicate large established melanoma after transfer into lymphopenic hosts. *J Exp Med* 207: 637-650.

75. Xie, Y., A. Akpinarli, C. Maris, E. L. Hipkiss, M. Lane, E. K. Kwon, P. Muranski, N. P. Restifo, and P. A. Antony. 2010. Naive tumor-specific CD4(+) T cells differentiated in vivo eradicate established melanoma. *J Exp Med* 207: 651-667.

76. Roach, K. L., K. R. King, B. E. Uygun, I. S. Kohane, M. L. Yarmush, and M. Toner. 2009. High throughput single cell bioinformatics. *Biotechnol Prog* 25: 1772-1779.

77. Deutsch, M., A. Deutsch, O. Shirihai, I. Hurevich, E. Afrimzon, Y. Shafran, and N. Zurgil. 2006. A novel miniature cell retainer for correlative high-content analysis of individual untethered non-adherent cells. *Lab Chip* 6: 995-1000.

78. Liadi, I., J. Roszik, G. Romain, L. J. Cooper, and N. Varadarajan. 2013. Quantitative high-throughput single-cell cytotoxicity assay for T cells. *J Vis Exp*: e50058.

79. Yamanaka, Y. J., C. T. Berger, M. Sips, P. C. Cheney, G. Alter, and J. C. Love. 2012. Single-cell analysis of the dynamics and functional outcomes of interactions between human natural killer cells and target cells. *Integr Biol (Camb)* 4: 1175-1184.

80. Romain, G., V. Senyukov, N. Rey-Villamizar, A. Merouane, W. Kelton, I. Liadi, A. Mahendra, W. Charab, G. Georgiou, B. Roysam, D. A. Lee, and N. Varadarajan. 2014. Antibody Fc-engineering improves frequency and promotes kinetic boosting of serial killing mediated by NK cells. *Blood*.

81. Singh, H., M. J. Figliola, M. J. Dawson, H. Huls, S. Olivares, K. Switzer, T. Mi, S. Maiti, P. Kebriaei, D. A. Lee, R. E. Champlin, and L. J. Cooper. 2011. Reprogramming CD19-specific T cells with IL-21 signaling can improve adoptive immunotherapy of B-lineage malignancies. *Cancer Res* 71: 3516-3527.

82. Singh, H., M. J. Figliola, M. J. Dawson, S. Olivares, L. Zhang, G. Yang, S. Maiti, P. Manuri, V. Senyukov, B. Jena, P. Kebriaei, R. E. Champlin, H. Huls, and L. J. Cooper. 2013. Manufacture of clinical-grade CD19-specific T cells stably

expressing chimeric antigen receptor using Sleeping Beauty system and artificial antigen presenting cells. *PLoS One* 8: e64138.

83. Luisi, J., A. Narayanaswamy, Z. Galbreath, and B. Roysam. 2011. The FARSIGHT trace editor: an open source tool for 3-D inspection and efficient pattern analysis aided editing of automated neuronal reconstructions. *Neuroinformatics* 9: 305-315.

84. Arunachalam Narayanaswamy, Amine Merouane, Antonio Peixoto, Ena Ladi, Paul Herzmark, Ulrich Von Andrian, Ellen Robey, and B. Roysam. 2012. Multi-temporal Globally-Optimal Dense 3-D Cell Segmentation and Tracking from Multi-photon Time-Lapse Movies of Live Tissue Microenvironments. *Lecture notes in computer science* 7570: 147-162.

85. Izsvak, Z., and Z. Ivics. 2004. Sleeping beauty transposition: biology and applications for molecular therapy. *Mol Ther* 9: 147-156.

86. Lex, A., M. Streit, H. J. Schulz, C. Partl, D. Schmalstieg, P. J. Park, and N. Gehlenborg. 2012. StratomeX: Visual Analysis of Large-Scale Heterogeneous Genomics Data for Cancer Subtype Characterization. *Comput Graph Forum* 31: 1175-1184.

87. Foley, M. H., T. Forcier, E. McAndrew, M. Gonzalez, H. Chen, B. Juelg, B. D. Walker, and D. J. Irvine. 2014. High avidity CD8+ T cells efficiently eliminate motile HIV-infected targets and execute a locally focused program of anti-viral function. *PLoS One* 9: e87873.

88. Henkart, P. A., P. J. Millard, C. W. Reynolds, and M. P. Henkart. 1984. Cytolytic activity of purified cytoplasmic granules from cytotoxic rat large granular lymphocyte tumors. *J Exp Med* 160: 75-93.

89. Krammer, P. H., R. Arnold, and I. N. Lavrik. 2007. Life and death in peripheral T cells. *Nat Rev Immunol* 7: 532-542.

90. Romer, P. S., S. Berr, E. Avota, S. Y. Na, M. Battaglia, I. ten Berge, H. Einsele, and T. Hunig. 2011. Preculture of PBMCs at high cell density increases sensitivity of T-cell responses, revealing cytokine release by CD28 superagonist TGN1412. *Blood* 118: 6772-6782.

91. Kochenderfer, J. N., M. E. Dudley, S. A. Feldman, W. H. Wilson, D. E. Spaner, I. Maric, M. Stetler-Stevenson, G. Q. Phan, M. S. Hughes, R. M. Sherry, J. C. Yang, U. S. Kammula, L. Devillier, R. Carpenter, D. A. Nathan, R. A. Morgan, C. Laurencot, and S. A. Rosenberg. 2012. B-cell depletion and remissions of malignancy along with cytokine-associated toxicity in a clinical trial of anti-CD19 chimeric-antigen-receptor-transduced T cells. *Blood* 119: 2709-2720.

92. Kryczek, I., E. Zhao, Y. Liu, Y. Wang, L. Vatan, W. Szeliga, J. Moyer, A. Klimczak, A. Lange, and W. Zou. 2011. Human TH17 cells are long-lived effector memory cells. *Sci Transl Med* 3: 104ra100.

93. Kryczek, I., M. Banerjee, P. Cheng, L. Vatan, W. Szeliga, S. Wei, E. Huang, E. Finlayson, D. Simeone, T. H. Welling, A. Chang, G. Coukos, R. Liu, and W. Zou. 2009. Phenotype, distribution, generation, and functional and clinical relevance of Th17 cells in the human tumor environments. *Blood* 114: 1141-1149.

94. Zhou, J., M. E. Dudley, S. A. Rosenberg, and P. F. Robbins. 2005. Persistence of multiple tumor-specific T-cell clones is associated with complete tumor regression in a melanoma patient receiving adoptive cell transfer therapy. *J Immunother* 28: 53-62.

95. Xu, Y., M. Zhang, C. A. Ramos, A. Durett, E. Liu, O. Dakhova, H. Liu, C. J. Creighton, A. P. Gee, H. E. Heslop, C. M. Rooney, B. Savoldo, and G. Dotti. 2014. Closely related T-memory stem cells correlate with in vivo expansion of CAR.CD19-T cells and are preserved by IL-7 and IL-15. *Blood* 123: 3750-3759.

96. Kiaii, S., A. J. Clear, A. G. Ramsay, D. Davies, A. Sangaralingam, A. Lee, M. Calaminici, D. S. Neuberg, and J. G. Gribben. 2013. Follicular lymphoma cells induce changes in T-cell gene expression and function: potential impact on survival and risk of transformation. *J Clin Oncol* 31: 2654-2661.

97. Gorgun, G., T. A. Holderried, D. Zahrieh, D. Neuberg, and J. G. Gribben. 2005. Chronic lymphocytic leukemia cells induce changes in gene expression of CD4 and CD8 T cells. *J Clin Invest* 115: 1797-1805.

98. Ramsay, A. G., A. J. Clear, G. Kelly, R. Fatah, J. Matthews, F. Macdougall, T. A. Lister, A. M. Lee, M. Calaminici, and J. G. Gribben. 2009. Follicular lymphoma cells induce T-cell immunologic synapse dysfunction that can be repaired with lenalidomide: implications for the tumor microenvironment and immunotherapy. *Blood* 114: 4713-4720.

99. Zinselmeyer, B. H., S. Heydari, C. Sacristan, D. Nayak, M. Cammer, J. Herz, X. Cheng, S. J. Davis, M. L. Dustin, and D. B. McGavern. 2013. PD-1 promotes immune exhaustion by inducing antiviral T cell motility paralysis. *J Exp Med* 210: 757-774.

100. Schneider, H., J. Downey, A. Smith, B. H. Zinselmeyer, C. Rush, J. M. Brewer, B. Wei, N. Hogg, P. Garside, and C. E. Rudd. 2006. Reversal of the TCR stop signal by CTLA-4. *Science* 313: 1972-1975.

101. Pentcheva-Hoang, T., T. R. Simpson, W. Montalvo-Ortiz, and J. P. Allison. 2014. Cytotoxic T Lymphocyte Antigen-4 Blockade Enhances Antitumor Immunity by Stimulating Melanoma-Specific T-cell Motility. *Cancer Immunol Res*.

102. Graw, F., and R. R. Regoes. 2014. Predicting the impact of CD8+ T cell polyfunctionality on HIV disease progression. *J Virol* 88: 10134-10145.

103. Adams, S., R. J. Gray, S. Demaria, L. Goldstein, E. A. Perez, L. N. Shulman, S. Martino, M. Wang, V. E. Jones, T. J. Saphner, A. C. Wolff, W. C. Wood, N. E. Davidson, G. W. Sledge, J. A. Sparano, and S. S. Badve. 2014. Prognostic value of tumor-infiltrating lymphocytes in triple-negative breast cancers from two phase III randomized adjuvant breast cancer trials: ECOG 2197 and ECOG 1199. *J Clin Oncol* 32: 2959-2966.

104. Zaidi, M. R., and G. Merlino. 2011. The two faces of interferon-gamma in cancer. *Clin Cancer Res* 17: 6118-6124.

105. Hu, X., S. D. Chakravarty, and L. B. Ivashkiv. 2008. Regulation of interferon and Toll-like receptor signaling during macrophage activation by opposing feedforward and feedback inhibition mechanisms. *Immunol Rev* 226: 41-56.

106. Qin, Z., J. Schwartzkopff, F. Pradera, T. Kammertoens, B. Seliger, H. Pircher, and T. Blankenstein. 2003. A critical requirement of interferon gamma-mediated angiostasis for tumor rejection by CD8+ T cells. *Cancer Res* 63: 4095-4100.

107. Gerbitz, A., M. Sukumar, F. Helm, A. Wilke, C. Friese, C. Fahrenwaldt, F. M. Lehmann, C. Loddenkemper, T. Kammertoens, J. Mautner, C. A. Schmitt, T. Blankenstein, and G. W. Bornkamm. 2012. Stromal interferon-gamma signaling

and cross-presentation are required to eliminate antigen-loss variants of B cell lymphomas in mice. *PLoS One* 7: e34552.

108. Spranger, S., R. M. Spaapen, Y. Zha, J. Williams, Y. Meng, T. T. Ha, and T. F. Gajewski. 2013. Up-regulation of PD-L1, IDO, and T(regs) in the melanoma tumor microenvironment is driven by CD8(+) T cells. *Sci Transl Med* 5: 200ra116.

109. Mempel, T. R. 2010. Single-cell analysis of cytotoxic T cell function by intravital multiphoton microscopy. *Methods Mol Biol* 616: 181-192.

110. Breart, B., F. Lemaitre, S. Celli, and P. Bousso. 2008. Two-photon imaging of intratumoral CD8+ T cell cytotoxic activity during adoptive T cell therapy in mice. *J Clin Invest* 118: 1390-1397.

111. Chen, Y., E. Ladi, P. Herzmark, E. Robey, and B. Roysam. 2009. Automated 5-D analysis of cell migration and interaction in the thymic cortex from time-lapse sequences of 3-D multi-channel multi-photon images. *J Immunol Methods* 340: 65-80.

112. Liadi, I., H. Singh, G. Romain, N. Rey-Villamizar, A. Merouane, J. R. Adolacion, P. Kebriaei, H. Huls, P. Qiu, B. Roysam, L. J. Cooper, and N. Varadarajan. 2015. Individual Motile CD4+ T Cells Can Participate in Efficient Multikilling through Conjugation to Multiple Tumor Cells. *Cancer Immunol Res* 3: 473-482.

113. Romain, G., V. Senyukov, N. Rey-Villamizar, A. Merouane, W. Kelton, I. Liadi, A. Mahendra, W. Charab, G. Georgiou, B. Roysam, D. A. Lee, and N. Varadarajan. 2014. Antibody Fc engineering improves frequency and promotes kinetic boosting of serial killing mediated by NK cells. *Blood* 124: 3241-3249.

114. Stahlberg, A., V. Rusnakova, and M. Kubista. 2013. The added value of single-cell gene expression profiling. *Brief Funct Genomics* 12: 81-89.

115. Kippner, L. E., J. Kim, G. Gibson, and M. L. Kemp. 2014. Single cell transcriptional analysis reveals novel innate immune cell types. *PeerJ* 2: e452.

116. McDavid, A., G. Finak, P. K. Chattopadyay, M. Dominguez, L. Lamoreaux, S. S. Ma, M. Roederer, and R. Gottardo. 2013. Data exploration, quality control and testing in single-cell qPCR-based gene expression experiments. *Bioinformatics* 29: 461-467.

117. Saeed, A. I., V. Sharov, J. White, J. Li, W. Liang, N. Bhagabati, J. Braisted, M. Klapa, T. Currier, M. Thiagarajan, A. Sturn, M. Snuffin, A. Rezantsev, D. Popov, A. Ryltsov, E. Kostukovich, I. Borisovsky, Z. Liu, A. Vinsavich, V. Trush, and J. Quackenbush. 2003. TM4: a free, open-source system for microarray data management and analysis. *Biotechniques* 34: 374-378.

118. Torres, A. J., A. S. Hill, and J. C. Love. 2014. Nanowell-based immunoassays for measuring single-cell secretion: characterization of transport and surface binding. *Anal Chem* 86: 11562-11569.

119. Han, Q., E. M. Bradshaw, B. Nilsson, D. A. Hafler, and J. C. Love. 2010. Multidimensional analysis of the frequencies and rates of cytokine secretion from single cells by quantitative microengraving. *Lab Chip* 10: 1391-1400.

120. Ekins, R. P. 1998. Ligand assays: from electrophoresis to miniaturized microarrays. *Clin Chem* 44: 2015-2030.

121. Kusnezow, W., Y. V. Syagailo, S. Ruffer, N. Baudenstiel, C. Gauer, J. D. Hoheisel, D. Wild, and I. Goychuk. 2006. Optimal design of microarray immunoassays to

compensate for kinetic limitations: theory and experiment. *Mol Cell Proteomics* 5: 1681-1696.

122. Hastie, T., R. Tibshirani, and J. H. Friedman. 2009. *The elements of statistical learning : data mining, inference, and prediction*. Springer, New York, NY.

123. Xu, Y., P. Qiu, and B. Roysam. 2015. Unsupervised Discovery of Subspace Trends. *IEEE Transactions on Pattern Analysis and Machine Intelligence*: 1-1.

124. Qiu, P., and S. K. Plevritis. 2013. TreeVis: a MATLAB-based tool for tree visualization. *Comput Methods Programs Biomed* 109: 74-76.

125. Zuberi, K., M. Franz, H. Rodriguez, J. Montojo, C. T. Lopes, G. D. Bader, and Q. Morris. 2013. GeneMANIA prediction server 2013 update. *Nucleic Acids Res* 41: W115-122.

126. Faroudi, M., C. Utzny, M. Salio, V. Cerundolo, M. Guiraud, S. Muller, and S. Valitutti. 2003. Lytic versus stimulatory synapse in cytotoxic T lymphocyte/target cell interaction: manifestation of a dual activation threshold. *Proc Natl Acad Sci U S A* 100: 14145-14150.

127. Purbhoo, M. A., D. J. Irvine, J. B. Huppa, and M. M. Davis. 2004. T cell killing does not require the formation of a stable mature immunological synapse. *Nat Immunol* 5: 524-530.

128. Jenkins, M. R., J. A. Rudd-Schmidt, J. A. Lopez, K. M. Ramsbottom, S. I. Mannering, D. M. Andrews, I. Voskoboinik, and J. A. Trapani. 2015. Failed CTL/NK cell killing and cytokine hypersecretion are directly linked through prolonged synapse time. *J Exp Med* 212: 307-317.

129. Kim, S. T., H. Jeong, O. H. Woo, J. H. Seo, A. Kim, E. S. Lee, S. W. Shin, Y. H. Kim, J. S. Kim, and K. H. Park. 2013. Tumor-infiltrating lymphocytes, tumor characteristics, and recurrence in patients with early breast cancer. *Am J Clin Oncol* 36: 224-231.

130. Dudley, M. E., C. A. Gross, R. P. Somerville, Y. Hong, N. P. Schaub, S. F. Rosati, D. E. White, D. Nathan, N. P. Restifo, S. M. Steinberg, J. R. Wunderlich, U. S. Kammula, R. M. Sherry, J. C. Yang, G. Q. Phan, M. S. Hughes, C. M. Laurencot, and S. A. Rosenberg. 2013. Randomized selection design trial evaluating CD8+-enriched versus unselected tumor-infiltrating lymphocytes for adoptive cell therapy for patients with melanoma. *J Clin Oncol* 31: 2152-2159.

131. Whiting, D., G. Hsieh, J. J. Yun, A. Banerji, W. Yao, M. C. Fishbein, J. Belperio, R. M. Strieter, B. Bonavida, and A. Ardehali. 2004. Chemokine monokine induced by IFN-gamma/CXC chemokine ligand 9 stimulates T lymphocyte proliferation and effector cytokine production. *J Immunol* 172: 7417-7424.

132. Kurachi, M., J. Kurachi, F. Suenaga, T. Tsukui, J. Abe, S. Ueha, M. Tomura, K. Sugihara, S. Takamura, K. Kakimi, and K. Matsushima. 2011. Chemokine receptor CXCR3 facilitates CD8(+) T cell differentiation into short-lived effector cells leading to memory degeneration. *J Exp Med* 208: 1605-1620.

133. Hikono, H., J. E. Kohlmeier, S. Takamura, S. T. Wittmer, A. D. Roberts, and D. L. Woodland. 2007. Activation phenotype, rather than central- or effector-memory phenotype, predicts the recall efficacy of memory CD8+ T cells. *J Exp Med* 204: 1625-1636.

134. Bachmann, M. F., M. Barner, and M. Kopf. 1999. CD2 sets quantitative thresholds in T cell activation. *J Exp Med* 190: 1383-1392.

135. Zhu, D. M., M. L. Dustin, C. W. Cairo, H. S. Thatte, and D. E. Golan. 2006. Mechanisms of Cellular Avidity Regulation in CD2-CD58-Mediated T Cell Adhesion. *ACS Chem Biol* 1: 649-658.

136. Ramming, A., K. Thummler, H. Schulze-Koops, and A. Skapenko. 2009. Homotypic T-cell/T-cell interaction induces T-cell activation, proliferation, and differentiation. *Hum Immunol* 70: 873-881.

137. Kunkele, A., A. J. Johnson, L. S. Rolczynski, C. A. Chang, V. Hoglund, K. S. Kelly-Spratt, and M. C. Jensen. 2015. Functional Tuning of CARs Reveals Signaling Threshold above Which CD8+ CTL Antitumor Potency Is Attenuated due to Cell Fas-FasL-Dependent AICD. *Cancer Immunol Res*.